Particle-matrix interactions in ferrogels containing shape-anisotropic, magnetic nanoparticles

Dissertation

to acquire the academic degree
doctor rerum naturalium (Dr. rer. nat.)
of the Faculty of Mathematics and Natural Sciences
at the University of Rostock

submitted by

Annemarie Nack

born on August 19, 1988 in Rostock

2017

urn:nbn:de:gbv:28-diss2017-0127-8

Referees:

Prof. Dr. Joachim Wagner, Universität Rostock
Prof. Dr. Gerhard Grübel, Deutsches Elektronen Synchrotron (DESY), Hamburg

Date of submission: March 24, 2017
Date of scientific colloquium: July 11, 2017

This dissertation was researched and written in the time between October 2013 and July 2017 at the University of Rostock, Institute of Chemistry under the supervision of Prof. Dr. Joachim Wagner.

Per aspera ad astra

Zusammenfassung

In der vorliegenden Arbeit werden feldinduzierte Änderungen der Mesostruktur von Ferrogelen mit formanisotropen magnetischen Hämatitpartikeln und die daraus resultierenden Änderungen der makroskopischen, viskoelastischen Eigenschaften dieser Komposite in externen Magnetfeldern untersucht. Als Modellsysteme dienen in das quervernetzte, thermosensitive Hydrogel poly-N-Isopropylacrylamid eingebettete, spindelförmige Hämatitpartikel verschiedener Aspektverhältnisse. In externen Magnetfeldern richten sich diese Partikel mit ihrer langen Dimension senkrecht zur Feldrichtung aus, was zu einer Deformation der Hydrogelmatrix führt. Partikel-Matrix-Wechselwirkungen werden anhand der über Röntgenkleinwinkelstreuung bestimmten, feldabhängigen Orientierungsverteilungsfunktionen der Hämatitpartikel in Hydrogelen mit unterschiedlichem Polymergehalt und Vernetzungsgrad quantifiziert. Die feldabhängigen, viskoelastischen Eigenschaften der Ferrogele werden mittels rotatorischer und oszillatorischer rheologischer Experimente und mit simultanen rheologischen und Kleinwinkelstreuexperimenten untersucht. Mittels Röntgenphotonenkorrelationsspektroskopie konnte in externen Feldern auf Längenskalen, die der Porengröße der Hydrogele entspricht eine richtungsabhängige Diffusion der Hämatitpartikel beobachtet werden, während Diffusionsprozesse zwischen den Poren unabhängig von der Vorzugsorientierung der Partikel sind.

Abstract

In the present work, field-induced changes of the mesostructure of ferrogels containing anisotropic magnetic particles and the resulting changes of their macroscopic, viscoelastic properties are investigated. As a model system, inter-crosslinked, thermoresponsive poly-N-isopropylacrylamide hydrogels with spindle-shaped hematite particles of different aspect ratio are used. These particles align in external magnetic fields with their long axis perpendicular to the field and provoke an elastic deformation of the hydrogel-network. Particle-matrix interactions are quantitatively analyzed by field-dependent orientational distribution functions of the hematite particles as determined by small angle X-ray scattering in hydrogels with varying volume fraction and crosslinking density. Field-dependent viscoelastic properties are studied by means of rotational and oscillatory rheological experiments and simultaneous rheological and small angle scattering experiments. Employing X-ray photon correlation spectroscopy, in external fields a direction-dependent diffusive motion of hematite particles on length scales corresponding to the size of voids in the hydrogel matrix could be observed while diffusion between adjacent voids is independent of the preferred particle orientation.

Contents

List of abbreviations

DESY Deutsches Elektronen Synchrotron

DLS dynamic light scattering

ESRF European Synchrotron Radiation Facility

GA glutaric aldehyde

LCST lower critical solution temperature

LVE region linear viscoelastic region

NIPAM *N*-isopropylacrylamide

NLVE region nonlinear viscoelastic region

ODF orientational distribution function

PCS photon correlation spectroscopy

PVA poly(vinyl alcohol)

pNIPAM poly(N-isopropylacrylamide)

RheoSAXS rheology small angle X-ray scattering

SAXS small angle X-ray scattering

SDS sodium dodecyl sulfate

SLS Static Light Scattering

TEM transmission electron microscopy

XPCS X-ray photon correlation spectroscopy

1 Introduction

In 1962 Payne et al. showed that both, the elastic responses, and viscosity of rubbers filled with carbon black change with amplitude of oscillation and with the concentration and type of carbon black [1]. Since then, the influence of incorporated nanoparticles on the mechanical properties of elastomers has attracted considerable scientific interest.
Based on these findings, one important focus of today's research is the development and the investigation of materials with extraordinary mechanical properties that can be distinctively changed and controlled by external stimuli such as temperature, pH-level, stress as well as by electric or magnetic fields. Many of these so called smart materials, as for example self-healing materials, shape-memory alloys and polymers, magnetorestrictive materials, pH- and temperature sensitive polymers and gels or ferrofluids are already common in use and knowledge [2–10]. The combination of these properties offers the opportunity to create more complex and specialized composite materials.
Hydrogels generally consist of hydrophilic polymer chains, in some cases forming cross-linked, colloidal particles, in which water is the suspending medium. Therefore, these gels are highly water absorbent and for example used to build contact lenses, breast implants or as super absorbing materials [11–13]. Some hydrogel species can be classified as smart materials since they have the ability to sense changes of, for example, pH, temperature, or the concentration of metabolite and release their load as result of such a change. These properties make them especially interesting for biomedical applications as drug delivering agents [14–16].
Ferrofluids, as another smart material, are colloidal liquids consisting of magnetic colloidal particles suspended in a carrier fluid which can be, for example, an organic solvent or water. They find several applications in medicine as well as in the field of mechanical engineering or in electronic devices as seals and dampers as well as efficient heat transfer medium [9, 17, 18].
By the combination of hydrogels and ferrofluids, ferrogels are obtained. The colloidal magnetic particles incorporated within the polymer network make the ferrogel sensitive to external magnetic fields as a stimulus and therefore its viscous and elastic behavior can be tuned by external magnetic fields [19].
Bio-compatible ferrogels with water as a suspension medium often find an application in the areas of biology and medicine as drug-delivery systems. Triggered by the ferrogels interactions with a magnetic field, pharmaceuticals are released in a controlled manner within the human body [20–22]. Another application can be found for therapeutical hyperthermia, were the suspension medium is heated up due to interactions of the magnetic nanoparticles with the external magnetic field. By means of hyperthermia cancer tissue

can be locally destroyed inducing apoptosis [23]. Regarding the fields of material-sciences and technology, ferrogels are potential candidates for a new generation of sensors and actuators. The ferrogels elastic properties can be controlled by stimuli as external magnetic fields, ion-concentatrion, pH-level or temperature [24, 25]. Artificial muscels as a special kind of actuator are already discussed in literature [26, 27].

Within this work particle-matrix interactions in ferrogels containing shape-anisotropic magnetic nanoparticles are investigated. As a matrix system the temperature-sensitive hydrogel poly(N-isopropylacrylamide) (pNIPAM) is chosen. pNIPAM is an especially interesting polymeric system, since it undergoes a characteristic coil-to-globuli transition around the human body temperature [28] and therefore opens up a wide field of applications including drug delivery, medical diagnostics or tissue engineering. Shape-anisotropic, magnetic hematite nanoparticles serve as filler particles in the materials investigated in this work. If exposed to an external magnetic field, shape anisotropic hematite (Fe_2O_3) nanoparticles align with their long axis perpendicular to the direction of an external field [29]. This behavior makes the spindles a system of special interest as a filler particle for the hydrogel matrix system, since the mesostructure and therewith the mechanical properties of the resulting ferrogels can be influenced by the flux density and the direction of external magnetic fields.
Hematite nanoparticles of different aspect ratios ν as well as intercrosslinked pNIPAM hydrogels consisting of thermoresponsive polymer spheres connected by polymer chains with systematically varying crosslinking ratios χ and polymer volume fractions φ are prepared and characterized topologically, dynamically and rheologically. The influence of the polymer's crosslinking ratio and polymer volume fraction on its viscosity η and viscoelastic behavior is investigated by means of rotational and oscillatory shear experiments. Topological parameters of the hematite nanoparticles are determined by transmission electron microscopy (TEM) and small angle X-ray scattering (SAXS) experiments.
The addition of hematite to the hydrogel matrtix and therewith the formation of a ferrogel causes an increase of the systems' viscosity. This is shown by rotational shear experiments and caused by an additional moment of friction the particles induce in the voids of the hydrogel matrix. By applying an external magnetic field the rotational mobility of the particles is progressively confined with increasing flux density, causing an additional rise of the ferrogels' viscosity.
Oscillatory shear experiments show an elastic particle-matrix interaction in dependence on the flux density. Therefore, the hematite particles can be considered as additional, field dependent crosslinkers in the hydrogel network.
The field-induced rotation of particles embedded in a hydrogel leads to an elastic deformation of the polymer network causing a restoring torque related to the elastic modulus of the hydrogel. Hence, the orientational distribution function (ODF) of hematite spindles as a function of the flux density, which is determined by the analysis of SAXS data, is governed by particle-matrix interactions within these composites. The interactions of the particles with an external magnetic field provoke a field-induced, isotropic-nematic phase

transition which is progressively hindered with increasing elasticity of the matrix.
Further insights into the shear-induced changes of the mesostructure are given by simultaneous, rheological and SAXS (RheoSAXS) experiments. Here, the influence of the networks to the ODF of the hematite spindles is investigated in the vorticity of the velocity field in a laminar shear flow. In oscillatory shear experiments, periodic fluctuations of the scattered intensity between isotropic to anisotropic patterns in phase with the shear deformation, are observed. The anisotropy of the scattered intensity increases, both, with the amplitude of deformation and the aspect ratio of the hematite particles.
To investigate the dynamic behavior of the hematite particles within the pNIPAM hydrogel, X-ray photon correlation spectroscopy (XPCS) experiments with and without an external magnetic field applied to the composites are performed. The Q- and time-dependence of the intensity autocorrelation functions clearly indicates a non-Gaussian diffusion process of the hematite particles. In addition to a compressed exponential decay which is typical for jammed systems, the Q-dependence shows two diffusion regimes separated by a critical length of diffusion paths corresponding of the void size of the hydrogel network. Within the voids, the diffusion is in presence of external fields direction-dependent, while diffusion processes with larger diffusive paths, between adjacent voids, are independent of the direction of the external field. Furthermore, the larger diffusion constant in the small Q-range is a hint for a superdiffusive motion in preformed diffusion channels of the hydrogel network, independent of the individual orientation of the elongated particles.

2 Basic principles of rheology

2.1 Rheological behavior of matter

Rheology, as a subfield of continuum mechanics, investigates the deformation of soft and condensed matter as a response to external stresses. The nature of shear stress and deformation can be demonstrated by two infinite thin, horizontal and parallel plates in a liquid, separated by a very small distance h. If the upper plate is kept stationary while the lower plate is set to motion with a velocity v_0, the liquid layer attached to the lower plate starts to move with the same velocity. With time, as a consequence to this motion, up following liquid layers will start moving due to momentum transfer in between layers. Assuming steady state conditions, the velocity of the uppermost layer, being attached to the stationary plate will be zero, while the bottom layer, in contact with the bottom plate, is still moving with v_0. As a result, across the gap between the two plates, velocity changes linearly with distance y from the stationary plate and the following linear velocity distribution is obtained.

$$v_x = v_0 \frac{y}{h} \tag{2.1}$$

Assuming a horizontal force $-F_x$ opposite to v_0, which must be applied to keep the upper stationary plate at rest and dividing this force by the surface area of the plate, the ratio of the two quantities describes the shear stress τ.

$$\tau = \frac{\mathrm{d}F_x}{\mathrm{d}A} \tag{2.2}$$

The systems shear strain or also called shear deformation γ is defined by the ratio of the lower plates deflection path s and distance between the two plates h as depicted in figure 2.1. Since at steady state, the velocity profile between two plates is linear, every infinitesimal segment in between is represented by the same relation and the expressions can be written in differential form [30, 31].

$$\gamma = \frac{\mathrm{d}s}{\mathrm{d}h} \tag{2.3}$$

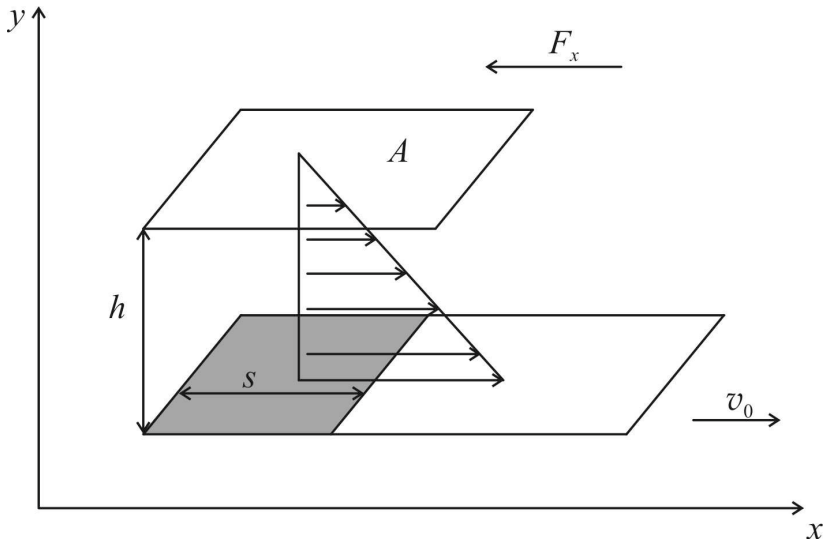

Figure 2.1: Schematic illustration of two-plate model, from which the expressions for deformation γ and shear stress τ can be derivated. The two horizontal plates are assumed to be infinite thin. In this given model the upper plate remains at rest, whereas the lower plate moves horizontally and parallel to the upper plate.

The basic principles of rheology can be derivated by only two fundamental laws of physics. The fist one is Hooke's law, describing the ideal linear elastic behavior of solids within certain limits of elastic deformation.

$$\tau_{yx} = G\frac{\mathrm{d}x}{\mathrm{d}y} \tag{2.4}$$

Here, the shear stress is denoted by τ_{yx} with the dimension of a pressure. The ratio $\mathrm{d}x/\mathrm{d}y$ is the analog to the expression for the deformation γ given in equation (2.2). G is a constant of proportionality between τ_{yx} and γ, known as general modulus of elasticity or shear modulus. Since the deformation is a dimensionless quantity, the shear modulus also has the dimension of a pressure.
The second fundamental law to mention is Newton's law of viscosity, which describes the behavior of atomic or molecular fluids at sufficiently high temperatures and low shear rates $\dot{\gamma}$.

$$\tau_{yx} = \eta\frac{\mathrm{d}v_x}{\mathrm{d}y} \tag{2.5}$$

For Newtonian fluids like water, air or glycerol, the shear stress is proportional to the derivative of the shear deformation $\dot{\gamma} = \mathrm{d}v_x/\mathrm{d}y$, known as shear rate. The constant of proportionality for Newtonian liquids is the viscosity η with the dimension of the product of pressure and time, which is independent of the shear rate.
Regarding equations (2.4) and (2.5), the limiting cases of materials properties can be

stated. For fluids, in the limiting case of $\eta \to 0$ the systems inner friction disappears and the quantum-hydrodynamic effect of supra fluidity occurs. For ^{4}He this behavior is observed beneath the λ-point at T_{SF}=2.17 K [32]. For the limiting case $G \to \infty$ matter behaves as a non-deformable or rigid solid, stating that even very small shear deformations result in infinite shear stresses. Therewith the flow behavior of matter is limited by suprafluidity and the nondeformable solid. In between these limits the behavior step wise shifts from a linear viscous fluid to a linear elastic solid. A summary of these transitions is given in table 2.1.
A systems exposition to a sudden increase and subsequently constant shear deformation results, depending on the material properties, in characteristic shear stress relaxation curves. Figure 2.2 compares τ-relaxation curves for a Hookean solid, a Newtonian fluid and a viscoelastic sample. A Newtonian liquid immediately starts relaxing after the deformation reaches a constant value and therewith the deformation rate, as given in equation (2.5), becomes $\mathrm{d}v_x/\mathrm{d}y = 0$. Viscoelastic systems relaxate over a period of time λ. For a Hookean solid no τ- relaxation is observed since the stress is only proportional to the strain and a sudden change of the deformation leads to an instantaneous response of the stress. In a viscoelastic liquid the shear stress falls off to zero eventually, while for a viscoelastic solid an equlibrium shear stress τ_{E} is reached. Therefore viscoelasticity describes a systems' time dependent answer to an external constraint.

Table 2.1: Summery of rheological behavior of materials within the limiting cases of a nondeformable solid ($G \to \infty$) and an inviscid fluid ($\eta \to 0$) [30].

state	**rheological behavior**	**example**
fluid	inviscid fluid ($\eta \to 0$)	suprafluidic helium
	linear viscous fluid (Newtonian fluid)	water
	nonlinear viscous material	suspensions in Newtonian media
	linear viscoelastic material	polymers under small deformation
	nonlinear viscoelastic material	concentrated polymers solutions or plastic under large deformation
solid	nonlinear elastic material	rubber
	linear elastic solid	linear Hookean spring
	nondeformable solid ($G \to \infty$)	-

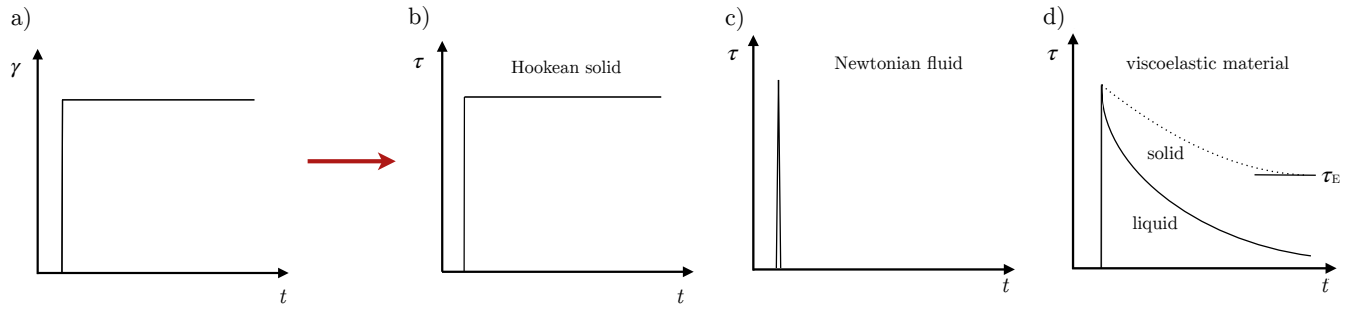

Figure 2.2: Progression of shear stress τ with the evolution of time t for b) a linear elastic, c) linear viscous and d) viscoelastic material while exposed to a) a constant shear deformation.

2.2 Linear and nonlinear viscous fluids

The flow properties of an ideal viscous fluid are formally described by Newton's law of viscosity, as denoted in equation (2.5). The shear stress acting on the liquid is directly proportional to the resulting flow velocity and as a consequence the systems viscosity stays independent from magnitude and duration of the shearing.
Figure 2.3 shows an example for this relation on the basis of a water/glycerol mixture with a volume fraction of 50 % as a typical model system for a Newtonian fluid. On the left hand side the shear stress τ is plotted against the shear rate $\dot{\gamma}$ for different temperatures T. As a result for each temperature, lines through the origin are obtained. The slope of each line corresponds to the systems viscosity at the given temperature. On the right hand side the viscosity η is plotted against the shear rate $\dot{\gamma}$ for different temperatures T. In accordance to the flow curves, the measurements show constant values of viscosity for the investigated shear rates. The slope in viscosity for very small shear rates is caused by an experimental uncertainty during the determination of related, very small torques.

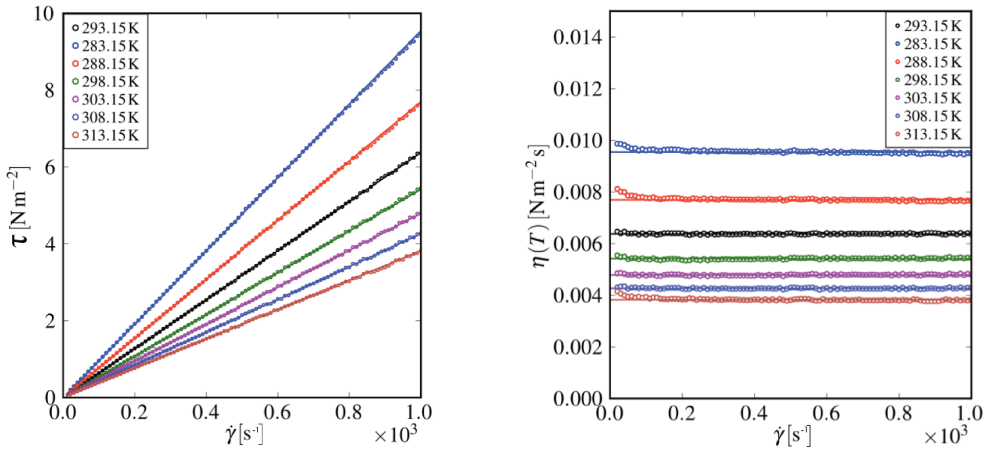

Figure 2.3: Temperature dependent flow- (left) and viscosity curves (right) of a water/glycerol mixture with a volume fraction of 50 % as sample system for a Newtonian liquid.

Water/glycerol mixtures show, like all low molecular mixtures, for moderate, experimentally feasible shear rates an ideal Newtonian behavior. Solutions of oligomers or polymers tend to show already at small concentrations, where the macromolecules' interparticle distances are similar to their size, non-Newtonian behavior. The viscosity of these mixtures is dependent on the applied shear rate. In this case, two main types of behavior can be specified. As a first, shear thinning, also known as pseudoplastic behavior can be named. This behavior is characterized by decreasing viscosity with increasing shear rates. Typical materials that show this behavior are glues, shampoos, polymer mixtures and polymer melts. The second case is shear thickening or dilatant flow behavior, where the viscosity increases with increasing shear rate. Materials that typically exhibit such behavior include highly filled dispersions, such as ceramic suspensions, starch dispersions as well as dental filling masses [31]. In both phenomena, the influence of shear rate on material properties is time independent. If the shear rate becomes a function of time, fluids are referred to as rheopectic or thixotropic. In the first case, the fluid requires a gradually increasing shear stress to maintain a constant shear rate. In case of thixotropy the fluid thins out with time and requires a decrasing stress to maintain a constant shear rate.

2.3 Linear and nonlinear viscoelasticity

A system exposed to a sinusoidal shear deformation will answer to this external constraint with a sinusoidal shear stress. Shear deformation γ and shear stress τ both depend on the same angular frequency ω but may be shifted in phase from one another.

$$\gamma(t) = \gamma_0 \cos(\omega t - \psi) \tag{2.6}$$

$$\tau(t) = \tau_0 \cos(\omega t - \phi) \tag{2.7}$$

$$\text{with } \psi - \phi \geq 0$$

In equations (2.6) and (2.7) τ_0 and γ_0 denote the amplitudes of stress and deformation, t the time and ψ and ϕ the corresponding phase angles. To simplify calculations we assume in the following $\psi = \pi/2$ and $\phi = \pi/2+\delta$, with δ denoting the phase shift angle [31].

$$\gamma(t) = \gamma_0 \sin(\omega t) \tag{2.8}$$

$$\tau(t) = \tau_0 \sin(\omega t + \delta) \tag{2.9}$$

The transfer of these equations to the range of complex numbers delivers the subsequent equations, whereas in the following underlining of physical quantities indicates them as vectors in the complex plane.

$$\underline{\gamma}(t) = \underline{\gamma}_0 \exp(\mathrm{i}\omega t) \tag{2.10}$$

$$\underline{\tau}(t) = \underline{\tau}_0 \exp(\mathrm{i}\omega t) \tag{2.11}$$

The phase information of complex deformation and complex shear stress is included in the complex amplitudes $\underline{\gamma_0}$ and $\underline{\tau_0}$, so that equation (2.10) can be transformed and substituted in equation (2.11).

$$\underline{\tau}(t) = \left(\frac{\underline{\tau}_0 \underline{\gamma}_0^*}{\| \underline{\gamma}_0 \|^2} \right) \underline{\gamma}(t) = \underline{G}\underline{\gamma}(t) \tag{2.12}$$

$\underline{G}$ denotes the complex shear modulus which can be expressed by a real part and an imaginary part or by its modulus multiplied with the phase factor.

$$\underline{G}(\omega) = G'(\omega) + \mathrm{i}G''(\omega) = |\underline{G}(\omega)| \exp[\mathrm{i}\delta(\omega)] \tag{2.13}$$

$G'(\omega)$ and $G''(\omega)$ are known as storage and loss moduli, whereas $\delta(\omega)$ denotes the frequency dependent phase shift angle [33]. $G'(\omega)$ is in phase with the deformation and represents the storage of elastic energy. G'' is in phase with the shear rate, also known as

strain rate and represents the viscous dissipation of energy [34].
The magnitude of the complex modulus is identical with the real amplitude ratio τ_0/γ_0, so for the complex modulus the following can be deviated:

$$\begin{aligned} |\,\underline{G}\,|\exp(\mathrm{i}\delta) &= \frac{\tau_0}{\gamma_0}\exp(\mathrm{i}\delta) \\ &= \frac{\tau_0}{\gamma_0}(\cos\delta + \mathrm{i}\sin\delta) \\ &= \frac{\tau_0}{\gamma_0}\cos\delta + \mathrm{i}\frac{\tau_0}{\gamma_0}\sin\delta \end{aligned} \tag{2.14}$$

Combining this expression with equation (2.13), terms for storage- and loss modulus are obtained.

$$G' = \frac{\tau_0}{\gamma_0}\cos(\delta(\omega)) \qquad\qquad G'' = \frac{\tau_0}{\gamma_0}\sin(\delta(\omega)) \tag{2.15}$$

The consideration of the shear rate $\dot{\gamma}$ and its complex form as the deformations time derivative results in a viscosity dependent expression for the complex, time dependent shear stress.

$$\frac{\mathrm{d}\gamma}{\mathrm{d}t} = \omega\gamma_0\cos(\omega t) \tag{2.16}$$

$$\underline{\dot{\gamma}}(t) = \mathrm{i}\omega\underline{\gamma}_0\exp(\mathrm{i}\omega t) \tag{2.17}$$

$$\begin{aligned} \underline{\tau}(t) &= \frac{\underline{\tau}_0\underline{\gamma_0}^*}{\mathrm{i}\omega\|\gamma_0\|^2}\underline{\dot{\gamma}} \\ &= \frac{\underline{G}}{\mathrm{i}\omega}\underline{\dot{\gamma}} \quad = \underline{\eta}\,\underline{\dot{\gamma}} \end{aligned} \tag{2.18}$$

The complex viscosity $\underline{\eta}$, in analogy to the complex modulus, can be expressed by denoting a real - and an imaginary part or its magnitude multiplied with the phase factor of the quantity. η', as the real part, is known as dynamic viscosity. The imaginary part η'' of $\underline{\eta}$ is called out-of-phase viscosity.

$$\underline{\eta}(\omega) = \eta'(\omega) + \mathrm{i}\eta''(\omega) = |\underline{\eta}(\omega)|\exp\left[-\mathrm{i}\left(\frac{\pi}{2} - \delta(\omega)\right)\right] \tag{2.19}$$

The magnitude of the complex viscosity can also be defined using the amplitude ratios of deformation $\underline{\gamma_0}$ and stress $\underline{\tau_0}$.

$$| \underline{\eta} | = \frac{\tau_0}{\dot{\gamma}_0} = \frac{\tau_0}{\gamma_0 \omega} \tag{2.20}$$

$$\begin{aligned} |\underline{\eta}(\omega)| \exp\left[-\mathrm{i}\left(\frac{\pi}{2} - \delta\right)\right] &= \frac{\tau_0}{\gamma_0 \omega}\left[\cos\left(\frac{\pi}{2} - \delta\right) - \mathrm{i}\sin\left(\frac{\pi}{2} - \delta\right)\right] \\ &= \frac{\tau_0}{\gamma_0 \omega}\left[\sin\delta - \mathrm{i}\cos\delta\right] \\ &= \eta' + \mathrm{i}\eta'' \end{aligned} \tag{2.21}$$

Therewith the following expressions for dynamic viscosity and out-of-phase viscosity are obtained [35].

$$\eta' = \frac{\tau_0}{\gamma_0 \omega}\sin(\delta) = \frac{G''}{\omega} \qquad\qquad \eta'' = \frac{\tau_0}{\gamma_0 \omega}\cos(\delta) = \frac{G'}{\omega} \tag{2.22}$$

Taking all the terms into consideration, a summarized equation for the modulus of the complex viscosity is found.

$$| \underline{\eta} | = (\eta^* \eta)^{1/2} = (\eta'^2 + \eta''^2)^{1/2} \tag{2.23}$$

$$= \left[\left(\frac{G''}{\omega}\right)^2 + \left(\frac{G'}{\omega}\right)^2\right]^{1/2} \tag{2.24}$$

The relative importance of viscous and elastic contributions for a material at given frequency is quantified by the ratio of loss and storage modulus and is broadly known as the loss factor $\tan(\delta)$. This ratio is high ($\tan\delta \gg 1$) for materials that are considered liquid-like, but low ($\tan\delta \ll 1$) for solid-like materials.

$$\frac{G''}{G'} = \frac{(\tau_0/\gamma_0)\sin\delta}{(\tau_0/\gamma_0)\cos\delta} = \tan\delta \tag{2.25}$$

If the strain amplitude γ_0 is small enough (typically $\gamma_0 \ll 1$) that the equilibrium structure of an unsheared fluid is not significantly disturbed by the deformation, then the stress measured during oscillatory shear experiments is controlled by the rates of spontaneous rearrangement, or relaxation present in the fluid. The shear stress $\tau(t)$ produced by small-amplitude deformation is proportional to the amplitude of the applied strain γ_0 and is itself sinusoidally varying in time. In general, the sinusoidally varying stress can be represented as

$$\tau(t) = \gamma_0[G'(\omega)\sin(\omega t) + G''(\omega)\cos(\omega t)]. \tag{2.26}$$

The regime of small-amplitude straining, in which $G'(\omega)$ and $G''(\omega)$ are independent of the amplitude of deformation γ_0 (see equation (2.26)) is called the linear viscoelastic regime [34]. Linear properties are of great interest, because in most cases they relate to the molecular structure of the materials. Structural changes of condensed matter induced by deformations lead to nonlinear viscoelastic behavior since the elastic properties themselves become dependent on the deformation γ and its temporal derivative $\dot{\gamma}$.

3 Basic principles of scattering

Scattering experiments are of great significance in the field of condensed matter physics. The spatial structure of matter, as for example the position of atoms or of microscopic magnetic moments, characterizing the magnetic structure, can be precisely determined. Additionally, from inelastic scattering experiments we obtain information on a systems time structure, meaning its state of movement, also referred to as dynamic structure. This is characterized by for example lattice vibration excitations, magnetic excitations like spin waves or dynamic processes like diffusion.

3.1 Scattering of electromagnetic waves

In 1864 Maxwell predicted via the now commonly known Maxwell equations, that an accelerated electric charge will emit energy in the form of electromagnetic waves traveling with a velocity c in vacuum. A derivation of the electromagnetic wave equations originating from Maxwell's equations [36] show, that electromagnetic waves consist of oscillating electric and magnetic fields.

$$\begin{aligned} \frac{1}{c^2}\frac{\partial^2 \mathbf{E}}{\partial t^2} - \nabla^2 \mathbf{E} = 0 \\ \frac{1}{c^2}\frac{\partial^2 \mathbf{B}}{\partial t^2} - \nabla^2 \mathbf{B} = 0 \end{aligned} \tag{3.1}$$

The electric and magnetic field vectors $\mathbf{E}$ and $\mathbf{B}$ are perpendicular to each other as well as to the direction of the waves propagation. Electrons moving back and forth in a straight wire produce, within the validity of the far-field approximation, a plane polarized wave, as shown in figure 3.1, where all electric field vectors $\mathbf{E}$ lie in the same plane. A wave emitted by independently moving charges like ionized atoms, however, is unpolarized, because of random orientations of the electric field vector $\mathbf{E}$ at various points in space. For an unpolarized wave, $\mathbf{E}$ and $\mathbf{B}$ are still perpendicular to the direction of propagation [37].

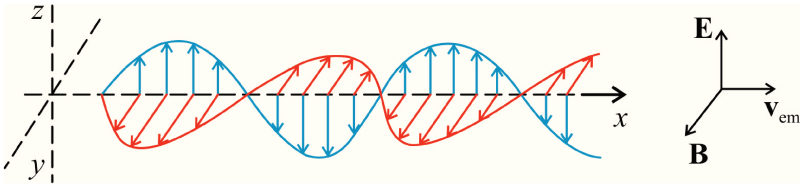

Figure 3.1: Schematic representation of a plane-polarized electromagnetic wave, with **E** and **B** as electric and magnetic field vectors and c as velocity of the electromagnetic wave.

The wavelength λ of a wave specifies the spatial distance between successive maxima or minima of the wave front of the electric or magnetic field. One period describes a segment of any two successive points, having the same phase. The frequency ν of the wave is the number of periods passing a given point per unit in time. The electromagnetic wave spectrum can be sketched as shown in figure 3.2.

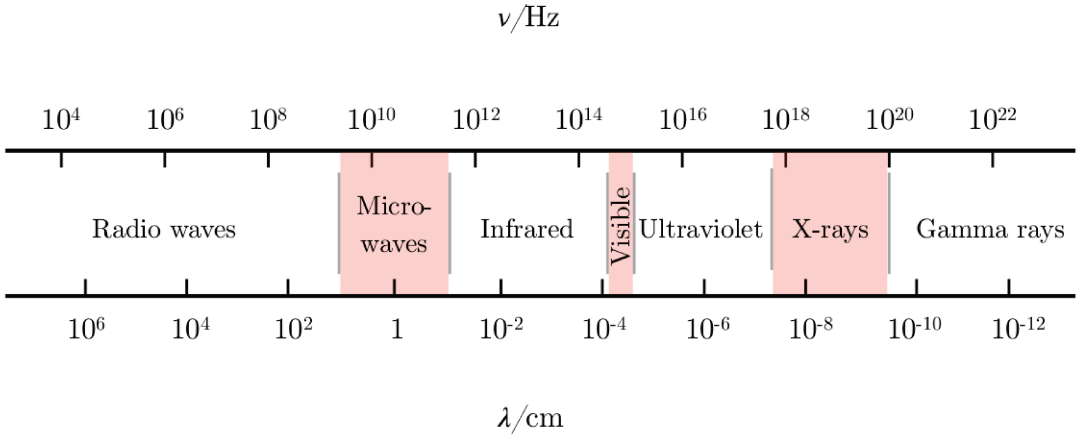

Figure 3.2: Extract of the electromagnetic spectrum.

Elastic and inelastic scattering

Electromagnetic waves are one of the best known and most commonly encountered forms of radiation that undergo scattering. The scattering process of a wave and the scattering object itself, as for example a scattering process of a photon as the quasi particle of an electromagnetic wave and an atom can either be elastic or inelastic.
If a scattering process is elastic, the energy of the photon $E = h\,\nu = (hc)/\lambda$ with Planck's constant h and c the vacuum speed of light, remains unchanged. If energy is either transferred to the sample by excitation of electrons, vibrations or rotations or from the sample to a photon by transition from an excited state to one of lower energy, the scattering process is considered inelastic.

Scattering of electromagnetic waves by matter

Compton scattering *Compton scattering* is the inelastic scattering of photons by charged particles such as electrons. As a result, a decrease of the photons energy an therewith an increase of its wavelength is observed. Part of the energy is absorbed by the recoiling electron in the moment of collision. The oppsosite process, where a charged particle transfers energy to a photon is know as *reversed Compton scattering*. The low energy limit of Compton scattering is called *Thomson scattering* as an elastic scattering process, where the photon energy is much smaller than the mass energy $h\nu \ll mc^2$ of the colliding particle.

Rayleigh scattering *Rayleigh scattering* is an elastic scattering process of electromagnetic waves by particles much smaller in size than the incident wavelength λ as for example when visible light is scattered by small molecules. The particle or molecule is illuminated by a parallel beam of linearly polarized radiation and becomes polarized in the electromagnetic field due to the displacement of electrons with respect to the nuclei and also due to the partial orientation of any permanent dipoles that might be present. The basic premise is, because the particle is small compared to the wavelength, that the instantaneous field which it experiences due to the electromagnetic waves is uniform over its extent [38]. Due to electron displacement, a dipole moment is induced and acts like a Hertzian dipole, emitting light of the same wavelength as the incident electromagnetic wave.
The Rayleigh scattering cross section σ_s is given by

$$\sigma_\mathrm{s} = \frac{2\pi^5}{3}\frac{d^6}{\lambda^4}\left(\frac{n^2-1}{n^2+2}\right)^2. \tag{3.2}$$

Here, d is the small sphere diameter, λ as the incident wavelength and n the refractive index [39]. As a result of the λ^{-4} wavelength dependence of σ_s, shorter wavelengths are scattered more strongly than longer wavelengths.
It is also possible for the incident photons to interact with the molecules in such a way that energy is either gained or lost, so that the scattered photons are shifted in frequency. Such inelastic scattering is called *Raman scattering*. For polarizable molecules, the incident photon energy can excite vibrational modes of the molecules, yielding scattered photons which are diminished in energy by the amount of the vibrational transition energies. A spectral analysis of the scattered light under these circumstances will reveal spectral satellite lines below the Rayleigh scattering peak at the incident frequency. Such lines are called *Stokes lines*. If there is significant excitation of vibrational excited states of the scattering molecules, then it is also possible to observe scattering at frequencies above the incident frequency as the vibrational energy is added to the incident photon energy. These lines, generally weaker, are called *anti-Stokes lines* [37].

Mie scattering For Compton or Rayleigh scattering, it is assumed that each segment of the scattering object interacts with the same electric field generated by the incident electromagnetic wave. This approximation fails for objects with the size of the order of the incident wave and if the particles' interior is optically much different from the surrounding medium [40, 41]. The Mie theory describes the exact solution of the Maxwell equations for the scattering of a plain electromagnetic wave by an object of any size and shape more generally. *Mie scattering* describes scattering events where the size of the scattering particles is comparable to the wavelength of the incident electromagnetic waves, rather than much smaller or much larger.

Scattering vector

A characteristic quantity to characterize scattering processes is the scattering vector $\mathbf{Q}$. If an electromagnetic wave with the wave vector $\mathbf{k}_\mathrm{i}$ impinges on an object, it is scattered by the object at an angle θ. As a result the difference between the wave vector of the incident wave $\mathbf{k}_\mathrm{i}$ and the wave vector of the scattered wave $\mathbf{k}_\mathrm{f}$ is obtained (see Fig. 3.3) and defined as

$$\mathbf{Q} = \mathbf{k}_\mathrm{i} - \mathbf{k}_\mathrm{f} \tag{3.3}$$

with

$$|\mathbf{k}_\mathrm{i}| = \frac{2\pi}{\lambda_\mathrm{i}} \qquad |\mathbf{k}_\mathrm{f}| = \frac{2\pi}{\lambda_\mathrm{f}}. \tag{3.4}$$

A scattering process can also be understood as a momentum transfer. In quantum mechanics the momentum is defined as $|\mathbf{p}| = h/\lambda$. Therewith we can write

$$\Delta\mathbf{p} = \frac{h}{2\pi}\left(\mathbf{k}_\mathrm{i} - \mathbf{k}_\mathrm{f}\right) = \hbar \cdot \mathbf{Q} \tag{3.5}$$

It is usually the case, that in static and dynamic light scattering elastic scattering processes are evaluated. Therewith the change in frequency and following by that the energy difference between incident and scattered photon becomes zero. Hence λ_i and λ_f as well as $|\mathbf{k}_\mathrm{i}|$ and $|\mathbf{k}_\mathrm{f}|$ are identical and the modulus of $\mathbf{Q}$ can be written as

$$|\mathbf{Q}|^2 = |\mathbf{k}_\mathrm{i}|^2 \cos 0 - 2|\mathbf{k}_\mathrm{i}||\mathbf{k}_\mathrm{f}| \cos\theta + |\mathbf{k}_\mathrm{f}|^2 \cos 0 = 2|\mathbf{k}_\mathrm{i}|^2(1 - \cos\theta). \tag{3.6}$$

Replacing the expression for $|\mathbf{k}_\mathrm{i}|$ from equation (3.4) and applying the addition theorem of cosines $\cos\theta = 1 - 2\sin^2(\theta/2)$ the expression for the scattering vector

$$|\mathbf{Q}| = \frac{4\pi}{\lambda} \sin\left(\frac{\theta}{2}\right) \tag{3.7}$$

is obtained [40]. The modulus of the scattering vector is related to the corresponding length d in real space by $d = 2\pi/Q$. Big objects scatter at small angles and small objects at wide angles. The scattering pattern therewith is the display of the reciprocal or the Fourier space [42].

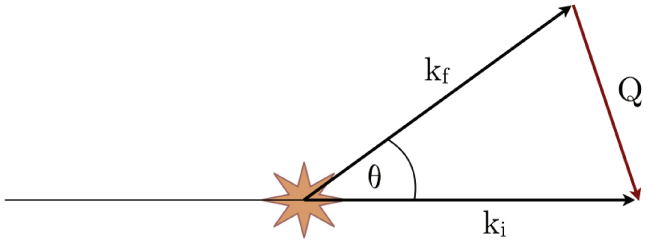

Figure 3.3: Schematic figure for the definition of the scattering vector **Q**.

3.2 Static scattering theory

The average scattered intensity is given by the magnitude of the time averaged Poynting vector $\mathbf{S} = \mathbf{E} \times \mathbf{H}$ of the scattered field corresponding to an energy normalized to unit area and unit time [43]. The scattering cross section σ is the ratio of scattered and incident energy per unit area of the illuminated sample. The differential scattering cross section $\mathrm{d}\sigma/\mathrm{d}\Omega$ is defined as the scattering cross section σ per unit solid angle Ω and characterizes the interaction between incident radiation and the sample. In scattering events as described in section 3.1 the incident photon intensity I_0 is scattered by a sample and the scattered photons are acquired by each detector element subtending a solid angle $\Delta\Omega$ with the efficiency ϵ. The resulting detected intensity for negligible absorption hence is given by [42]

$$I_\mathrm{s} = I_0 \epsilon \Delta\Omega \frac{\mathrm{d}\sigma}{\mathrm{d}\Omega}. \tag{3.8}$$

For a dilute system containing N uniform particles per unit volume and neglecting inter-particle interactions, $I(Q)$ depends on the shape, on the size of the particles and the scattering length density difference between particles and their environment.

$$I(\mathbf{Q}) = N|F(\mathbf{Q})|^2 \tag{3.9}$$

For X-rays as a probe, $F(Q)$ is the Fourier transform of the coherent sum of the scattering amplitudes of the electrons as individual scattering centers within the particle [44]. For SAXS experiments the electron density can be approximated as a continuous function,

therewith the scattering amplitude of the particle, with respect to the volume of the particle V can be expressed as

$$F(\mathbf{Q}) = \int_V \rho(\mathbf{r}) \mathrm{e}^{-\mathrm{i}\mathbf{Q}\mathbf{r}} \mathrm{d}\, V. \tag{3.10}$$

If the scattering particles are embedded in a matrix, the relative scattering length density also known as contrast length density $\Delta\rho$ becomes relevant for the scattering function. Furthermore inserting the orientational average for the phase factor, for isotropic particles, we obtain the following one-dimensional form

$$F(Q) = 4\pi \int_0^\infty \Delta\rho(r) \frac{\sin(Qr)}{Qr} r^2 \mathrm{d}r. \tag{3.11}$$

Also for randomly aligned anisotropic scatterers, the intensity will be isotropic. For a homogeneous spherical particle of radius R and Volume V_s, the following expression with $P_\mathrm{sp}(QR)$ as *form factor of a sphere* is obtained [42]:

$$\begin{aligned} |F(Q)|^2 &= {V_\mathrm{s}}^2 \Delta\rho^2 \left(\frac{3\left[\sin(QR) - QR\cos(QR)\right]}{(QR)^3} \right)^2 \\ &= {V_\mathrm{s}}^2 \Delta\rho^2 P_\mathrm{sp}(QR). \end{aligned} \tag{3.12}$$

Real colloidal particle systems underlie a natural distribution of particle sizes, quantified by the polydispersity of a system. If $p(R)$ is the normalized probability density, $p(R)\,\mathrm{d}R$ is the probability to find particles with radii between R and $R + \mathrm{d}R$. Hence, the intensity of a polydisperse system underlying a size distribution $p(R)$ can be expressed as

$$I(Q) = N\Delta\rho^2 \int_0^\infty p(R) V^2(R) P(Q,R) \mathrm{d}R. \tag{3.13}$$

The factor $V^2(R)$ takes the proportionality of the scattering power to the squared particle volume in the Rayleigh-Gans-Debye limit into account.
From the kinetics of polymerization reactions the Schulz-Flory distribution function

$$p(R) = \frac{1}{\Gamma(\mathrm{Z}+1)} \left(\frac{Z+1}{R_0} \right)^{Z+1} R^Z \exp\left(-\frac{Z+1}{R_0} R \right), \tag{3.14}$$

describing the distribution of molar masses of formed polymers, is known [45]. Z is

related to the width, whereas R_0 is the first moment of the distribution. The Schulz-Flory distribution is also convenient to describe particle size distributions, since analytical expressions for integrals like (3.13) exist.

For anisotropic particles, the scattered intensity depends on the particles' orientation relative to the direction of the scattering vector $\mathbf{Q}$. For axially symmetric particles, with additional inversion symmetry, the scattered intensity depends on $(\hat{\mathbf{Q}}.\,\hat{\mathbf{u}})^2$, where $\hat{\mathbf{Q}}$ is a unit vector in the direction of the scattering vector and $\hat{\mathbf{u}}$ is the particle director, a unit vector in the direction of the paricles' principal symmetry axis.
If $f(\vartheta_\mathrm{P}, \varphi_\mathrm{P})$ is the ODF of an ensemble of anisotropic particles related to the laboratory coordinate system defined, e.g., by the direction of an external magnetic field, $f(\vartheta_\mathrm{P}, \varphi_\mathrm{P})\mathrm{d}\cos\vartheta_\mathrm{P}\mathrm{d}\varphi_\mathrm{P}$ is the normalized probability to find a particle director in the solid angle $\mathrm{d}\cos\vartheta_\mathrm{P}\mathrm{d}\varphi_\mathrm{P}$. Hence, the scattered intensity in the laboratory coordinate system can be written as

$$I(Q, \vartheta_\mathrm{Q}) = \int_0^\pi \int_0^{2\pi} f(\vartheta_\mathrm{P}, \varphi_\mathrm{P}) P(Q, \gamma(\vartheta_\mathrm{P}, \varphi_\mathrm{P}; \vartheta_\mathrm{Q}\varphi_\mathrm{Q}))\mathrm{d}\cos\vartheta_\mathrm{P}\mathrm{d}\varphi_\mathrm{P}. \tag{3.15}$$

Here,

$$\gamma(\vartheta_\mathrm{P}, \varphi_\mathrm{P}; \vartheta_\mathrm{Q}\varphi_\mathrm{Q}) = \cos\vartheta_\mathrm{P}\cos\vartheta_\mathrm{Q} + \sin\vartheta_\mathrm{P}\sin\vartheta_\mathrm{Q}\cos(\varphi_\mathrm{P} - \varphi_\mathrm{Q}) \tag{3.16}$$

is the cosine of the angle between the particle director and the direction of the scattering vector. Due to the axial symmetry of the particles φ_Q can be chosen arbitrarily and the scattered intensity only depends on the modulus Q of the scattering vector and the angle ϑ_Q enclosed between the scattering vector and the external field, as can be seen in figure 3.4.
The ODF can be obtained with a Boltzmann-Ansatz taking into account the energy $V_\mathrm{P}(\vartheta_\mathrm{P}, \varphi_\mathrm{P})$ of a particle with the orientation $\hat{\mathbf{u}} = (\cos\varphi_\mathrm{P}\sin\vartheta_\mathrm{P}, \sin\varphi_\mathrm{P}\sin\vartheta_\mathrm{P}, \cos\vartheta_\mathrm{P})$ relative to the direction of $\hat{\mathbf{B}}$ of an external field.
We have

$$f(\vartheta_\mathrm{P}, \varphi_\mathrm{P}) = \frac{1}{Z}\exp\left(-\frac{V_\mathrm{P}(\vartheta_\mathrm{P}, \varphi_\mathrm{P})}{k_\mathrm{B}T}\right) \tag{3.17}$$

where Z is the partition function

$$Z = \int_{-1}^{1} \int_0^{2\pi} \exp\left(-\frac{V_\mathrm{P}(\vartheta_\mathrm{P}, \varphi_\mathrm{P})}{k_\mathrm{B}T}\right)\mathrm{d}\cos\vartheta_\mathrm{P}\mathrm{d}\varphi_\mathrm{P}. \tag{3.18}$$

The energy of a magnetic particle in an external field consists of the Zeeman energy of a permanent magnetic dipole with a possible offset ϑ_offs relative to the particles' rotation

axis and the energy of a field-induced magnetic dipole in the external magnetic field. Since the induced dipole

$$\mu_{\mathrm{ind}} = \frac{V}{\mu_0} \begin{bmatrix} \chi_\perp & 0 & 0 \\ 0 & \chi_\perp & 0 \\ 0 & 0 & \chi_\parallel \end{bmatrix}. \mathbf{B} \tag{3.19}$$

$$= \frac{V}{\mu_0} \left\{ \left(\frac{2\chi_\perp + \chi_\parallel}{3} \right) \cdot I + \frac{1}{3} \begin{bmatrix} -\Delta\chi & 0 & 0 \\ 0 & -\Delta\chi & 0 \\ 0 & 0 & 2\Delta\chi \end{bmatrix} \right\} \tag{3.20}$$

is determined by the susceptibility tensor $\underline{\underline{\chi}}$ the second addendend of which is a traceless, symmetric, second-order tensor, the orientation dependent excess energy is proportional to

$$\Delta\chi = \chi_\parallel - \chi_\perp. \tag{3.21}$$

Hence, the total energy V_{P} of a particle in an external field B is given by

$$V_{\mathrm{P}} = -\mu B \cos\vartheta_\mu - \frac{\Delta\chi V}{2\mu_0} B^2 \cos^2\vartheta_{\mathrm{P}}. \tag{3.22}$$

Here ϑ_μ is the angle between the magnetic moment and field direction given by

$$\cos\vartheta_\mu = \cos\vartheta_{\mathrm{P}} \cos\vartheta_{\mathrm{offs}} + \sin\vartheta_{\mathrm{P}} \sin\vartheta_{\mathrm{offs}} (\cos\varphi_{\mathrm{P}}) \tag{3.23}$$

The orientational order of anisotropic particles in an external magnetic field can be quantified by the nematic order parameter S_2 [46, 47]

$$S_2 = \frac{1}{2} \langle 3\cos^2\vartheta_{\mathrm{P}} - 1 \rangle, \tag{3.24}$$

the canonical average of the ODF weighted by the 2nd Legendre polynomial. For a system completely aligned parallel to the external field, $S_2 = 1$ results, while a complete alignment perpendicular to the external field leads to $S_2 = -1/2$. For a statistically aligned system, finally $S_2 = 0$ is obtained.

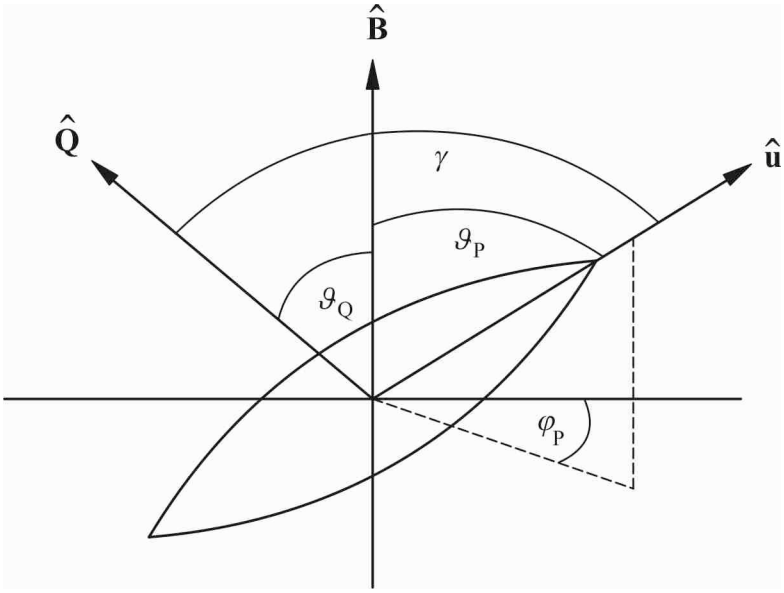

Figure 3.4: A spindle-shaped particle in a spherical coordinate system defined by the direction of the external magnetic field $\mathbf{B}$. The scattered intensity of a particle with $\hat{\mathbf{u}} = (\cos\varphi_\mathrm{P}\sin\vartheta_\mathrm{P}, \sin\varphi_\mathrm{P}\sin\vartheta_\mathrm{P}, \cos\vartheta_\mathrm{P})$ depends on the angle $\sphericalangle(\hat{\mathbf{u}}, \hat{\mathbf{Q}})$, while its energy in the external field depends on $\sphericalangle(\hat{\mathbf{u}}, \hat{\mathbf{B}})$.

3.3 Dynamic scattering theory

The time average $\langle A\rangle$ of an observable A is defined as

$$\langle A\rangle = \lim_{T\to\infty} \frac{1}{T} \int_0^T A(t)\mathrm{d}t \tag{3.25}$$

with T as the time interval over which the quantity A is observed and $A(t)$ as the value of A at time t. Experimentally, A is measured for discrete time intervals. Thus a discrete representation for calculating a average of A is to divide the time scale in j discrete intervals.

$$\langle A\rangle = \lim_{N\to\infty} \frac{1}{N} \sum_{j=1}^{N} A(t_j) \tag{3.26}$$

If the interval is shrunk to infinitesimal times, the integral (3.25) results. Time averages like the square value of A are of great importance in many soft matter applications [42] as for example in the mean squared displacement of particles.

$$\langle A^2 \rangle = \lim_{T\to\infty} \frac{1}{T} \int_0^T A^2 \mathrm{d}t \tag{3.27}$$

In an analog way, the mean square of $\langle A^2 \rangle$ of an observable can be calculated according to (3.27) or as a discrete approximation as

$$\langle A^2 \rangle = \lim_{N\to\infty} \frac{1}{N} \sum A^2(t_j). \tag{3.28}$$

Mean squares like the mean squared displacement $\langle (r_i(t+\tau) - r_i(\tau))^2 \rangle_{i,\tau}$ are of particular importance for diffusion.
Temporal correlations can be quantified by means of the autocorrelation function of an observable A

$$\langle A(t_0)A(t_0+\tau) \rangle = \lim_{T\to\infty} \frac{1}{T} \int_{t_0}^{t_0+T} A(t)A(t+\tau)\mathrm{d}t. \tag{3.29}$$

With the scattering intensity I as an observable, the intensity autocorrelation function

$$\begin{aligned} g_2(Q,t) &= \frac{\langle I(Q,0)\, I(Q,t) \rangle}{\langle I(Q) \rangle^2} \\ &= 1 + \beta(Q) \left(\frac{\langle E(Q,0)\, E^*(Q,t) \rangle}{\langle I(Q) \rangle} \right)^2 \end{aligned} \tag{3.30}$$

is the measured parameter in homodyne, dynamic light scattering (DLS) or photon correlation spectroscopy (PCS) either employing visible light or coherent X-rays as a probe. $\beta(Q)$ denotes the Q-dependent speckle contrast. This second expression is also known as corrected *Siegert relation*. $g_2(Q,t)$ is subsequently expressed in terms of the field autocorrelation function $g_1(Q,t)$ with

$$g_2(Q,t) = 1 + \beta(Q)[g_1(Q,t)]^2 \tag{3.31}$$

where

$$g_1(Q,t) = \frac{S(Q,t)}{S(Q,0)} \tag{3.32}$$

and

$$S(Q,t) = \left[\frac{1}{N\langle b^2(Q) \rangle} \right] \sum_{n=1}^{N} \sum_{m=1}^{N} \langle b_n(Q) b_m(Q) \cdot \exp\left(-iQ\left[r_n(0) - r_m(t)\right]\right) \rangle. \tag{3.33}$$

The number of scatterers is denoted with N, the square of the scattering amplitude averaged over the particle size distribution with $\langle b^2(Q)\rangle$. The averaged argument is interpreted as an ensemble average with $[r_n(0) - r_m(t)]$ as the expression for the particles' displacement. At $t = 0$, $S(Q, 0)$ is defined as the static structure factor.
For an ensemble of monodisperse particles undergoing Brownian motion [48], in absence of particle-particle interactions the particle positions are uncorrelated and therefore results $S(Q, 0) = 1$. The mean square value of the particles' displacement, considering free Brownian particle motion is

$$\langle [r_n(0) - r_m(t)]^2 \rangle = 6D_0 t \tag{3.34}$$

with D_0 as the free particle or Stokes-Einstein diffusion coefficient of a particle, since with $S(Q, 0) = 1$ only self-correlations with $n = m$ survive in the average [49–51]. D_0 can be expressed by

$$D_0 = \frac{k_\mathrm{B} T}{6\pi\eta R} \tag{3.35}$$

with the hydrodynamic particle radius R and η as the dynamic viscosity of the surrounding medium. Therewith the expression for the field autocorrelation function reduces to

$$g_1(Q, t) = \exp\left(-D_0 Q^2 t\right). \tag{3.36}$$

From the negative slope of the logarithm of the field autocorrelation function with respect to time t, the diffusion coefficient can be determined from the slope $-Q^2\, D_0$. The relaxation rate can be written as

$$\Gamma(Q) = Q^2\, D_\mathrm{E}, \tag{3.37}$$

also known as *Landau-Placzek relation* [52, 53].
In presence of particle-particle interactions, this equation is no longer valid and a wavevector - as well as time-dependent diffusion coefficient $D(Q, t)$ results [42]. As a short time limit for collective diffusion, the effective diffusion coefficient can be determined via the initial slope of the intermediate scattering function.

$$D_\mathrm{eff}(Q) = \lim_{t \to \text{"0"}} D(Q, t) \tag{3.38}$$

$t \to$ "0" denotes times, that are short compared to the structural relaxation time but longer than the impulse relaxation time of the system. The effective diffusion coefficient

follows the extended *de-Gennes narrowing* [54]

$$D_{\text{eff}}(Q) = \frac{D_0}{S(Q)} H(Q) \tag{3.39}$$

with D_0 as short-time self diffusion coefficient and $H(Q)$ as the hydrodynamic function. $H(Q)$ respects retarded interactions caused by flow patterns in the suspending medium by the particles' motion. These interactions are not instantaneous but time-delayed, because the speed of propagation of such shear waves is finite. The structure factor $S(Q)$ is only governed by instantaneous interactions.

4 Ferrogels

One challenge of modern research is the development and investigation of new multifunctional smart materials that possess intelligence at a material level. Ferrogels are of great importance and interest in this broad field of research since they can be influenced by external magnetic fields. Ferrogels are composite systems consisting of a polymeric gel matrix as poly(vinyl alcohol) (PVA), gelatine or poly(N-isopropylacrylamide) (pNIPAM) and colloidal magnetic particles as magnetite (Fe_2O_3), maghemite (γ-Fe_2O_3) or cobalt ferrite ($CoFe_2O_4$) which are at high volume fractions also known as ferrofluids [55–58].
In 1969 NASA physicist Steve Papell invented the first ferrofluid for the application as a low density and low viscosity magnetic propellant usable under zero-gravity conditions [59]. Since then the field of application for ferrofluids has been significantly widened. Technical applications as inertia dampers, sealing fluids or loudspeakers have been established [60, 61]. In the field of medicine, magnetic nanoparticles in ferrofluids find their application as carriers in drug targeting systems [62], as contrast agents in NMR tomography [63] as well as absorbents for high-frequency electromagnetic fields and the resulting application in hyperthermia as cancer treatment [39, 64, 65].
Polymer gels are unique intelligent materials in the sense that no other class of materials can be made to respond to various stimuli. Volume phase transition in response to external stimuli like temperature, pH level, solvent type, light intensity or the addition of specific ions has been observed for several systems [66]. In order to accelerate the response of those gels to external stimuli, the use of magnetic, field-sensitive gels has been developed. One of the first to describe the influence of nonuniform magnetic fields on a ferrogel were Zrínyi et al. They investigated the possibility of elongation and contraction of chemically crosslinked-PVA-magnetite composites by means of a magnetic field gradient produced by an electromagnet. A field dependent magneto-elastic behavior of the ferrogel was found [55, 67] and foundation for the development of a new class of smart materials was layed.

4.1 Colloidal filler particles

In up to now described ferrogels based on soft polymer gels, mostly spherical magnetic nanoparticles are used as microrheological probes to investigate the viscoelastic properties. *Cobalt ferrite* nanoparticles have been incorporated into thermoresponsive pNIPAM microgel particles and their response to an external magnetic field has been investigated with a scanning force microscope [56]. Also, the influence of *maghemite* and *platinum*

(Pt) nanoparticles on the swelling behavior and the volume phase transition of pNIPAM microgel spheres have been studied and an application of maghemite covered microgels as a carrier for controlled and target drug release has been stated[58, 68]. Superparamagnetic *magnetite* (Fe_3O_4) in a crosslinked gelatine matrix was found to reduce the gels poresize in presence of an external magnetic field and an application as a drug release system was derivated [69]. In this work, spindle-shaped magnetic *hematite* (Fe_2O_3) nanoparticles with tunable aspect ratio are used as microrheological probes to investigate elastic and viscous properties of such ferrogels. Generally, if shape anisotropic, magnetic particles are embedded in viscoelastic matrices, their mesoscopic structure and dynamics and the related macroscopic properties depend on the particles' orientation as an additional degree of freedom. Distortions of the matrix either induced by interaction of the particles with an external field or mechanical stresses exerted on the composites influence, both, the spatial and orientational distribution of the particles. In addition, shape anisotropic nanoparticles as mesogens are constituents of lyotropic, mineral liquid crystals (LCs). Both, discotic and calamitic mineral LC phases, consisting, e.g., of *boehmite* (γ-*AlO(OH)*) plates or *goethite* (α-*FeO(OH)*) as well as *silica rods* are described [70–72]. Already in 1949, Onsager predicted the formation of a nematic phase by mineral colloids with the decrease in excluded volume compensating a loss of orientational entropy [73]. By means of Small Angle X-ray Scattering and computer simulations it was already accomplished to state a packing fraction and magnetic field dependent phase diagram of silica coated hematite particles, in which a nemaitc phase is distinctly identified [74].

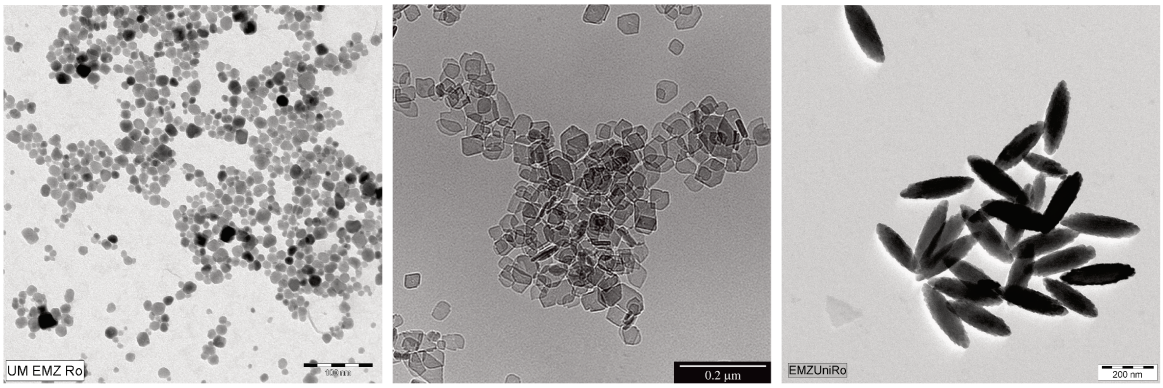

Figure 4.1: TEM micrographs of spheric cobalt ferrite (lhs), plate-like boehmite [75] (middle) and spindle-shaped hematite particles (rhs) as examples for the variety of colloidal filler particles embedded in ferrogels.

4.2 Polymer gel matrix

4.2.1 Hydrogels

A variety of chemical substances qualifies as a building block for polymer gels. Generally, gels can be divided in *lyogels*, when the extension medium is a liquid and *xerogels* with a gaseous extension medium. In the special case of water as extension medium, the term *hydrogel* is appropriate, in the case of air as gaseous medium the gel is called *aerogel*.
Typical and extensively investigated polymeric hydrogels are for example poly(vinylalcohol), poly(acrylamide) or gelatine based gels.

poly(vinylalcohol) based gels Due to the high number of hydroxy groups in the chemical polymer structure it is obvious that this polymer has strong hydrophilic properties. By crosslinking individual polymer strands for example with glutaric aldehyde as a bifunctional aldehyde, a three dimensional network is formed as the system transfers to a gel-state. PVA is prepared by the hydrolysis of poly(vinylacetate). poly(vinylacetate) is the polymerization product of the via Wacker-reaction achieved vinyl acetate. As a hydrogel, PVA is for example found in contact lenses with low oxygen permeability or as thickening agent in shampoos or glues.

Gelatin based gels Gelatin is a mixture from peptides and proteins produced by the hydrolysis of collagen, which is extracted from the skin, bones or connective tissue of animals. Gelatin, once formed, dissolves easily in water and forms a gel, when cooled down. In these hydrogel networks, the volume percentage of gelatine normally does not exceed a value of 5%. Since it is of natural origin, an application especially in medicine is likely, although for the same reason its usage is restricted due to limited preservability.

poly(acrylamide) based gels Radical polymerization and chemical crosslinking of acrylamides, results in the formation of polyacrylamides, which find many uses as water soluble thickeners. These are for example hydrogels, used as supporting material for gel electrophoresis (SDS-PAGE) or flocking agent in the field of water purification.
If copolymerized with monomers carrying Brønsted-Lowry acid or base functionalities as acrylic acid (see figure 4.2), in water charged polymer networks, polyelectrolyte hydrogels, are formed and the swelling ability of the gel is increased. The technical application are superabsorbent polymers (SAPs) for example in diapers or as packing material for humidity-sensitive materials.
Acrylamide hydrogels which are functionalized by an alkyl substituent at the amide nitrogen, as it is given for polymerized N-isopropylacrylamide (NIPAM), mostly show a lower critical solution temperature (LCST), below which the polymer is mixable with water for every given composition. Above the LCST, which for poly(N-isopropylacrylamide) (pNIPAM) is with $T \approx 32°\mathrm{C}$ close to the human body temperature, the system shows

phase separation into a two phase system. Additionally these systems' viscositys show a strong dependence on the temperature as an external parameter and are therefore ascribed to the class of thermoresponsive smart materials.

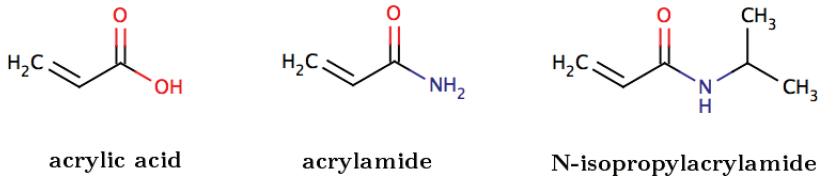

Figure 4.2: Overview of acrylamide-based monomers, forming polymer gels.

4.2.2 poly(N-isopropylacrylamide)

pNIPAM is a well-known thermosensitive polymer and undergoes a *coil-to-globuli transition* around the human body temperature [28]. This transition is important in a number of practical applications including drug delivery, medical diagnostics, tissue engineering and electrophoresis.
To explain this temperature dependent coil-to-globuli transition, the amphiphilic character of pNIPAM molecules with a polar amide and non-polar backbone and isopropyl groups is of great importance [76, 77]. Similar to the one of globular proteins, the coil-to-globule collapse of pNIPAM involves the formation of intramolecular H-bonds among the peptide (−CONH−) groups and the breakage of intermolecular H-bonds among the peptide groups of the chain and water molecules. From the enthalpic point of view, the process is endothermic, indicating that polar peptide groups prefer water rather than the nonpolar interior of the globule, supposedly because there is a higher chance of engaging in H-bonds in the aqueous medium.
From the entropic point of view, the process decreases the conformational degrees of freedom of the polymer chain, but it increases the configurational freedom of water molecules previously H-bonded to the CONH-groups of the chain. In addition, the coil to globule collapse reduces strongly the space occupied by the polymer chain in solution, decreasing the excluded volume and raising further the configurational entropy of water molecules.
Experimental measurements demonstrate that the sum of entropy contributions is positive enough to overwhelm the contrasting enthalpy contribution and to initiate the formation of the compact globule. At low temperature, the enthalpic terms are dominant stabilizing the expanded coil state of pNIPAM with peptide-groups H-bonded to water molecules. At high temperature, the entropic terms related to the configurational entropy of water molecules become dominant stabilizing the compact globule state of pNIPAM.[77].

The temperature dependency of the hydrodynamic radius of spheric pNIPAM polymer particles can easily be determined by means of DLS. In figure 4.3 this has been done for different pNIPAM species, varying for example in the degree of crosslinking or the amount

of surfactant added to the reaction mixture. It is visible, that within the given temperature range of 15 °C to 40 °C the hydrodynamic radius R_h for every species decreases with increasing temperature differently, but is equal after passing the supposed LCST of ≈ 32 °C. Here, as described above, the polymer network of each particle species collapses and the globuli-structure is dominant, independent from the preperational parameters.

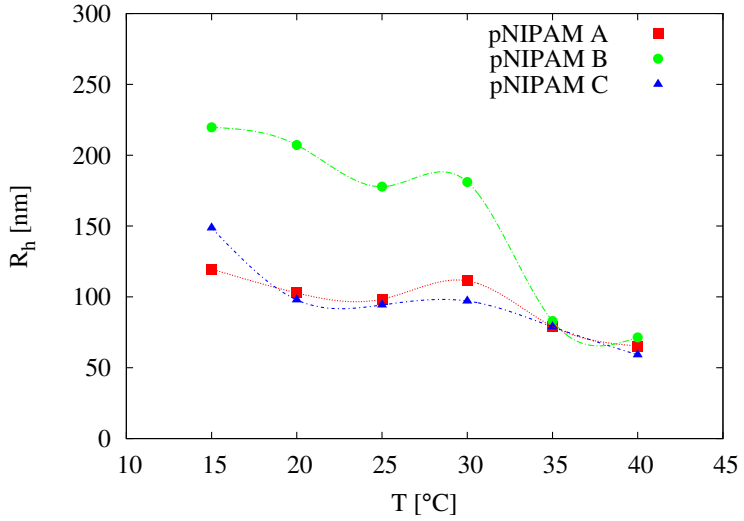

Figure 4.3: Determination of the hydrodynamic radius R_h for spherical pNIPAM particle species via dynamic light scattering (DLS), indicating pNIPAMs lower critical solution temperature at ≈ 32 °C

5 Experimental

5.1 Preparation of sample systems

5.1.1 Preparation of hematite particles

Spindle shaped hematite nanoparticles are prepared via a one-step batch reaction as published by Ozaki et al. [78] in 1984, following chemical equation (5.1).
An aqueous solution of sodium dihydrogen phosphate (NaH_2PO_4) is heated to the boiling point and reflux. Subsequently iron(III)-chloride ($FeCl_3$) is added and the reaction mixture is kept under reflux for 48 hours. During the process of reaction the turbidity of the suspension is increasing. The suspensions' final color is a deep orange-red.

$$2FeCl_3 + 3H_2O \xrightarrow[\Delta,\,48h]{NaH_2PO_4} Fe_2O_3 + 6HCl \tag{5.1}$$

In the reprocessing step the suspension is centrifuged at 4000 rpm step wise and the remaining centrifugate washed at least twice with deionized water in order to eliminate small particle populations. After resuspending the washed centrifugate a suspension with a narrow size distribution of hematite spindles is achieved without carrying out further reprocessing steps like dialysis.
The obtained particle suspensions are stable in aqueous, polar environment, since the ironoxide surface carries negative charges for neutral to weakly acidic pH levels. Within this work, the concentration of NaH_2PO_4 is varied systematically and therefore a wide range of particle aspect ratios $\nu = L/\sigma_{eq}$ is obtained.
In table 5.1 an overview of the preparations for hematite spindles investigated in this work is given. The parameter ϵ denotes the ratio $\epsilon = m(NaH_2PO_4)/m(FeCl_3)$ and is related to the aspect ratio of the resulting hematite spindles. High values of ϵ will most likely result in spindles with high aspect ratio ν and vice verca.

Table 5.1: Overview of the amounts of $FeCl_3$, NaH_2PO_4 and H_2O used for the preparation of hematite spindles presented in this work. ϵ denotes the ratio $\epsilon = m(NaH_2PO_4)/m(FeCl_3)$.

	$m(FeCl_3)$	$m(NaH_2PO_4)$	$V(H_2O)$	ϵ
HEM 1	3.234 g	0.075 g	1 L	0.023
HEM 2	3.259 g	0.035 g	1 L	0.011
HEM 3	3.255 g	0.061 g	1 L	0.019
HEM 4	3.243 g	0.032 g	1 L	0.010

5.1.2 Preparation of pNIPAM hydrogels and ferrogels

pNIPAM hydrogels are prepared by a single step, free radical emulsion polymerization of NIPAM, inspired by a publication by Hu et al. [79], describing the preparation of hydrogels forming colloidal crystals. Simple free radical polymerization of NIPAM results in a colloidal suspension of uncrosslinked pNIPAM spheres. To obtain a crosslinked hydrogel, glutaric aldehyde (GA) - a bifunctional $\alpha - \omega$-dialdehyde as a crosslinking agent is added to the mixture. The proposed mechanism to this reaction is shown in the reaction scheme in figure 5.1.
As a first step, water is heated in a nitrogen atmosphere whilst stirring continuously up until the oil bath temperature reaches 80 °C. After one hour equilibration time an aqueous solution of 50 wt% GA, NIPAM and sodium dodecyl sulfate (SDS) as a surfactant are added to the reaction mixture. Finally, after all additives have been properly dissolved in water, an aqueous solution of potassium persulfate ($K_2S_2O_8$) as radical initiator is added and the reaction mixture is kept at an oil bath temperature of 80 °C in a nitrogen atmosphere for four hours.
Only few minutes after adding the radical initiator, the reaction mixture shows increasing turbidity which results after four hours of reaction time in a white, opaque liquid, which becomes a transparent, colorless gel after cooling down to room temperature. Subsequently the gel is dialyzed against water for at least one week in order remove remaining salts and surfactants from the network and is afterwards reduced to a volume of 100 ml via vacuum distillation.
Within this work, the polymer volume fraction φ and the crosslinking ratio χ are varied systematically during preparation of the hydrogel samples as can be seen in table 5.2. The crosslinking ratio and polymer volume fraction are determined by

$$\chi = \frac{n_{\mathrm{GA}}}{n_{\mathrm{GA}} + n_{\mathrm{NIPAM}}} \tag{5.2}$$

$$\varphi = \frac{V_{\mathrm{monomer}}}{V_{\mathrm{total}}} \tag{5.3}$$

with n denoting the amount of substance of each reactant and V denoting the given volume. The hematite-hydrogel composites are prepared by mixing hydrogels and aqueous hematite suspensions and stirring until homogeneity is achieved verified by optical transmission.

Table 5.2: Overview of preparations of different pNIPAM hydrogel matrix systems presented in this work. χ denotes the crosslinking ratio as denoted in equation (5.3).

	m(NIPAM)	m(GA)	m(SDS)	$m(K_2S_2O_8)$	$V(H_2O)$	χ	φ
pN 1	6.99 g	0.22 g	0.02 g	0.1 g	250 ml	0.034	0.065
pN 2	6,99 g	0.20 g	0.02 g	0.1 g	250 ml	0.028	0.065
pN 3	5.49 g	0.20 g	0.02 g	0.1 g	250 ml	0.040	0.052
pN 4	5.00 g	0.49 g	0.02 g	0.1 g	250 ml	0.102	0.047
pN 5	5.00 g	0.26 g	0.02 g	0.1 g	250 ml	0.056	0.047
pSys 1	5.00 g	53.0 µl	0.02 g	0.1 g	250 ml	0.025	0.047
pSys 2	4.99 g	109.8 µl	0.02 g	0.1 g	250 ml	0.050	0.047
pSys 3	4.99 g	231.8 µl	0.02 g	0.1 g	250 ml	0.100	0.047
pSys 4	10.00 g	106.9 µl	0.04 g	0.1 g	250 ml	0.025	0.09
pSys 5	10.03 g	219.6 µl	0.04 g	0.1 g	250 ml	0.050	0.09
pSys 6	10.01 g	464.0 µl	0.04 g	0.1 g	250 ml	0.100	0.09
pSys 7	14.99 g	160.5 µl	0.06 g	0.1 g	250 ml	0.025	0.13
pSys 8	14.99 g	329.4 µl	0.06 g	0.1 g	250 ml	0.05	0.13
pSys 9	15.00 g	695.0 µl	0.06 g	0.1 g	250 ml	0.100	0.13

5.2 Rheological investigations

Rheological investigations are executed by using a MCR 302 rheometer by Anton-Paar. For rotational and oscillatory shear experiments without external magnetic fields a cone-plate geometry with the diameter $d_{\mathrm{cp}} = 25$ mm and for the same experiments with an external magnetic field within the sample environment, a plate-plate geometry with a diameter $d_{\mathrm{pp}} = 16\,\mathrm{mm}$ is used.
The application of an external magnetic field is possible by using the Anton Paar MRD (magneto-rheological measuring cell) setup. Therewith, in the investigated volume, flux densities up to 1.0 T can be applied during the experiments. The temperature is monitored via a PT 100 sensor in the center of the bottom plate in immediate vicinity of the sample. During the magnetic field-dependent experiments a temperature stability better than $\Delta T = 0.15\,\mathrm{K}$ is achieved. The direction of the external magnetic field is parallel to

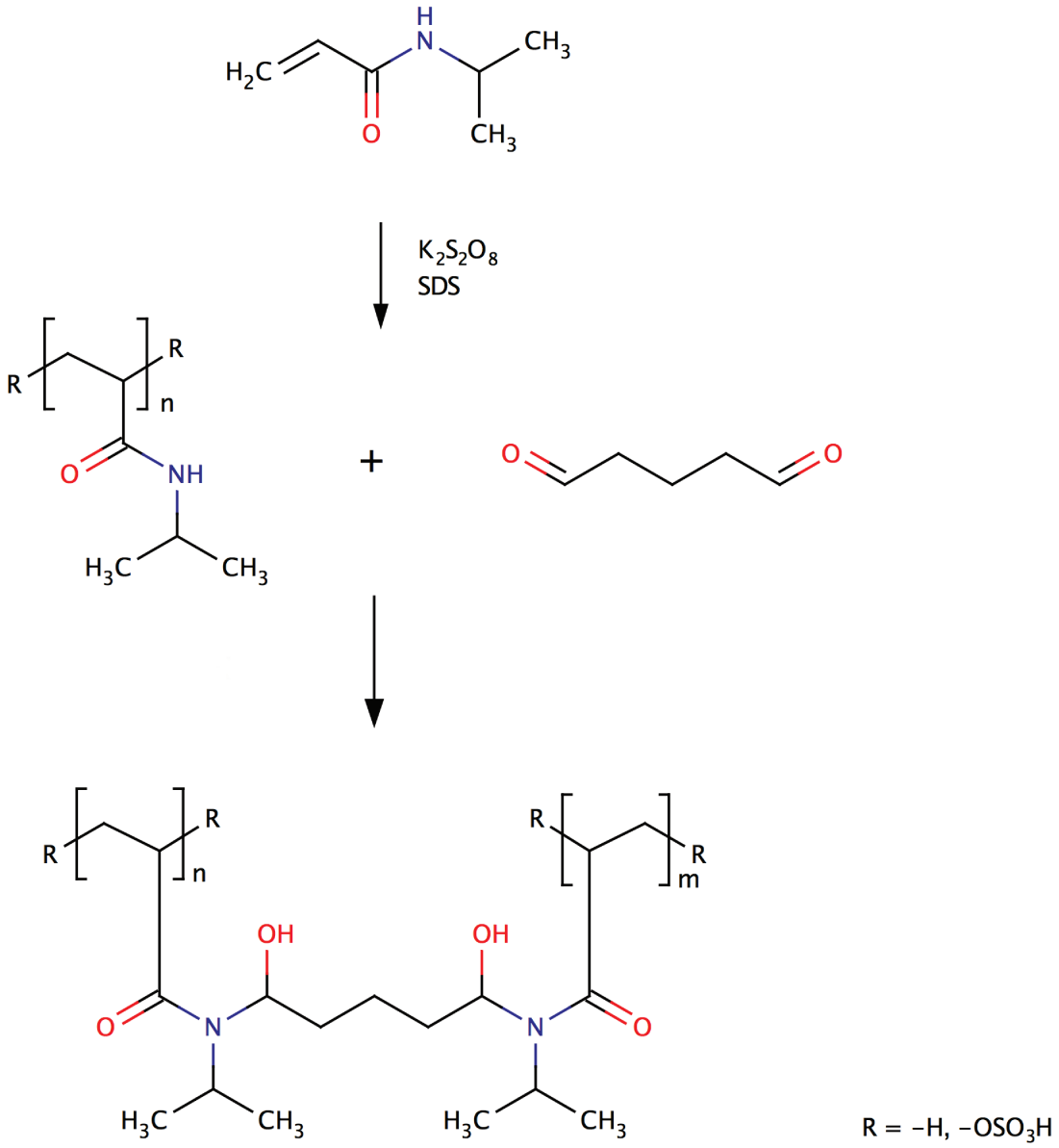

Figure 5.1: Reaction scheme of radical polymerization of NIPAM and GA to prepare globally crosslinked pNIPAM hydrogel network. Subscripts n and m indicate a statistical distribution of NIPAM segments between crosslinking points within the network, not the existence of a defined order as found in block copolymer.

the direction of the applied shear gradient.
Within this work, for rotational shear experiments, the shear rate $\dot{\gamma}$ as well as the temperature T of the sample are systematically varied and the systems' response in changes of the viscosity η are investigated. For oscillatory shear experiments next to the variation of the temperature also the shear frequency f and the deformation γ are variables. The systems response to these stresses is observed by evaluating the storage and loss moduli G' and G'' as well as the loss factor $\tan\delta$ and the complex viscosity corresponding to equations (2.25) and (2.24).

5.3 X-ray scattering experiments

Time-resolved ultra small-angle X-ray scattering beamline ID02

Magnetic field dependent SAXS experiments are performed at the high brilliance beamline ID02 at the European Synchrotron Radiation Facility (ESRF) in Grenoble, France. This beamline is optimized for experiments using a fixed wavelength around $\lambda = 1$ Å (12.4 keV), although due to three undulators and a Si(111) channel-cut monochromator wavelengths between 0.73 Å and 1.6 Å with high photon flux of maximum 10^{14} photons/sec/100 mA are accessible. The default beam size is 0.2×0.4 mm^2 (vertical and horizontal, respectively) [80].
An external magnetic field can be applied with a sample environment using rare-earth permanent magnets with variable pole distances. With this setup, flux densities of $0.1\ \text{mT} \leqslant B \leqslant 1.5\ \text{T}$ perpendicular and $0.1\ \text{mT} \leqslant B \leqslant 1.2\ \text{T}$ parallel to the primary beam can be applied. Figure 5.2 shows an image of the sample environment.
For experiments performed at the ID02 beamline within this work the incident energy is chosen 12 keV ($\lambda = 0.997$ Å) with a sample-detector distance of $s = 20$ m. Magnetic fields parallel and perpendicular to the beam direction are applied and the magnetic flux density B is systematically varied to investigate particle-matrix interactions. The illuminated sample volume is with $1 \times 0.2 \times 0.4$ mm^3 significantly smaller than the pole size (100×50 mm^2) of the magnets. Hence, the magnetic field in the illuminated sample volume, which is placed in the center between the poles, is gradient free and highly homogeneous.

Soft interfaces and coherent scattering beamline ID10

XPCS experiments to investigate the dynamic behavior of the hematite-pNIPAM composites in dependence on an external magnetic field are performed at the multi-purpose, high-brillance undulator beamline ID10 at ESRF in Genoble, France. Due to a Water cooled Si(111) pseudo channel cut crystal monochromator a wide wavelength range from $\lambda = 0.5166$ Å (7 keV) to 1.77 Å (24 keV) of maximum 10^{10} photons/second/100 mA is accessible. At ID10 XPCS experiments with high coherent flux are limited to energies of 7-10 keV and 21-24 keV. The minimum accessible Q is, depending on the energy, around

$Q \approx 10^{-2}\,\mathrm{nm}^{-1}$ [81].
The sample environment already described in the previous section is used to perform XPCS experiments in external magnetic fields.
For XPCS experiments at ID10 described in this work, the incident energy is chosen to 7 keV ($\lambda = 1.7712\,\text{Å}$) to avoid resonant scattering of iron at an energy below its K-absorption edge at 7.111 keV [82]. The sample detector distance is set to $s = 5.24\,\mathrm{m}$.

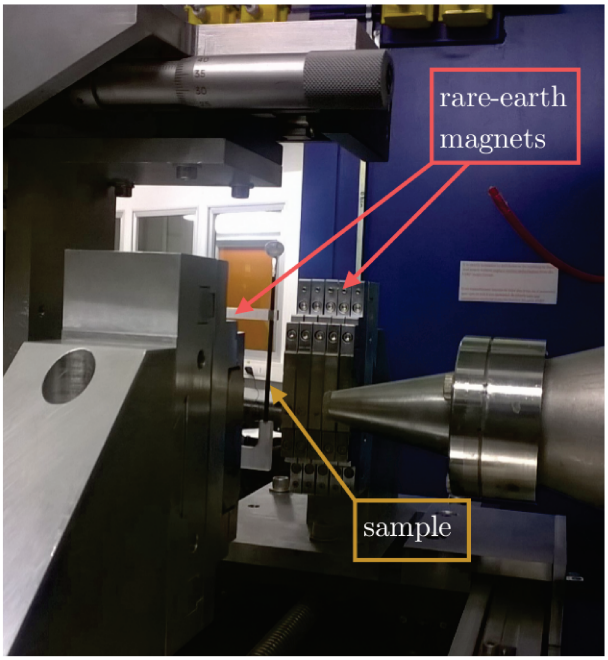

Figure 5.2: ID02 sample environment at ESRF. The pole distance of assemblies of rare-earth magnets can be varied by a step motor in order to tune to different magnetic flux densities during experiments.

RheoSAXS setup at coherence application beamline P10

In order to obtain simultaneously information about the viscoelastic properties and the structural organisation of hematite-hydrogel composites, rheology small angle X-ray scattering (RheoSAXS) experiments are performed at the coherence beamline P10 at the Deutsches Elektronen Synchrotron (DESY) in Hamburg, Germany. The incident energy during RheoSAXS experiments described in this work is determined to 8 keV (λ =1.5489 Å) by the 90° - Bragg reflection at a Si(333) crystal used to deflect the horizontal X-ray beam to the vertical beam needed for the rheometer setup. For these experiments, the maximum possible detector distance of $s = 3\,\mathrm{m}$ is chosen.
The rheometer is a modified Thermo Fisher MARS II constructed with an inverted geometry in order to meet the special requirements for the use with vertically deflected synchrotron radiation. In this configuration, the drive system of the rheometer is located below the sample cell, allowing the scattered beam to travel unhampered and vertically

through a flight tube to the detector mounted above. As a detection system a Pilatus 300K, 2D hybrid pixel-array detector with a pixel size of $172 \times 172\ \mu m^2$ is used.
The intrinsically horizontal X-ray beam has to be deflected to vertical, to pass through the plate-plate geometry of the modified rheometer. This is facilitated by a Si(333) single crystal placed in the beam path before the rheometer. By deflecting the beam, it is possible to probe the perpendicular configuration of any fluid material between the two measuring plates, since it travels through the sample along the velocity gradient. Figure 5.3 shows an image of the sample environment, also depicting the beampath. Scattering of the incoming X-ray beam will produce characteristic X-ray patterns which depend on the orientations of periodic structures in the sample, formed due to external stresses in the rheometer. During experiments, viscosity ranges from $\eta = 0.1 - 1000\,\mathrm{Pas}$ and shear rates between $\dot{\gamma} = 0.002 - 2700\,\mathrm{s}^{-1}$ are accessible [83].

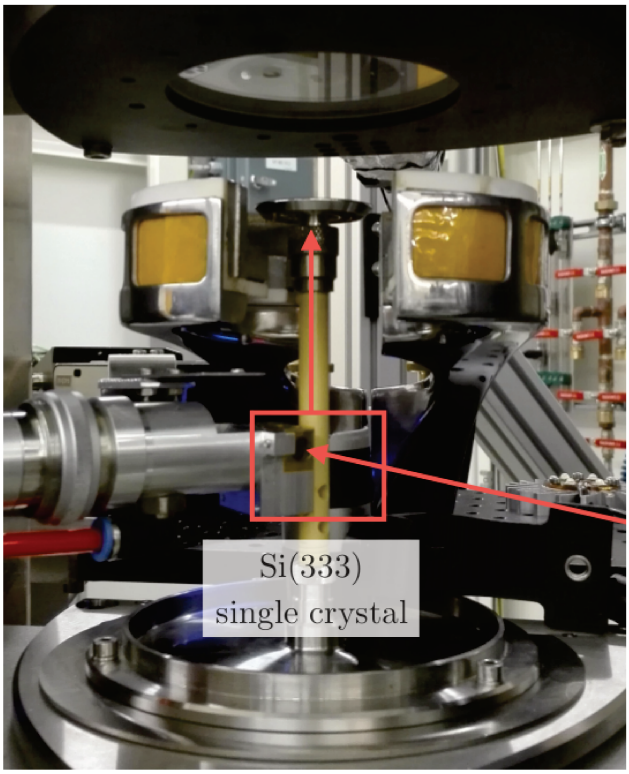

Figure 5.3: P10 RheoSAXS setup with red arrows displaying the X-ray beam path.

5.4 Transmission electron spectroscopy

TEM micrographs are taken using an EM 902 electron microscope by Carl Zeiss (Oberkochen, Germany). The microscopes maximum acceleration voltage is 80 keV. The sample is prepared by covering a carbon coated copper grid with the hematite-hydrogel composite. Therefore the composite is diluted with deionized water, the copper grid is dipped into

the suspension and afterwards the grid is dried until the solvent evaporates completely.

5.5 Dynamic light scattering

DLS experiments are performed with the goniometer CGS 32 by ALV (Langen, Germany). As a light source a frequency doubled Nd-YAG Laser with a wavelength of $\lambda = 532$ nm is implemented in the setup. The sample is captured by a quartz cuvette, placed in a sample compartment filled with toluene. Since silica glass and toluene have similar refractive indices, surface scattering of the cuvette is suppressed almost completely. A heat exchanger placed in the toluene containing vat connected to a circulation thermostat allows temperature-dependent light scattering experiments.The temperature of the toluene bath is monitored by a PT 100 sensor. With this setup, a temperature stability better ± 0.1 K is achieved. The scattered light is guided by an optical single-mode fiber and a fiber-optical beam splitter to two avalanche photo diodes the signal of which is pseudo-crosscorrelated to suppress electronical background noise. Typically, dynamic light scattering experiments are performed at a scattering angle of 90° for 600 s.

6 Basic characterization of nanoparticles and hydrogel matrix

6.1 Hematite spindles

Within this work, four species of hematite spindles are used as filler particles for the pNIPAM-hematite composites (see section 5.1). To properly evaluate and understand particle-matrix interactions it is necessary to entirely characterize the topology of the hematite spindles. This can be easily done by transmission electron microscopy (TEM). In figure 6.1 TEM micrographs of all hematite species are shown.

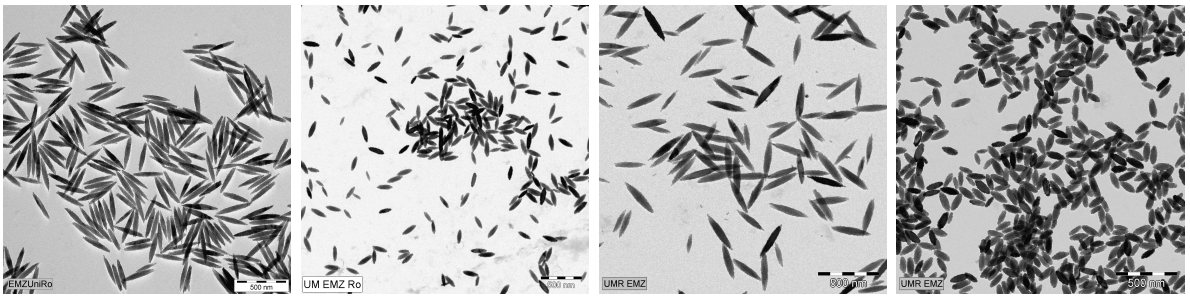

Figure 6.1: TEM micrographs of hematite samples (HEM 1, HEM 2, HEM 3, HEM 4, from left to right) investigated in this work.

Topological parameters as the distribution of length L and equatorial diameter σ_{eq} as well as the aspect ratio ν are determined from TEM micrographs and converted to normalized histograms as shown in figure 6.2. The data presented in these histograms are additionally fitted by a Schulz-Flory distribution [45],

$$f(r, r_0, Z) = \frac{1}{\Gamma(Z+1)} \left(\frac{Z+1}{r_0}\right)^{Z+1} r^Z \exp\left(-\frac{Z+1}{r_0} r\right) \tag{6.1}$$

the optimum parameters of which are compiled in table 6.1. $r_0 = \langle r \rangle$ is the mean size, while the parameter Z is related to the width of the distribution expressed as the square root of normalized variance, defining the polydispersity

$$p = \left(\frac{\langle r_0^2 \rangle - \langle r_0 \rangle^2}{\langle r_0 \rangle^2} \right)^{1/2} = \sqrt{\frac{1}{Z+1}} \,. \tag{6.2}$$

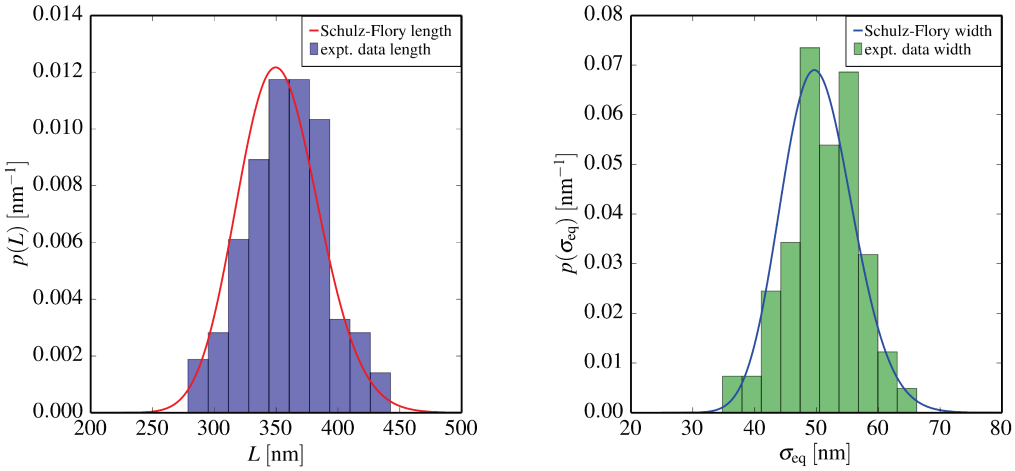

Figure 6.2: Size distribution of lengths L (blue, lhs) and equatorial diameters σ_{eq} (green, rhs) of sample HEM 1 determined by means of TEM, as well as fits to a Schulz-Flory distribution (solid lines).

Hematite spindles of different aspect ratios ν are prepared and investigated within this work, the topological parameters of which are compiled in table 6.1. In general, the aspect ratio of the spindles is determined by the concentration of NaH_2PO_4 in the reaction mixture during synthesis, causing the anisotropic growth of the particles. During the formation of the ditrigonal-scalenohedral ($\bar{3}\ 2/m$) hematite, six equivalents of hematite crystallize per unit cell in the space group $R\bar{3}c$. Dark field electron microscopy shows, that the particles are crystalline single domain particles [29]. The hydrogenphosphate-ions from NaH_2PO_4 have an oxygen-oxygen distance $d_{\mathrm{O-O}} = 2.5$ Å. Due to this distance, adsorption of $H_2PO_4^-$ is preferred to planes parallel to the trigonal axis ($d_{\mathrm{Fe-Fe}} = 2.29$ Å) since the spacing is a better match than the Fe-Fe distance in planes perpendicular to the trigonal axis ($d_{\mathrm{Fe-Fe}} = 2.92$ Å). Due to this regio-specific adsorption, the spindles' growth preferably takes place in the less blocked direction of the rhombohedral axis and therewith the spindles aspect ratio ν increases with increasing concentration of NaH_2PO_4. This conclusion is in accordance with the results displayed in table 6.1. The parameter ϵ denotes the ratio $\epsilon = m(NaH_2PO_4)/m(FeCl_3)$. The amount of $FeCl_3$ is kept constant for every preparation, therefore ϵ is directly proportional to the amount of NaH_2PO_4 and therewith also proportional to the aspect ratio ν. The values given in table 6.1 for the represented hematite species show, that with increasing ϵ the values for ν also increase.
To perform and evaluate scattering experiments, a small polydispersity p of the investi-

gated nanoparticles is required, since the resulting scattering curves become less structured for highly disperse samples, which complicates their qualitative and quantitative interpretation. The polydispersities for the size distribution of length L and equatorial diameter σ_{eq} quantified by the Schulz-Flory parameter Z never exceed 15%. Hence, for all prepared samples, structured scattering patterns are obtained.

Table 6.1: Summarized results of size distributions of hematite particles determined by means of TEM, with aspect ratio ν and Schulz-Flory fit parameters r_0 and Z as well as calculated polydispersity p for each particle dimension. ϵ denotes the ratio $\epsilon = m(\mathrm{NaH_2PO_4})/m(\mathrm{FeCl_3})$ as introduced in section 5.1.

		r_0	ν	Z	p	ϵ
HEM 1	L	325.6 ± 0.9	7.0	113.9 ± 6.9	0.093	0.023
	σ_{eq}	50.3 ± 0.2		73.9 ± 4.2	0.116	
HEM 2	L	196.0 ± 0.8	3.4	79.2 ± 6.0	0.111	0.011
	σ_{eq}	61.6 ± 0.3		58.1 ± 4.7	0.130	
HEM 3	L	312.7 ± 1.3	5.2	80.8 ± 6.8	0.111	0.019
	σ_{eq}	61.2 ± 0.5		45.6 ± 4.9	0.146	
HEM 4	L	163.3 ± 0.4	2.9	147.3 ± 8.9	0.082	0.010
	σ_{eq}	55.7 ± 0.1		131.3 ± 7.3	0.087	

If exposed to an external magnetic field, shape anisotropic hematite nanoparticles align with their long axis perpendicular to the external field direction. This behavior makes the spindles a system of special interest as a filler particle for the hydrogel matrix system, since the mesostructure and therewith the mechanical properties of the resulting ferrogels can be influenced by the flux density and the direction of external magnetic fields.
Hematite spindles interact with an external magnetic field due to both, a permanent magnetic moment nearly perpendicular to the rotation axis [84, 85] in the direction of the crystallographic trigonal axis and an induced moment proportional to their negative, magnetic anisotropy $\Delta\chi = \chi_{\parallel} - \chi_{\perp}$. The interaction with an external magnetic field of the flux density B is given by

$$V(\vartheta_{\mathrm{P}}) = -\mu B \cos\vartheta_{\mu} - \frac{\Delta\chi V_{\mathrm{P}} B^2}{2\mu_0} \cos^2\vartheta_{\mathrm{P}}, \tag{6.3}$$

where $\chi_{\parallel}$ and $\chi_{\perp}$ denote the magnetic susceptibilities parallel and perpendicular to the spindles' director defined by its axis of revolution. The Zeeman contribution of the permanent moment is proportional to the cosine of the angle ϑ_{μ} enclosed between the direction of the field and the direction of the magnetic moment with the modulus μ. The contribution of the induced magnetic dipole is proportional to the particle volume V_{P} and the square B^2 of the flux density. Its angular dependence can be described by $\cos^2\vartheta_{\mathrm{P}}$, where ϑ_{P} denotes the angle between field direction and particle director. The direction of the

permanent magnetic moment is related to the particle director by an offset ϑ_{off} and can be obtained by an Eulerian tranformation in dependence on the Eulerian angles ϑ_{P} and χ_{P}.

Using (6.3), a Boltzmann ansatz for the ODF of the particles can be written as

$$f(\vartheta_{\text{P}}, \chi_{\text{P}}) = \frac{1}{Z} \exp\left[\frac{\mu B}{k_{\text{B}}T} \cos\left[\vartheta_{\mu}(\vartheta_{\text{P}}, \chi_{\text{P}})\right] + \frac{\Delta\chi V_{\text{P}} B^2}{2\mu_0 k_{\text{B}}T} \cos^2 \vartheta_{\text{P}}\right] \tag{6.4}$$

with the thermal energy $k_{\text{B}}T$ and the partition function Z as the integral of the exponential over the Eulerian angles $\varphi_{\text{P}}, \vartheta_{\text{P}}$, and χ_{P}. Here, particle interactions between the hematite spindles are neglected due to their large interparticle distances at very small volume fractions in the order of 10^{-3} compared to the interactions between individual particles with the external field.

The nematic order parameter S_2 (see equation (3.24)), calculated from the field dependent ODF of the hematite spindles determined by the evaluation of X-ray scattering data is used to quantify the alignment of the particles as a function of the flux density B. In figure 6.3, the field dependent order parameter is shown for the alignment of HEM 1 in an aqueous suspension. For complete alignment of the particles perpendicular to the magnetic field, the order parameter becomes $S_2 = -1/2$, whereas a completely random orientation results in an order parameter $S_2 = 0$. It is visible, that the alignment of the hematite particles in aqueous suspension increases with increasing magnetic flux densities.

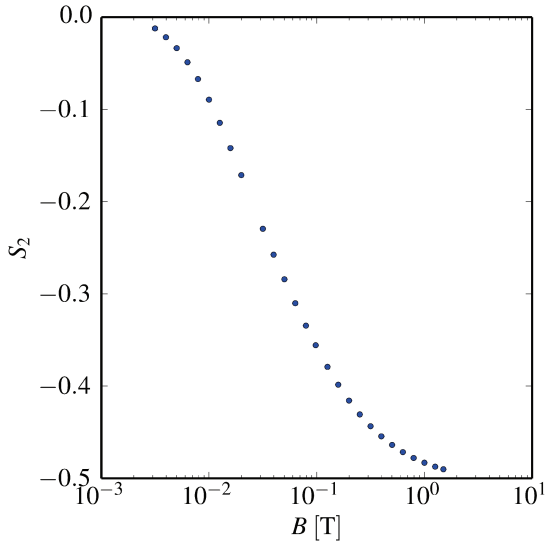

Figure 6.3: Order parameter S_2 for an aqueous suspension of HEM 1 in dependence of the flux density B of an external magnetic field.

6.2 poly(N-isopropylacrylamide) hydrogel

6.2.1 Characterization of structure and dynamics

Regarding to the matrix system, the aim of this work is to create a hydrogel, consisting not only of thermoresponsive, spherical pNIPAM particles but of thermoresponsive polymer spheres, additionally crosslinked by polymer chains in between which the hematite nanoparticles are embedded, as shown in figure 6.4 (lhs). A complex polymer network like this promises interesting – assumingly non-ergodic – dynamic behavior as well as the capability to spatially and physically interact with the hematite particles due to corresponding length scales.
Comparing the two given images, figure 6.4 confirms that a hydrogel matrix system in accordance to the intended model has indeed been prepared. In the TEM micrograph, polymer chain crosslinked pNIPAM spheres, specifically originating from sample pN 1 (see section 5.1), are visible.
For a basic characterization, the hydrogel samples are studied by means of Static Light Scattering (SLS) and dynamic light scattering (DLS). The results for the investigation of sample pN 1 are displayed in figure 6.5. Static light scattering experiments show a pronounced structure peak at $Q \approx 2 \times 10^{-2}\,\mathrm{nm}^{-1}$ corresponding to a correlation length of $d = 2\pi/Q \approx 315\,\mathrm{nm}$ in real space. This correlation length is in accordance to the polymer spheres' interparticle distances visible in figure 6.4, determined by means of TEM.

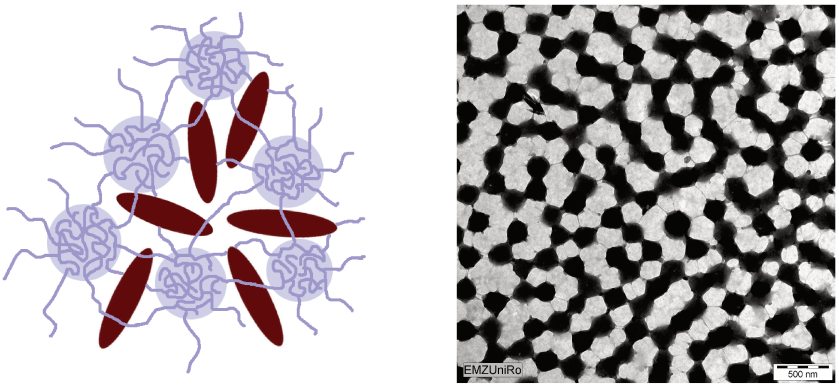

Figure 6.4: Schematic representation of the target hydrogel model consisting of pNIPAM hydrogel spheres crosslinked by polymer chains with embedded hematite particles (lhs). Exemplary TEM micrograph of an actual glutaric aldehyde (GA) crosslinked pNIPAM hydrogel (pN 1) presented in this work (rhs).

By means of DLS, characteristic field autocorrelation functions $g_1(\tau)$ for Q-values smaller, and larger than the correlation peak as well as for the correlation peak itself, are obtained [86]. In every correlation function, two well separated relaxation processes are visible, the relaxation rate of which differ by orders of magnitude. Short-time relaxations typically at 100 μs, also known as β-relaxation processes, are characterized by the

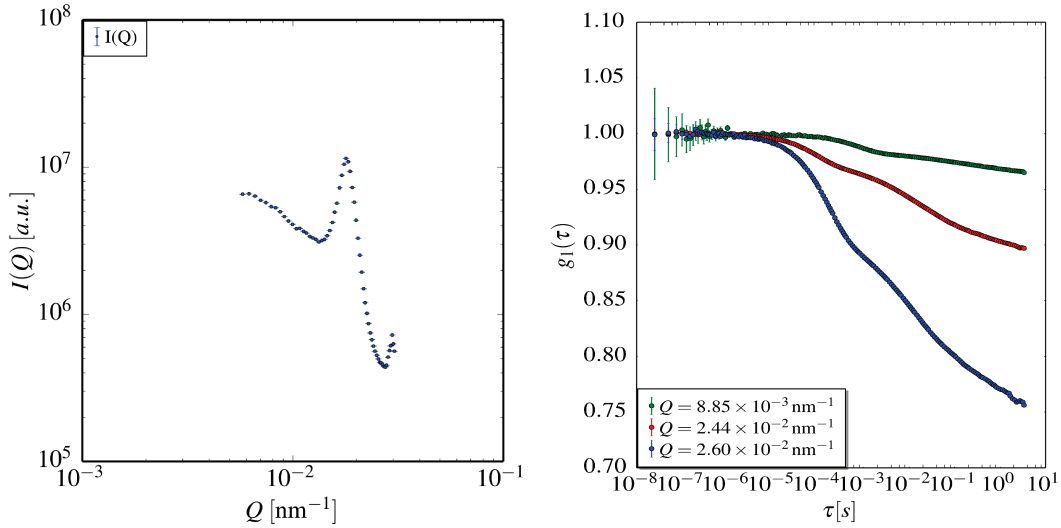

Figure 6.5: Scattering function of pNIPAM hydrogel matrix (pN 1) with distinct correlation peak at $Q \approx 2 \times 10^{-2}\,\mathrm{nm}^{-1}$ corresponding to a distance of $d \approx 315\,\mathrm{nm}$ in real space determined via SLS (lhs). Field autocorrelation functions $g_1(\tau)$ of pNIPAM hydrogel matrix (pN 1) for Q-values of scattering function before (green), at (red) and after (blue) correlation peak determined via DLS (rhs).

polymer spheres' localized movements within the confinement of the coordination cage. The chemical equilibrium for the formation of hemiaminals and imines, as relevant for the crosslinking reaction of pNIPAM and GA (see figure 5.1) in an acidic milieu is shifted towards the side of the educts. In the dynamic chemical equilibrium of the hemiaminal formation, it is possible that some crosslinking points are cut from and reattached to the polymer sphere after its' displacement. Therefore it can be stated, that the significantly slower α-relaxation process with relaxation times typically between 0.1 s and 10 s is characterized by diffusive escaping processes of a polymer sphere as a central particle from the confinement of its coordination cage. The nonergodicity of the polymer matrix, meaning the nonequivalence between time-averaged and ensemble-averaged time-autocorrelation functions [40], manifests itself by the existence of these two separated relaxation processes, as can be seen in figure 6.5 (rhs).

The Huggins equation

$$\eta_{\mathrm{red}} = \frac{\eta_{\mathrm{sp}}}{c} = \frac{\eta - \eta_0}{\eta_0 c} = [\eta] + k_{\mathrm{H}}\,[\eta]^2\,c \tag{6.5}$$

is used to relate the reduced viscosity of a dilute polymer solution to the concentration of a polymer solution [87]. Here, η denotes the viscosity of the polymer solution, η_0 the viscosity of the solvent, $[\eta]$ the intrinsic viscosity, c the concentration of the polymer

solution and k_H the Huggins coefficient. Mathematically, the Huggins equation is deviated from a virial expansion, truncated after the second term. Therefore, this approximation is only valid for small polymer concentrations.
In figure 6.6 the reduced viscosity η_{sp}/c in dependence on the polymer concentration c is shown for the samples pSys 2, pSys 5 and pSys 8, with different polymer volume fractions $\varphi_{pSys2} = 0.047$, $\varphi_{pSys5} = 0.09$ and $\varphi_{pSys8} = 0.13$ but constant crosslinking ratio $\chi = 0.05$. The red line is a guide to the eye showing that in the concentration range used there, already derivations from the Huggins' relation are observed. Because the virial expansion is truncated after the squared term, it is only valid for diluted polymer systems.

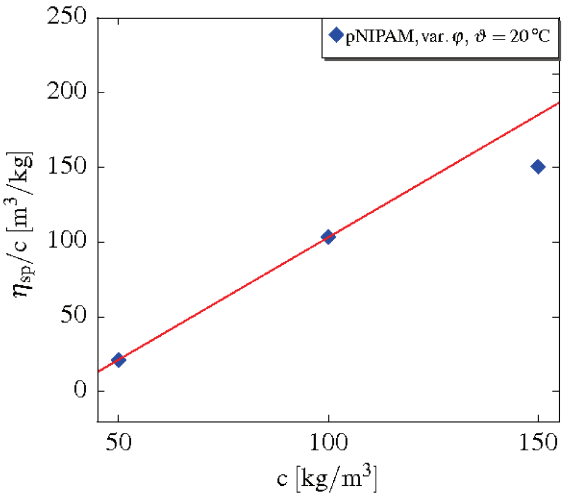

Figure 6.6: Ratio of specific viscosity η_{sp} and mass concentration c in dependence on the mass concentration c (blue diamonds) at a constant temperature $\vartheta = 20°C$. The red line is a guide to the eye, representing the linearity of the Huggins equation for low polymer concentrations.

6.2.2 Rheological characterization

Macroscopic properties of the pNIPAM matrix are determined by means of rotational and oscillatory shear experiments. Rotational shear experiments give information on the hydrogels' viscosity η in dependence on the temperature and shear rate $\dot{\gamma}$. The macroscopic viscoelastic properties are accessible via oscillatory shear experiments by evaluating the storage- and loss moduli G' and G'' in dependence on the frequency f and the shear deformation γ.

Rotational shear experiments pNIPAM matrix systems consisting of crosslinked polymer spheres are prepared systematically varying the polymer volume fraction φ and crosslinking ratio χ (see table 5.2). The influence of the polymer volume fraction φ and the crosslinking ratio χ on the viscous properties of hydrogels is investigated as a

function of temperature by means of rotational shear experiments at a constant shear rate $\dot{\gamma} = 2\,\mathrm{s}^{-1}$.
In figure 6.7, rheological results are shown for constant polymer volume fraction $\varphi = 0.046$ and varying crosslinking density of χ as well as for constant $\chi = 0.05$ and varying values of φ. The viscosity η of every hydrogel matrix decreases with increasing temperature due the polymers coil-to-globuli transition. The polymer structure collapses with increasing temperature and as a consequence, radius of gyration decreases. Considering Stokes equation $\xi = 6\pi\eta r$, smaller hydrodynamic radii result into smaller friction coefficients ξ, explaining the decreasing viscosities.
The radii of gyration decrease with increasing crosslinking ratio, too. Therewith, the viscosity of the polymer matrix decreases with increasing χ, as can be seen in figure 6.7, left. An increasing polymer volume fraction leads to increased radii and reduced interparticle distances between the linked pNIPAM spheres, both causing enlarged friction. Enlarged friction of the mesoscale structured entities cause increased macroscopic viscosity, as shown in figure 6.7, right.
In figure 6.8 the viscosity η of a pNIPAM hydrogel in dependence on the shear rate $\dot{\gamma}$ is shown. Here, the pseudoplastic, shear-thinning behavior, common to all pNIPAM hydrogels is exemplarily shown. Shear-thinning is typical for macromolecules, even for diluted polymer solutions. In the absence of shear stress, macromolecules form coils, possibly locking different polymer chains. Conformational reorganization under shear stress leads to reduced interaction between different polymer chains, which is the reason for decreasing friction and therewith decreasing viscosity.

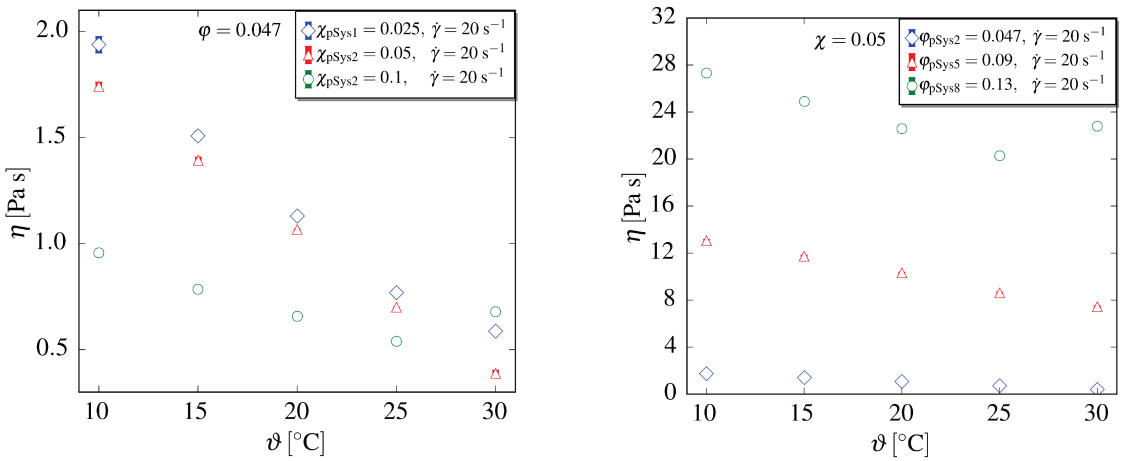

Figure 6.7: Temperature dependent viscosities of pNIPAM matrices determined at a constant shear rate of $\dot{\gamma} = 20\ \mathrm{s}^{-1}$. Lhs: pNIPAM samples of constant polymer volume fraction $\varphi = 0.047$ and varying crosslinking ratio $\chi_{\mathrm{pSys1}} = 0.025$ (blue diamonds), $\chi_{\mathrm{pSys2}} = 0.05$ (red tringles) and $\chi_{\mathrm{pSys3}} = 0.1$ (green circles). Rhs: pNIPAM samples of constant $\chi = 0.05$ and varying $\varphi_{\mathrm{pSys2}} = 0.047$ (blue diamonds), $\varphi_{\mathrm{pSys5}} = 0.09$ (red triangles) and $\varphi_{\mathrm{pSys8}} = 0.13$ (green circles).

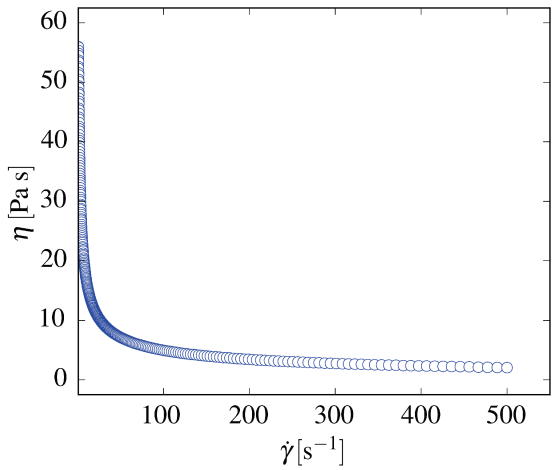

Figure 6.8: Shear rate dependent viscosity $\eta(\dot{\gamma})$ of pNIPAM hydrogel sample pSys 5 with $\chi = 0.05$ and $\varphi = 0.09$ determined at $\vartheta = 20\,^{\circ}\mathrm{C}$.

Oscillatory shear experiments Oscillatory shear experiments give information on the viscoelastic behavior of the pNIPAM samples via the storage - and loss moduli G' and G'' as an answer to a sinusoidal shear deformation γ. The resulting signal can be divided in a linear viscoelastic region (LVE region) and a nonlinear viscoelastic region (NLVE region). The LVE region is the region of small deformations, where the moduli G' and G'' are nearly independent of the deformation, representing the systems' properties without shear-induced structural changes.

In figure 6.9 storage and loss modulus in dependence on the shear deformation are shown for samples of varying crosslinking density χ as well as for varying polymer volume fractions φ, in accordance to the samples investigated by means of rotational shear experiments, as displayed in figure 6.7.
Regarding the LVE region, it is visible that an increment of the samples' crosslinking density results in a transition of the samples' behavior from a viscoelastic solid to a viscously dominated liquid-like system. For a high crosslinking density of $\chi = 0.1$ at a low polymer volume fraction of $\varphi = 0.047$, the loss factor is increased to $\tan\delta = G''/G' > 1$, indicating the fluid-like behavior of the sample (see figure 6.9, lhs). This finding can be explained by the decreasing sample viscosity for increasing χ at constant temperature. The critical deformation at which $\tan\delta = 1$, is shifted to lower values with increasing crosslinking ratio χ. Intense crosslinking between polymer chains causes high tension within the network structure of the hydrogels. The strain necessary to cause structural changes due to the overcoming of this tension therefore is reduced with increasing crosslinking ratio.
Increasing polymer volume fractions at a constant crosslinking density tend to shift the hydrogels' behavior from viscoelastic solid-like towards a viscously dominated fluid-like behavior, as can be interpreted by the decreasing ratio of G' and G'' within the LVE region (see figure 6.9, rhs). For intermediate crosslinking densities and low polymer volume fractions, elastically dominated solid-like behavior with $\tan\delta = G''/G' \ll 1$ is observed. With increasing polymer volume fraction, the ratio of G' and G'' decreases, therefore the loss factor can be found to be $\tan\delta \to 1$. Although for all φ investigated, within the LVE region $G' > G''$ it observed, it can be assumed, that further increase of φ results in a clear transition from solid-like to fluid-like behavior with $G'' > G'$ and $\tan\delta > 1$. This can be explained by the fact, that the increment of φ causes a rise in inner friction among polymer chains. Therewith the influence of the elastic moment resulting from crosslinked polymer chains is weakened, leading to increasingly viscous behavior of the hydrogel.Furthermore, the transition from LVE region to NLVE region and therewith the transition from solid-like to fluid like behavior due to shear-induced structural changes is shifted to higher values of deformation with increasing polymer volume fraction. The more polymer exists per unit volume, the higher the strain on the sample must be chosen to cause structural changes within the network structure of the matrix.

Figure 6.10 shows the shear deformation-dependent storage- and loss moduli for the sample pSys2 with $\chi = 0.05$ and $\varphi = 0.047$ for different shear frequencies. With increasing

frequency, and therewith increasing shear rates $\dot{\gamma}$ for constant amplitudes of deformation γ_0, the ratio of G' and G'' decreases. Only G'' and therewith the dissipated energy density shows a frequency dependency. Therefore, with increasing frequency, the hydrogel matrix shows progressing liquid-like behavior. Restoring forces, contributing to the elastic behavior of the sample are overcome by increasing forces of friction. This trend is found to be valid for all hydrogels investigated. The critical deformation for the transition from LVE region to NLVE region with $\tan\delta = 1$ is not influenced by the shear frequency.

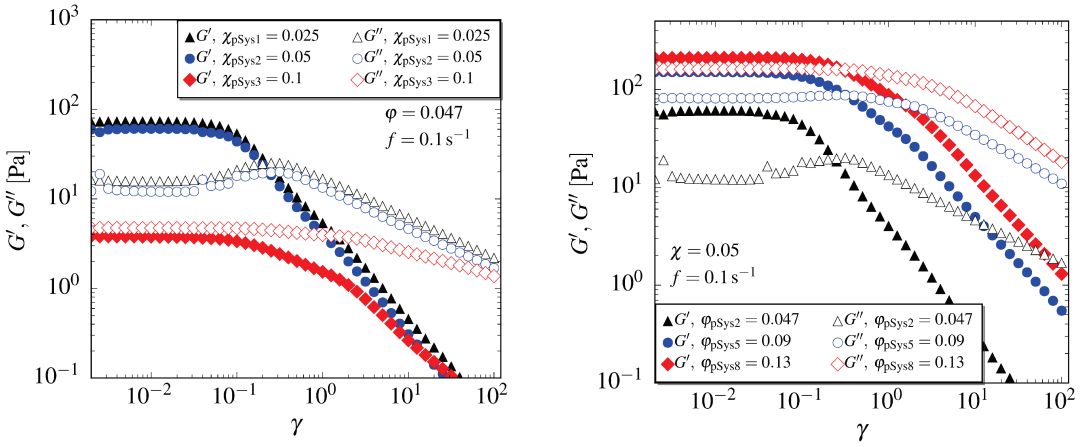

Figure 6.9: Storage- and loss moduli G' (filled symbols) and G'' (open symbols) in dependence on the shear deformation γ and at constant shear frequency $f = 1\,s^{-1}$ and $\vartheta = 20°C$. Lhs: pNIPAM samples of constant polymer volume fraction $\varphi = 0.047$ and varying crosslinking ratio $\chi_{pSys1} = 0.025$ (black triangles), $\chi_{pSys2} = 0.05$ (blue cirlces) and $\chi_{pSys3} = 0.1$ (red diamonds). Rhs: pNIPAM samples of constant $\chi = 0.05$ and varying $\varphi_{pSys2} = 0.047$ (black triangles), $\varphi_{pSys5} = 0.09$ (blue circles) and $\varphi_{pSys8} = 0.13$ (red diamonds).

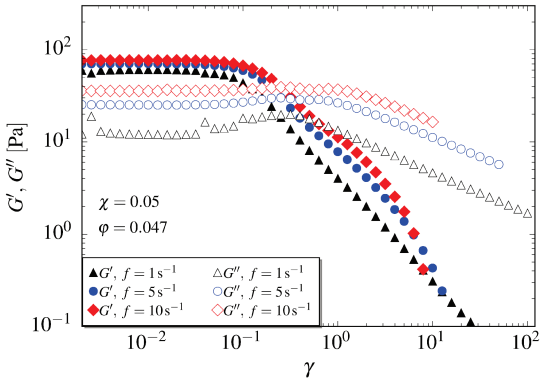

Figure 6.10: Storage- and loss moduli G' (filled symbols) and G'' (open symbols) in dependence on the shear deformation γ for hydrogel pSys 2 ($\chi = 0.05$ and $\varphi = 0.047$) for varying shear frequencies $f_1 = 1\,s^{-1}$ (black triangles), $f_2 = 5\,s^{-1}$ (blue circles) and $f_3 = 10\,s^{-1}$ (red diamonds) at constant temperature $\vartheta = 20°C$.

7 Rheological characterization of ferrogels

Rheological experiments serve as a method for the macroscopic characterization of the ferrogels' viscosity as well as their viscoelastic properties. As described before, rotational shear experiments allow the determination of the systems' viscosity in dependence of various parameters, as the temperature ϑ, the shear rate $\dot{\gamma}$ or the magnetic flux density B of an external magnetic field. Oscillatory shear experiments give insights into the viscoelastic behavior of the sample by the determination of the storage- and loss moduli G' and G'' in dependence on the shear deformation γ, the frequency f as well as the flux density B.
The characterization of hematite particles and pNIPAM hydrogels, the constituents of the composite ferrogels, is described in chapter 6. Hematite samples with different aspect ratios are topologically characterized and their alignment in external magnetic fields is investigated. Also the pNIPAM hydrogels used as a matrix for ferrogels are characterized. The influence of polymer volume fraction φ and crosslinking density χ on the viscoelastic properties is shown systematically in chapter 6. A common property of all crosslinked hydrogels is their nonergodicity visible by different relaxation processes observed by means of DLS experiments.
This chapter now focuses on the investigation of composites built from these two components. Of special interest are the changes to the mechanical properties of the hydrogel induced by the presence of shape anisotropic, magnetic nanoparticles. Particle-matrix interactions due to for example polymer entanglements of the spindles, as well as restoring forces resulting from the deformation of the matrix or torques induced by the application of external magnetic fields, are possible reasons for field induced changes of mechanical properties.

Table 7.1: pNIPAM samples, with varying polymer volume fraction φ and their crosslinking ratio χ, used as matrices for the preparation of pNIPAM-hematite composites

	φ	χ
pN 1	0.065	0.034
pN 2	0.065	0.028
pN 3	0.052	0.040

Three different hematite-pNIPAM composites with each a mass ratio of $\psi(\mathrm{HEM} : \mathrm{pNIPAM}) = 1 : 1$ are prepared to perform rheological experiments in order to characterize the change of mechanical properties. The pNIPAM hydrogels utilized as matrix systems for the composites, listed in table 7.1 differ in polymer volume fraction φ and crosslinking ratio χ. HEM 1 has been chosen as a composite component due to its large aspect ratio of $\nu = 7.0$. Presumably, an increasing anisotropy of the particles more likely induces changes of the mechanical properties of the hydrogel due to particle-matrix interactions. The aqueous suspension of HEM 1 added in a 1:1 mass ratio to the hydrogels to form the composites, has a mass concentration of $\mathrm{HEM1} = 10^{-3}$ wt% .

7.1 Rotational shear experiments

The influence of hematite nanoparticles within the polymer network to the viscosity η as a macroscopic mechanical property is shown by comparison of temperature dependent shear viscosity at $\dot{\gamma} = 20\,\mathrm{s}^{-1}$ of pure hydrogels and ferrogels, respectively. In order to compare systems with identical polymer volume fraction φ, as well as to ensure consistent viscosity data, for the determination of the pure hydrogels' viscosity, a to the amount of hematite suspension corresponding amount of water is added to the unloaded hydrogel sample before measurements.

In figure 7.1 the comparison of temperature dependent viscosities of two different composite materials to the corresponding unloaded hydrogels is shown. The hydrogel samples differ in polymer volume fraction ($\varphi_{\mathrm{pN}\,1} = 0.065$, $\varphi_{\mathrm{pN}\,3} = 0.052$) and crosslinking density ($\chi_{\mathrm{pN}\,1} = 0.034$, $\chi_{\mathrm{pN}\,3} = 0.04$) as can also be seen in table 7.1. For all samples the viscosity is decreasing with increasing temperature, as expected. This is caused by the characteristic coil-to-globule transition of the polymer network as described earlier in section 6.2.2.

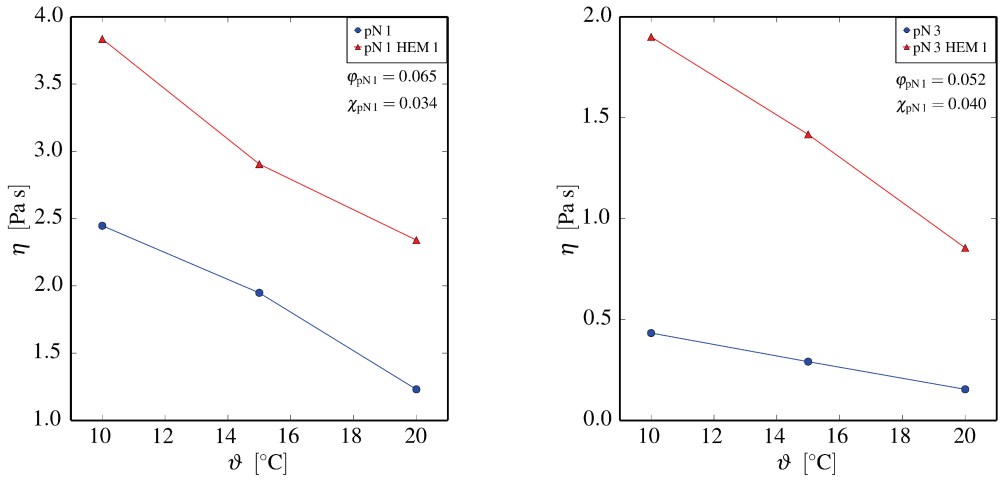

Figure 7.1: Comparison of temperature dependent viscosities η of pure pNIPAM hydrogels (blue circles) and pNIPAM-hematite composites (red triangles) at a constant shear rate $\dot{\gamma} = 20\,\mathrm{s}^{-1}$. The hydrogels differ in polymer volume fraction φ and crosslinking ratio χ.

Furthermore it can be seen, that the addition of hematite particles to the polymer network causes a significant rise in viscosity for both samples investigated. Increasing polymer volume fractions φ cause an increment of the systems viscosity. Contrarily, an increasing crosslinking ratio χ results in a reduced viscosity. In figure 7.1, a higher polymer volume fraction and a smaller value for the crosslinking ratio cause a higher viscosity of sample pN1 compared to smple pN 3, forming the initial baseline of the corresponding shear experiments. The viscosity for the composites (red) stays above the viscosity of the unloaded corresponding hydrogels (blue) for all temperatures investigated.
Entering the originally with water filled voids of the polymer network, the hematite particles cause an additional moment of friction due to their volume on the one hand and due to potential entanglements with the polymer matrix on the other hand. The additional friction of embedded hematite particles in the hydrogel network leads to an increased viscosity of the composites compared to pure hydrogels with the same polymer volume fraction.

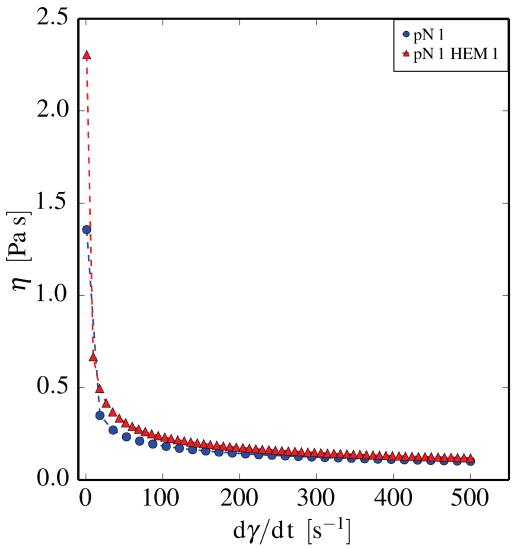

Figure 7.2: Shear rate dependent viscosity $\eta(\dot{\gamma})$ of pNIPAM hydrogel sample pN1 (blue circles) and composite pN 1 HEM 1 (red triangles) at $\vartheta = 20°\mathrm{C}$.

The shear-thinning or pseudoplastic behavior typical for polymers is observed both, for pure hydrogels and ferrogels, by means of shear rate dependent rheological experiments as shown in figure 7.2. Up to $\dot{\gamma} = 500\,\mathrm{s}^{-1}$, the composites' viscosity is enlarged, compared to the identical unloaded hydrogels. With increasing shear rate, however, the differences between composites and pure hydrogels vanish, if the viscosity η of the systems becomes smaller.

7.2 Oscillatory shear experiments

The influence of embedded hematite particles to the viscoelastic properties of composites compared to the unloaded polymer network is investigated by means of oscillatory shear experiments. As a result of these experiments, the storage and loss moduli G' and G'', with G' representing the elastically stored energy density and G'' representing the, caused by viscous friction, dissipated energy density, are obtained. As for the rotational shear experiments, to get insights into particle-matrix interactions, again composites and pure hydrogels of identical polymer volume fraction are compared.
In figure 7.3 storage- and loss moduli in dependence on the shear deformation γ at a constant shear frequency of $f = 1\,\mathrm{s}^{-1}$ and constant temperature of $\vartheta = 15°\,\mathrm{C}$ for the composite pN 2 HEM 1 and the corresponding hydrogel pN 2 are shown. It is visible, that the absolute values for G' as well as for G'' are slightly smaller for the composite (red) than for the unloaded hydrogel (blue) within the range of deformations measured. The reduced storage- and loss moduli in composites indicates opposite to the results of rotational

shear stress less dissipated energy due to friction in oscillatory shear experiments with limited deformation. Due to the continuously increasing deformation in rotational shear experiments, however, the structural reorganization due to shear stress is not comparable in both types of rheological experiments

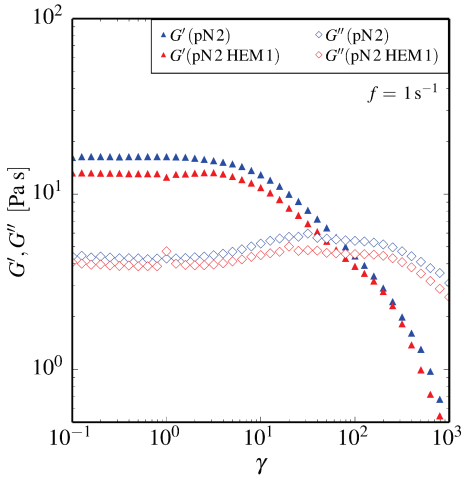

Figure 7.3: Storage- and loss moduli G' (filled symbols) and G'' (open symbols) in dependence on the shear deformation γ at constant shear frequency $f = 1\,\mathrm{s}^{-1}$ for unloaded hydrogel pN 2 (blue) and composite pN 2 HEM 1 (red) at constant temperature $\vartheta = 15°\mathrm{C}$.

Despite of that small difference, there seems to be no significant influence to the viscoelastic properties due to the addition of hematite particles to the polymer system. The ratio of storage and loss moduli within the linear viscoelastic region (LVE region) and therewith the loss factor $\tan\delta$ stays nearly constant. For both samples, the critical deformations characterizing the transition from LVE region to nonlinear viscoelastic region (NLVE region) and $\tan\delta = 1$ are nearly independent from the addition of hematite particles. These findings are representative for all investigated composite systems.
The influence of the shear frequency to the viscoelastic properties determined by deformation sweep experiments is shown in figure 7.4. Here, the composites pN 1 HEM 1 and pN 2 HEM 1 and corresponding unloaded hydrogels, differing in their crosslinking ratios with $\chi_{\mathrm{pN1}} = 0.034$ (lhs) and $\chi_{\mathrm{pN2}} = 0.028$ (rhs), are compared. Deformation sweep experiments are performed at two different frequencies $f_1 = 1\,\mathrm{s}^{-1}$ (squares) and $f_2 = 2\,\mathrm{s}^{-1}$ (stars), respectively. Regarding the storage modulus G', no distinguished difference between both frequencies, neither for the hydrogels nor for the corresponding composites, can be observed. Therefore, the storage modulus, also meaning the by mechanical deformation stored energy density, is virtually independent from the shear frequency as well as from particle-matrix interactions caused by the addition of hematite to the hydrogel network.

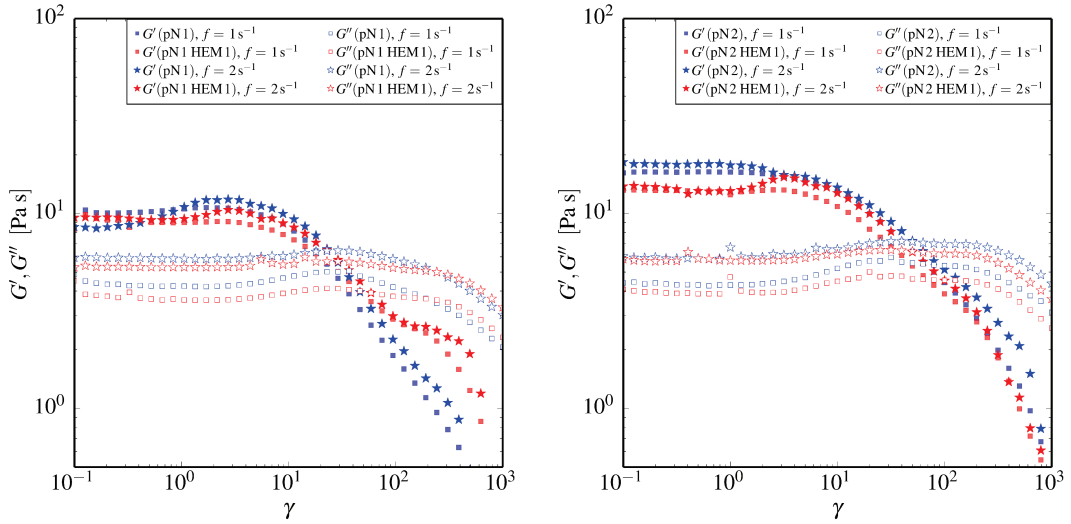

Figure 7.4: Storage- and loss moduli G' (filled symbols) and G'' (open symbols) in dependence on the shear deformation γ for two different shear frequencies $f_1 = 1\,s^{-1}$ (squares) and $f_2 = 2\,s^{-1}$ (stars). Two composites (red) and corresponding unloaded hydrogels (blue) of similar polymer volume fraction but different crosslinking ratios ($\chi_{pN1} = 0.034$ (lhs) and $\chi_{pN2} = 0.028$ (rhs)) are investigated at constant temperature of 15° C.

For both samples, the loss moduli G'' increase with increasing frequency. As a consequence, the ratio of G' and G'' is reduced with increasing shear frequency. For higher frequencies, the velocity of moving polymer- and hematite components and therewith the influence of inner friction is enlarged, explaining the increment of G'', quantifying inner friction, which is proportional to the angular velocity and therewith to the frequency.
Comparing the crosslinking ratios χ of both composites, the samples behave in accordance to the findings already described in section 6.2.2. Samples with higher crosslinking ratios tend to show more liquid-like behavior. Analyzing the values for G' and G'' in figure 7.4, the loss factor $\tan\delta = G''/G'$ is of typically by a factor two higher values for sample pN 1 HEM 1 (lhs) than for pN 2 HEM 1 (rhs).

7.3 Magneto-rheological experiments

In external magnetic fields, spindle-shaped hematite nanoparticles align with their long axis perpendicuar to the direction of the external magnetic field. This is due to interactions of a permanent dipole with the magnetic field as well as due to an induced magnetic moment caused by the anisotropy of the magnetic susceptibility tensor (see section 6.1). This field-induced orientational behavior serves as motivation for magneto-rheological experiments of pNIPAM-hematite composites. The already under field-free conditions observed consequences of particle-matrix interactions, concerning especially the viscosity

of the ferrogels, are influenced by the restriction of the particles' free rotation due to the field-induced orientation perpendicular to the long particle axis.

7.3.1 Rotational shear experiments in external magnetic field

The hydrogel composites, the characterization of which by means of rotational shear experiments is described in section 7.1, are additionally characterized by rotational shear experiments in presence of an external magnetic field. In figures 7.5 the temperature dependent viscosity $\eta(\vartheta)$ as well as the relative viscosity η/η_0, normalized to the zero-field viscosity η_0, are shown for the magnetic flux densities $B_0 = 0\,\mathrm{T}$, $B_1 = 0.1\,\mathrm{T}$ (squares), $B_2 = 0.2\,\mathrm{T}$ (diamonds) and $B_3 = 0.3\,\mathrm{T}$ (stars) for the composites pN 1 HEM 1 and pN 3 HEM 1 at a constant shear rate $\dot{\gamma} = 20\mathrm{s}^{-1}$.
With increasing temperature ϑ, the viscosity for both composites decreases, which is caused by the characteristic coil-to-globuli transition of the pNIPAM matrix. This effect is also observed for the viscosity of the composites exposed to an external magnetic field. Further regarding the absolute values of the viscosity it can be seen, that with increasing flux densities the viscosity of the composites increases. To quantify this effect, the relative viscosity is evaluated. An increase up to approximately 10% in presence of a field with a flux density of $B = 0.3\,\mathrm{T}$ parallel to the shear gradient is observed for both composites, pN 1 HEM 1 and pN 3 HEM 1. The increased viscosity is a consequence of the hindered rotational mobility of the shape-anisotropic particles due to their orientation in external magnetic fields. With increasing magnetic flux density, the rotational mobility of the particles is progressively restricted, causing increasing friction within the vorticity of the shear flow. As can be seen, especially for composite pN 1 HEM 1, the effect even intensifies with increasing temperature. For low temperatures, in the swollen polymer state, torques induced by viscous friction dominate magnetically induced torques of the particles. Therefore the relative changes in viscosity are small. With increasing temperature, the polymer volume decreases and the friction of particles, the rotation of which is restricted by the external field, becomes progressively important for the composites' viscosity.

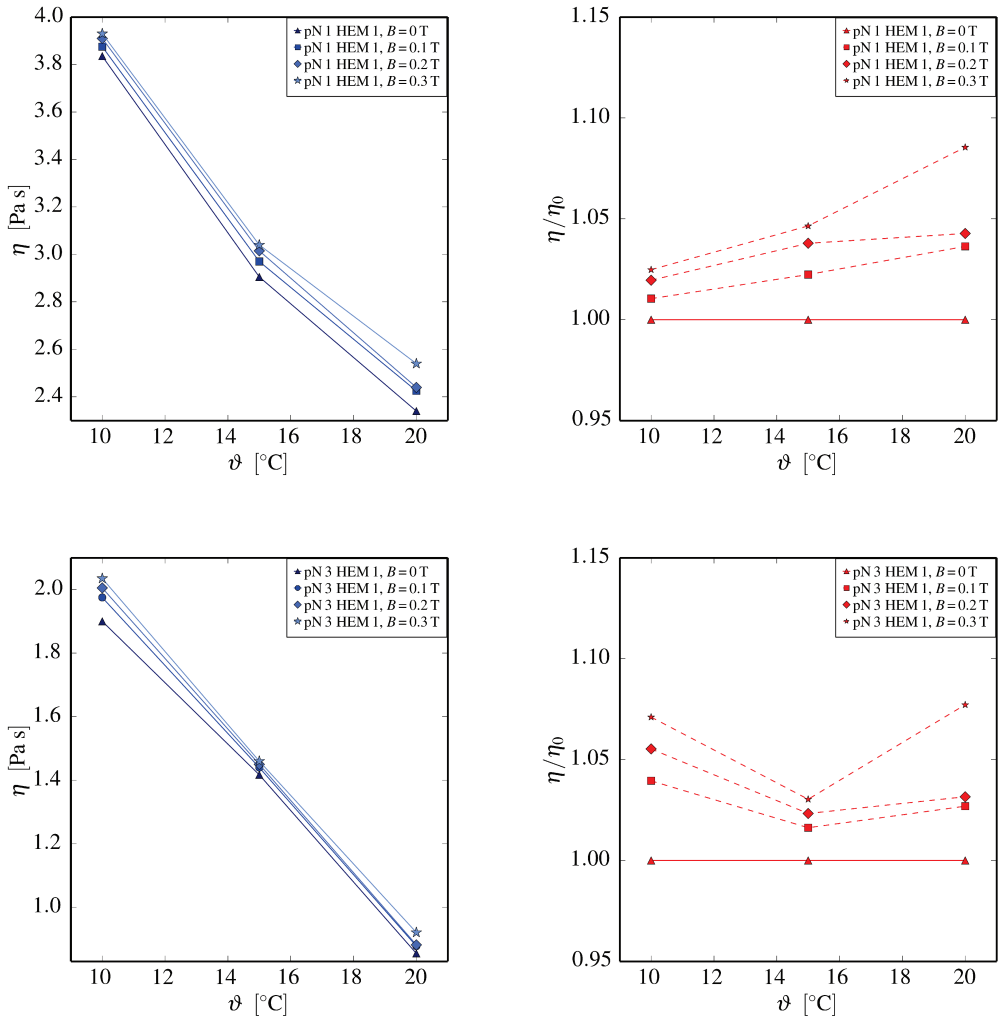

Figure 7.5: Temperature dependent viscosity η (blue) of pN 1 HEM 1 composite (upper row) and pN 3 HEM 1 composite (lower row) for varying magnetic flux densities B ($B_0 = 0\,\mathrm{T}$ (triangles), $B_1 = 0.1\,\mathrm{T}$ (squares), $B_2 = 0.2\,\mathrm{T}$ (diamonds) and $B_3 = 0.3\,\mathrm{T}$ (stars)) at a constant shear rate of $\dot{\gamma} = 20\,\mathrm{s}^{-1}$ (lhs). Relative changes of temperature dependent viscosity (red) of the same composites, normalized to the zero-field viscosity (solid line) for varying magnetic flux densities (rhs). During the experiments a temperature stability better than $\pm$ 0.15 K is monitored by means of a PT100 sensor in the lower plate.

7.3.2 Oscillatory shear experiments in external magnetic field

Composite materials already investigated in section 7.2 by means of oscillatory shear experiments are now exposed to an external magnetic field whilst performing an oscillatory

deformation sweep measurement. Referring to the results presented in the previous section, a change of the viscoelastic properties due to the restricted rotational mobility of the hematite particles in magnetic fields is the motivation for these experiments. Deformation sweeps are performed varying shear frequencies as well magnetic flux densities.

Variation of frequency at constant flux density In figure 7.6, deformation-dependent storage- and loss moduli G' and G'' are shown for the composites pN 1 HEM 1 (upper row) and pN 3 HEM 1 (lower row). Each experiment is performed at constant flux density B but varying shear frequency f. Results for oscillatory shear experiments at zero field and maximum field $B_{\max} \approx 680\,\mathrm{mT}$ are shown.
Regarding the storage modulus, G' seems to be independent of the applied shear frequency at constant magnetic flux density. No change can be observed for any of the composites within the range of deformation, comparing results of $f_1 = 1\,\mathrm{s}^{-1}$ and $f_2 = 2\,\mathrm{s}^{-1}$. For constant values of deformation, the loss modulus G'' increases with increasing frequency, corresponding to the findings in section 7.2. Here, the presence of an external magnetic field does not influence this behavior, as can be seen for both composites in figure7.6. Hence, for constant values of magnetic flux density and varying shear frequencies, the systems' response is purely viscous as characterized by the change of G''. The critical deformation for $\tan\delta$ is shifted in presence of an external magnetic field nearly by one order of magnitude to higher deformations but is independent from the variation of the shear frequency.

Variation of flux density at constant frequency In figure 7.7, deformation-dependent storage- and loss moduli G' and G'' are shown for the composites pN 1 HEM 1 (upper row) and pN 3 HEM 1 (lower row). Now, each experiment is performed at a constant shear frequency f whilst increasing the magnetic flux density B, to access a range, from zero to maximum external field. The storage modulus G' increases with increasing flux density for each composite and frequency. The loss modulus G'', however, is nearly independent of the flux density, especially at small deformations.
In an external magnetic field with increasing flux density, the rotational mobility of the shape-anisotropic particles is progressively confined, leading to the drastic increase of the storage modulus and therewith the elastically stored energy density, resulting from mechanical deformation of the hydrogel matrix. Phenomenologically, the embedded hematite particles can be seen as additional crosslinking points, which can be directed by external magnetic fields and therefore specifically influence the viscoelastic porperties of the composites.
The enlarged elastically stored energy density and the compared to the loss moduli increased storage moduli also cause a shift of $\tan\delta = 1$, corresponding to the transition from elastically dominated to liquid like behavior, to higher critical deformations with increasing flux density.

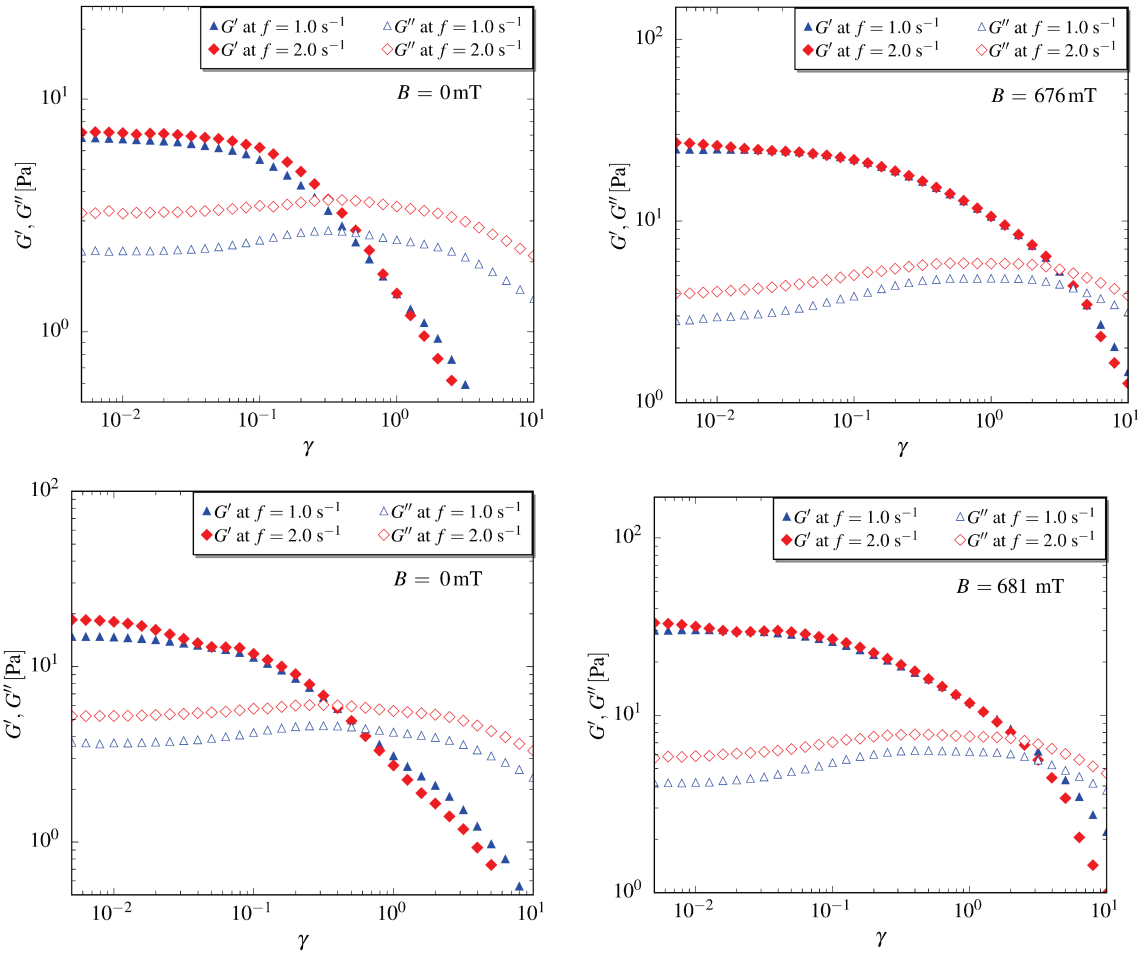

Figure 7.6: Storage- and loss moduli G' (filled symbols) and G'' (open symbols) in dependence on the shear deformation γ with at each case constant magnetic flux densities $B_0 = 0\,\mathrm{mT}$ (left column) and $B_{\max} \approx 680\,\mathrm{mT}$ (right column) for composites pN 1 HEM 1 (upper row) and pN 3 HEM 1 (lower row) at different frequencies $f_1 = 1\,\mathrm{s}^{-1}$ (blue triangles) and $f_2 = 2\,\mathrm{s}^{-1}$ (red diamonds) and a constant temperature of $\vartheta = 15^\circ\,\mathrm{C}\ \pm 0.15^\circ\,\mathrm{C}$.

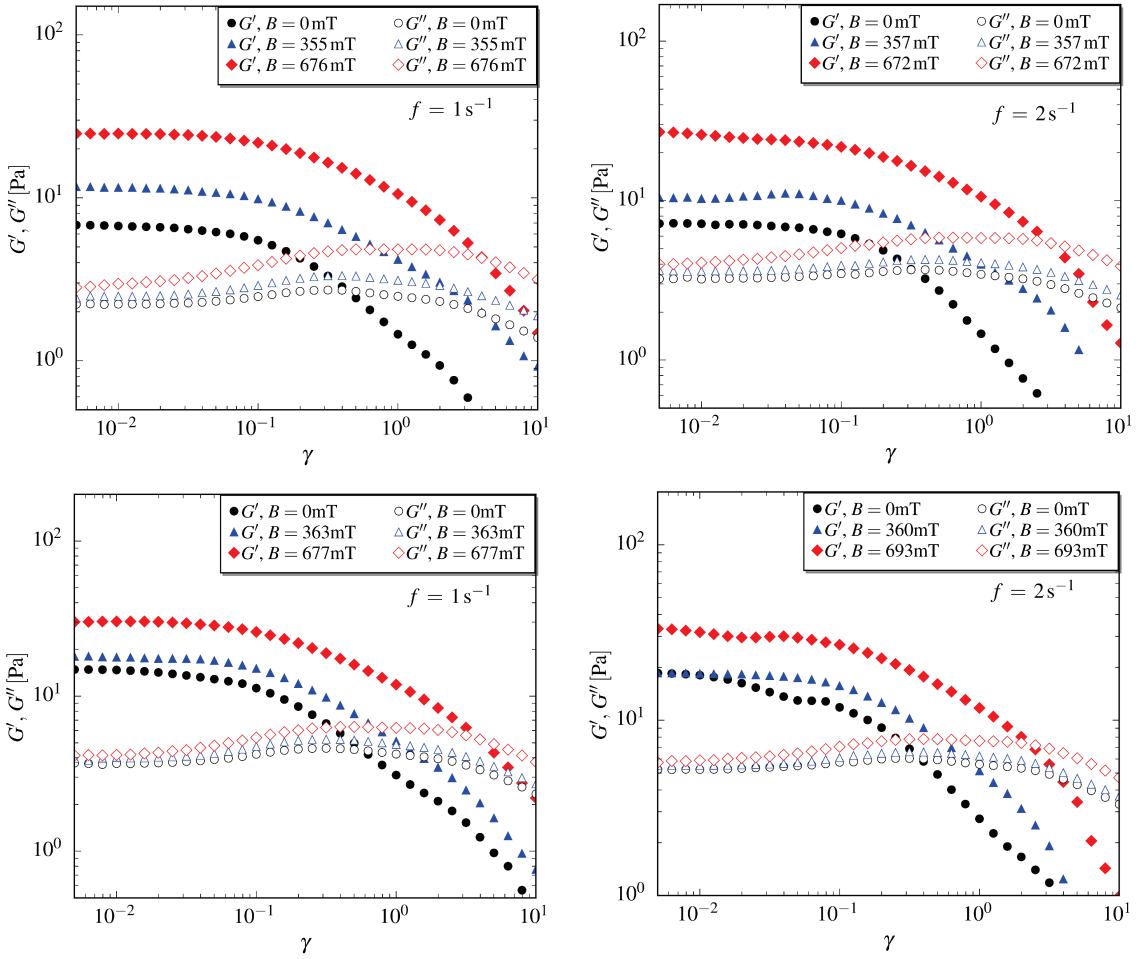

Figure 7.7: Storage- and loss moduli G' (filled symbols) and G'' (open symbols) in dependence on the shear deformation γ with at each case constant frequencies $f_1 = 1\,\mathrm{s}^{-1}$ (left column) and $f_2 = 2\,\mathrm{s}^{-1}$ (right column) for composites pN 1 HEM 1 (upper row) and pN 3 HEM 1 (lower row) at different magnetic flux densities $B_0 = 0\,\mathrm{mT}$ (black circles), $B_{\mathrm{mean}} \approx 360\,\mathrm{mT}$ (blue triangles) and $B_{\mathrm{max}} \approx 680\,\mathrm{mT}$ (red diamonds) and a constant temperature of $\vartheta = 15^\circ\,\mathrm{C}$ $\pm 0.15^\circ\,\mathrm{C}$.

In figure 7.8, as a control experiment, an unloaded hydrogel sample is exposed to a deformation dependent oscillatory shear experiment for zero-field conditions and at a magnetic flux density of $B = 312\,\mathrm{mT}$, similar to the previous experiments with the hematite-pNIPAM composites. It can be seen, that for both, storage- and loss moduli G' and G'' almost no influence of the presence of a magnetic field can be stated. Hence the previous findings of characteristic changes in the viscoelastic behavior of the composite materials are originating from the incorporation and the interactions of the magnetic nanoparticles in the hydrogel matrix.

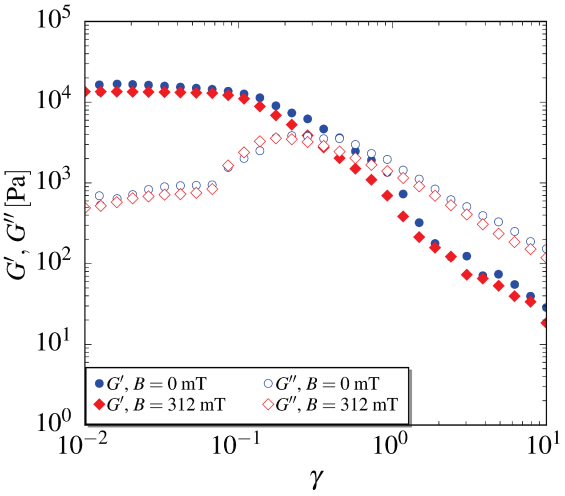

Figure 7.8: Storage- and loss moduli G' and G'' of an unloaded pNIPAM hydrogel pN1 at a constant shear frequency $f = 10\,\mathrm{s}^{-1}$ for flux densities $B_1 = 0$ mT (blue) and $B_1 = 312$ mT (red).

8 X-ray scattering investigations

8.1 Small angle X-ray scattering

Small angle X-ray scattering experiments are a powerful method to investigate the composites structure on mesoscopic length scales. Due to the low electron density of pNIPAM and water compared to hematite, the scattered intensity mainly results from the embedded particles. Within this chapter, in order to investigate particle-matrix interactions of the hematite spindles embedded in pNIPAM hydrogels, both, spindles in a hydrogel matrix and at the same number density, in aqueous suspensions are investigated and compared to each other.
Spindle-shaped hematite particles align with their long axis perpendicular to an external magnetic field. Scattering experiments with oriented particles are even more informative, since the scattering function shows in addition to its dependence on the modulus of the scattering vector a dependence on the direction of the scattering vector relative to the external magnetic field, in which the magnetic particles align. If the magnetic field is applied perpendicular to the primary beam, by using a 2d dectector, the dependence of the scattering function on the modulus as well as on the direction of the scattering vector can be determined simultaneously during the scattering experiment.
In this section, the orientational distribution functions (ODF) of hematite particles are derived from scattering experiments in presence of an external field with varying flux density. The ODFs are determined by analysis of the scattered intensity simultaneously in dependence on the modulus $|\mathbf{Q}|$ and the direction $\hat{\mathbf{Q}}$ of the scattering vector relative to the external field's direction. The scattering data displayed in the following are corrected for the background of a water filled capillary for aqueous suspensions and for that of a hydrogel filled capillary in the case of composites. Hence, the scattered intensity displayed, solely originates from the particles, either in water or hydrogel.
At the high brilliance beamline ID02 at the European Synchrotron Radiation Facility (ESRF) in Grenoble, hematite spindles of different aspect ratios $\nu_{\mathrm{HEM\,1}} = 7.0$ and $\nu_{\mathrm{HEM\,2}} = 3.4$ embedded in pNIPAM hydrogels of varying polymer volume fraction φ and crosslinking ratio χ as listed in table 8.1 are investigated in dependence on the flux density B of an external magnetic field.

Table 8.1: pNIPAM samples of varying polymer volume fraction φ and crosslinking ratio χ used to built composites investigated by means of small angle X- ray scattering.

	φ	χ
pN 1	0.065	0.034
pN 4	0.047	0.102
pN 5	0.047	0.056
pN 5$_{\mathrm{A}}$	0.024	0.056
pN 5$_{\mathrm{B}}$	0.012	0.056

In absence of a magnetic field the scattering patterns resulting from both, composites and aqueous suspensions, are, as can be seen in figure 8.1, completely isotropic, indicating a random orientation of the hematite spindles. With increasing flux density of an external magnetic field, the particles align with their long axes perpendicular to the field direction. With a scattering geometry using a magnetic field perpendicular to the primary beam, scattering vectors $\mathbf{Q}$ both, parallel and perpendicular to the external field $\mathbf{B}$, can be observed simultaneously.
With increasing flux density B, in the scattering patterns resulting from both, hydrogels and aqueous suspensions, an increasing anisotropy is visible (see figure 8.1). However, due to particle-matrix interactions, with the matrix restricting the alignment of the hematite particles, the composites' anisotropy is less pronounced than that of aqueous suspensions, as visible from false color representations of the scattered intensity at identical flux densities. The field-induced changes on the mesostructure of both, composites and aqueous suspensions, are completely reversible: typically 10 s after removing the external field, the scattering patterns are isotropic again.

The raw intensities detected with a 2d CCD detector (3840 x 3840 pixels) are pixelwise corrected for parasitic scattering, electronic background and detection efficiency. Subsequently, the detector plane is partitioned into 72 sectors with an acceptance of $\Delta\vartheta = \pm 2.5\,^{\circ}$ defining the direction of the scattering vector $\mathbf{Q}$ with respect to the external field (see figure 8.2). The modulus Q is related to a pixels' distance to the center of the scattering pattern. Therefore the detector is additionally partitioned in annuli of the width $\Delta r = 2.48 \times 10^{-4}\,\mathrm{m}$, corresponding to the diagonal of four pixels. Due to the cylindrical symmetry of the particles for the form factor the relation

$$P(Q, \vartheta_Q) = P(Q, -\vartheta_Q) = P(Q, \pi - \vartheta_Q) = P(Q, \pi + \vartheta_Q) \tag{8.1}$$

results, where ϑ_Q denotes the angle between the scattering vector $\mathbf{Q}$ and the particle director $\hat{\mathbf{u}}$. As a consequence, only 19 of 72 sectors, which are averages of four (respectively two for $\vartheta_{\mathrm{Q}} = 0$ and $\vartheta_Q = \pi/2$), are symmetrically independent. The data reduced

employing the symmetry relation (8.1) are used for the numerical analysis of scattering data.

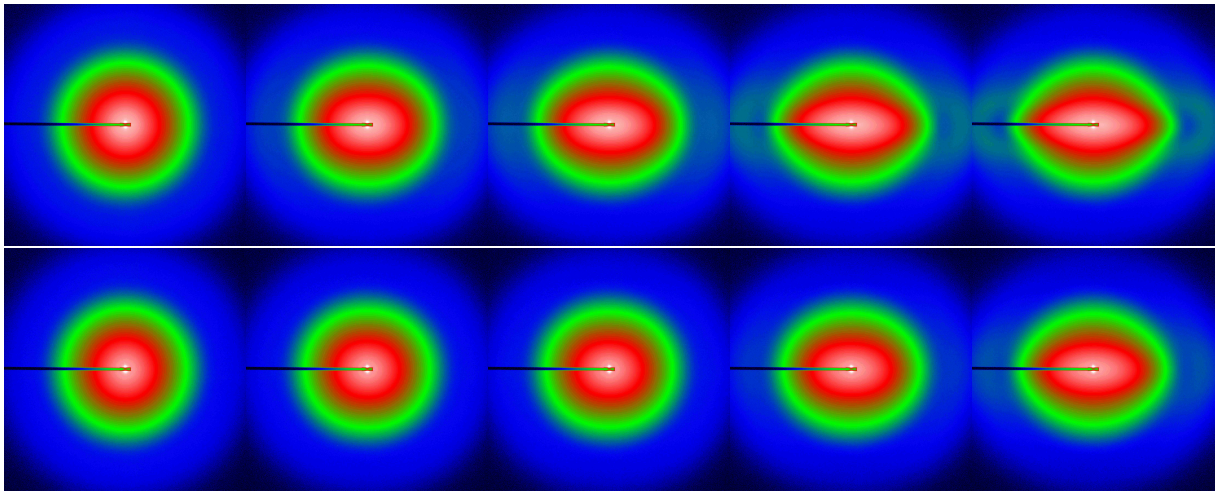

Figure 8.1: False color representation of the Small Angle X-ray Scattering resulting from aqueous suspensions (upper row) and composites (lower row) containing identical number densities of hematite particles. The magnetic flux density with horizontal field direction increases from left to right ($B_1 = 0$ mT, $B_2 = 10.0$ mT, $B_3 = 98$ mT, $B_4 = 1.00$ T, $B_5 = 1.50$ T).

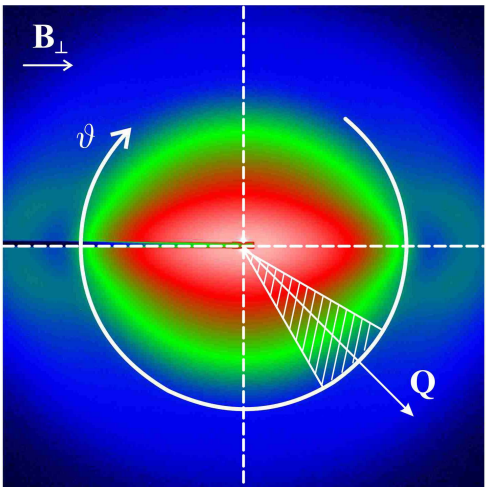

Figure 8.2: Data reduction by partitioning the detector in sectors.

Figure 8.4 shows sector averaged intensities of an aqueous suspension of HEM 2 with $\nu_{\mathrm{HEM\,2}} = 3.4$ and a PN 1 HEM 2 composite at different flux densities $B_1 = 0\,\mathrm{T}$, $B_2 =$

316 mT and $B_3 = 1.5$ T of the external field. Scattering functions are exemplarily displayed for the scattering vectors parallel ($\vartheta_Q = 0$) and perpendicular ($\vartheta_Q = \pi/2$) to the external magnetic field. In absence of an external magnetic field the orientation of the hematite spindles is random irrespective of the surrounding medium, either water or hydrogel. The scattering pattern resulting from such a spherically symmetric ensemble is radially symmetric, too. In this case, all sector averages are equal within experimental accuracy, independent of the angle ϑ_Q.
In presence of a magnetic field, due to the interaction with the particles' permanent and induced magnetic dipoles, the particles align. As a consequence, the spherical symmetry is reduced to a cylindrical symmetry as visible in the angular dependence of the sector averages for $B = 316$ mT and $B = 1.5$ T. With increasing anisotropy of the ODF the differences, maximum between directions parallel and perpendicular to the external field, increase as can be seen comparing scattering functions for field-free conditions. Both, for composites and aqueous suspensions the intensity differences increase with increasing flux density of the external magnetic field. Furthermore, it is obvious that differences between $\vartheta_Q = 0$ and $\vartheta_Q = \pi/2$ are more pronounced for the aqueous suspensions than for the pNIPAM-composites. While at 316 mT the particles in the hydrogel are still more or less statistically aligned, in water, the particles are nearly completely aligned perpendicular to the external field.
Both, for composites and aqueous suspensions, the scattered intensity in the direction $\mathbf{Q} \parallel \mathbf{B}$ ($\vartheta_Q = 0$) is more structured than for $\mathbf{Q} \perp \mathbf{B}$ ($\vartheta_Q = \pi/2$). Though the hematite spindles align with their long axis perpendicular to the external magnetic field a rotation around their short axis is still possible. Hence, the electron density for a particle rotating around its short axis resembles a disc with its' equatorial plane always perpendicular to the field direction and, as a consequence, $\mathbf{Q}$ always perpendicular to the particle director. Perpendicular to the field, however, a circular distribution of particle directors over 2π is observed, leading to an average orientation of the particle director with respect to $\mathbf{Q}$, smearing out the scattered intensity for $\vartheta_Q = \pi/2$. Applying a magnetic field parallel to the primary beam, as expected, a symmetric scattering pattern is observed, as can be seen in figure 8.3.

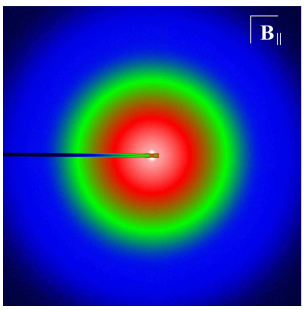

Figure 8.3: False color representation of the SAXS data from the composite pN 1 HEM 2 for a magnetic field if the flux density $B = 1.0$ T parallel to the primary beam.

The SAXS data are analysed assuming homogeneous, spindle-shaped particles with a Schulz-Flory size distribution of their equatorial radii. For simplicity of the model, a constant aspect ratio ν is assumed. Since the volume fraction of hematite spindles is typically $\varphi_{\mathrm{HEM}} = 10^{-3}$ and the interparticle distances are significantly larger than the particle size, particle-particle interactions can be neglected. As a consequence, with a structure factor $S(Q) \equiv 1$, the scattering data can solely be described by the form factor $P(Q, \vartheta_Q)$ of an ensemble of spindles underlying both, a size distribution, and an orientational distribution. With respect to the models' simplicity, the experimental data in figure 8.4 are described very well as a function of both, modulus and direction of $\mathbf{Q}$. Small deviations at $|\mathbf{Q}| \approx 0.2\,\mathrm{nm}^{-1}$ corresponding to length scales of $d \approx 30\,\mathrm{nm}$ in real space can be attributed to deviations of the real particle shape from the spindle model and neglecting a distribution of aspect ratios. Deviations at very small scattering vectors in the hydrogel composites result from weak aggregation of the hematite particles. Since the long axis of hematite spindles used in these experiments is typically $L = \nu r_{\mathrm{eq}} \approx 200\,\mathrm{nm}$, the orientation of the particles mainly influences the scattering function at $|\mathbf{Q}| \approx 2\pi/(200\,\mathrm{nm})$. In the latter $|\mathbf{Q}|$-range the model accurately describes the scattering data.
Employing the Boltzmann approach for the ODF (see equation 3.22), the nematic order parameter S_2 is obtained by canonically averaging the distribution function (see equations (3.22) and (3.24)). S_2 quantifies the field-induced alignment of the particles in dependence on the flux density of the applied field. For complete alignment of the particles perpendicular to the external field, $S_2 = -1/2$ is expected, while the order parameter approaches $S_2 = 0$ for a random orientation.
Figure 8.5 shows the field dependent nematic order parameter of aqueous suspensions of HEM 1 with $\nu = 7.0$ and HEM 2 with $\nu = 3.4$. In figure 8.6 and figure 8.7 the field-dependent order parameters of aqueous suspensions and hydrogel-composites containing identical number densities of hematite spindles are compared. Both, for aqueous suspensions and hydrogel-composites, a field-induced isotropic-nematic transition is observed, although in the hydrogel-composites the nematic alignment is less pronounced than in aqueous suspensions.

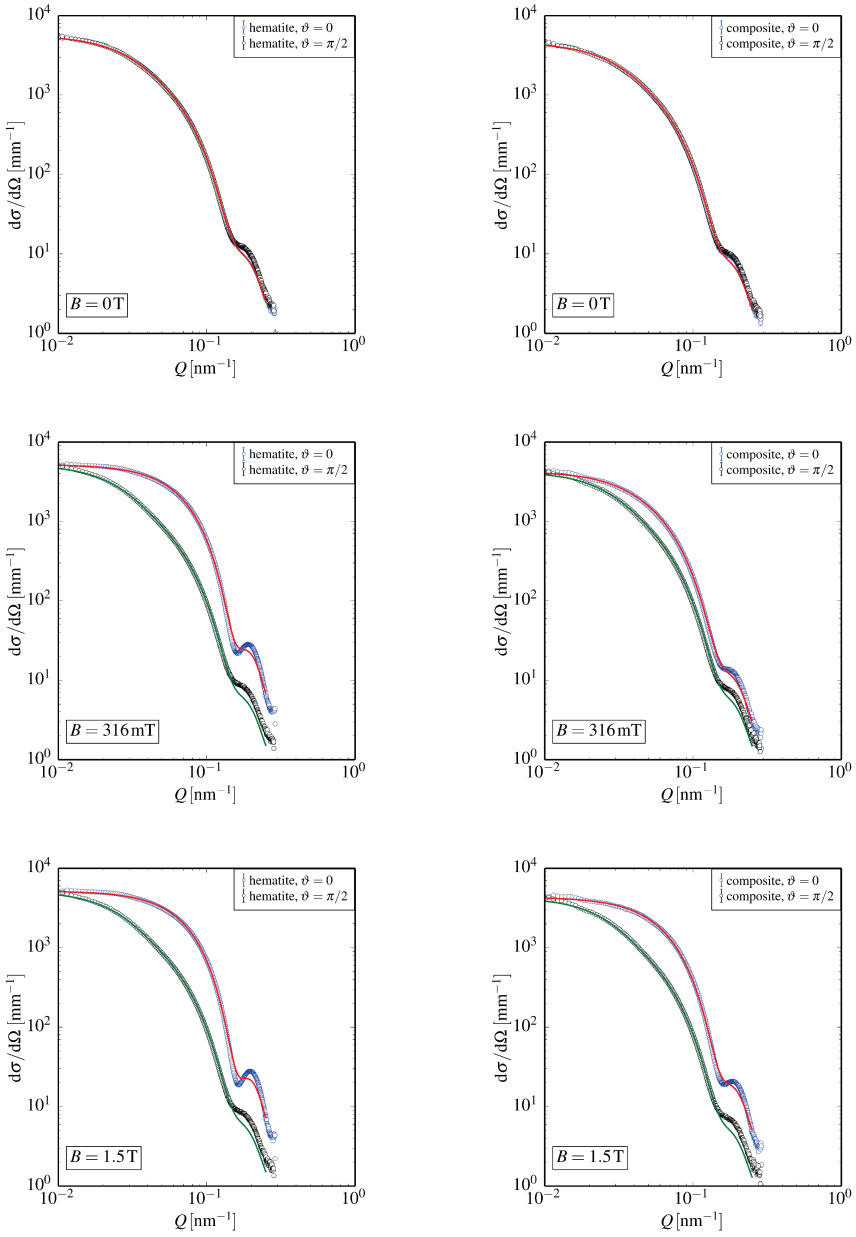

Figure 8.4: Sector-averaged mean intensities of an aqueous suspension of HEM 2 with $\nu_{\mathrm{HEM\,2}} = 3.4$ (left colum) and a pN 1 HEM 2 composite (right column) exemplarily displayed for the scattering vector parallel ($\vartheta_Q = 0$, blue circles) and perpendicular ($\vartheta_Q = \pi/2$, black circles) to the external magnetic field for varying flux densities $B_1 = 0\,\mathrm{T}$, $B_2 = 316\,\mathrm{mT}$ and $B_3 = 1.5\,\mathrm{T}$. The solid lines are the results of a simultaneous least-squares fit of the complete reduced data set with $0 \leq \vartheta_Q \leq \pi/2$ employing a model of Schulz-Flory distributed spindles in an external field.

Figure 8.5 shows the dependency of the field-induced isotropic-nematic transtion of the hematite in spindles in dependence on the particles' aspect ratio ν. It is obvious, comparing S_2 for both species, that an increasing anisotropy of the particles and therewith increasing volume and magnetic moment favors the field-induced alignment. The graphs $S_2(B)$ show a steeper slope at low flux densities for particles of higher aspect ratio.
In figure 8.6 the influence of the crosslinking ratio χ on the particle-matrix interactions is visible by the investigation of composites pN 4 HEM 2 with $\chi = 0.102$ and pN 5 HEM 2 with $\chi = 0.056$ and an aqueous suspension of HEM 2 as a reference. In hydrogels with identical polymer volume fraction $\varphi = 0.047$, the nematic alignment is progressively hindered with increasing crosslinking ratio χ. As shown in section 6.2.2, increasing crosslinking ratios result in increasing elasticity of the hydrogel matrix causing restoring torques to the magnetically induced angular displacement of the hematite particles embedded in the hydrogel. With increasing crosslinking ratio χ and therewith larger elasticity, the isotropic-nematic transition of particles in composites is shifted to larger flux densities.
In figure 8.7, the influence of the polymer volume fraction φ of the hydrogel matrix to the isotropic-nematic transition at constant crosslinking ratio χ is displayed for the composites pN 5 HEM 1 ($\varphi = 0.047$), pN 5_{A} HEM 1 ($\varphi = 0.024$), pN 5_{B} HEM 1 ($\varphi = 0.012$) and an aqueous suspension of HEM 1 ($\nu = 7.0$) as a reference. An increasing polymer volume on the one hand also induces a rising elasticity of the hydrogel matrix and on the other hand decreases the size and volume of water filled cavities, in which the particles can move freely. Both effects lead to the result, that the nematic alignment of the magnetic spindles is progressively hindered with increasing φ of the polymer matrix.
Both, in aqueous suspensions and hydrogel composites, an equilibrium mesostructure is obtained within several seconds and the alignment is completely reversible. This clearly indicates that the hindered alignment is a result of the viscoelasticity of the composites. Purely viscous friction would prolong the equilibration but result after infinite time in the same time-averaged mesostructure.

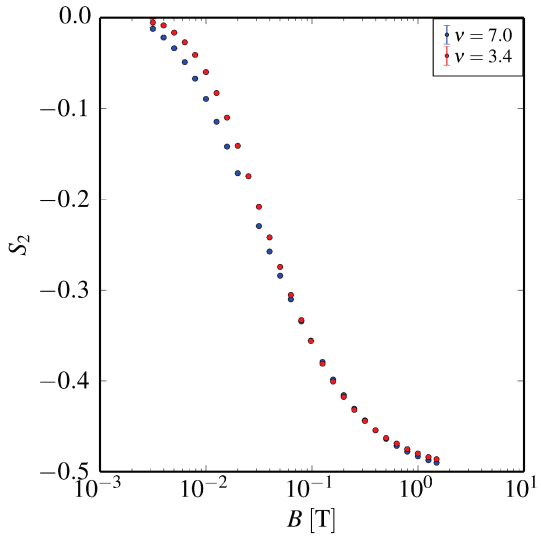

Figure 8.5: Order parameter S_2 of aqueous suspensions of HEM 1 ($\nu = 7.0$, blue circles) and HEM 2 ($\nu = 3.4$, red circles) in dependence on the flux density B of an external magnetic field.

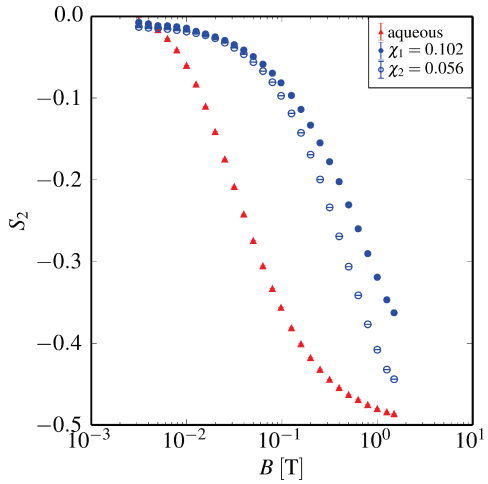

Figure 8.6: Order parameter S_2 of an aqueous suspension of HEM 2 (red triangles) and hydrogel composites pN 4 HEM 2 and pN 5 HEM 2 in dependence on the flux density B of an external magnetic field. Both hydrogels contain an identical polymer volume fraction $\varphi = 0.047$ at different crosslinking ratios $\chi_{1,\mathrm{pN4}} = 0.102$ (filled blue circles) and $\chi_{2,\mathrm{pN5}} = 0.056$ (open blue circles).

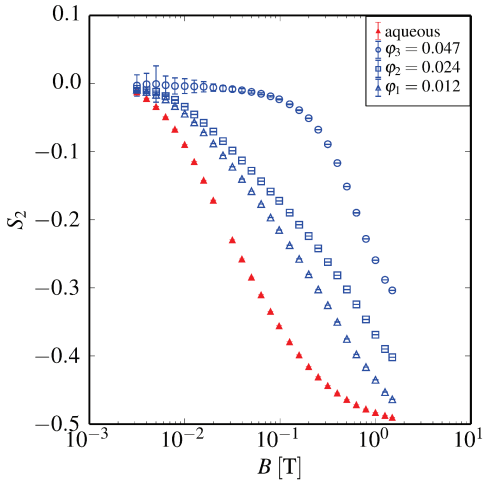

Figure 8.7: Order parameter S_2 of an aqueous suspension of HEM 1 (red triangles) and hydrogel composite pN 5 HEM 2 in dependence on the flux density B of an external magnetic field. The hydrogel, before forming the composite, is diluted with water to obtain varying volume fractions $\varphi_1 = 0.012$, $\varphi_2 = 0.024$, $\varphi_3 = 0.047$ (open blue symbols) at identical crosslinking ratio $\chi = 0.056$.

8.2 Rheological small angle X-ray scattering

In the previous section, small-angle X-ray scattering experiments gave insights to particle-matrix interactions within the ferrogels. In absence of an external magnetic field, the particles are statistically orientated in the matrix, as obvious from spherically symmetric SAXS patterns. Due to the magnetic moment of spindle-shaped hematite particles, in an external magnetic field a torque is applied to the anisotropic particle, leading to a deformation of the polymer network. This leads to a hindered nematic alignment of the magnetic rods embedded in the hydrogel matrix.
In the opposite way, within the vorticity of a laminar shear flow, the polymer network rotates. Hereby the orientational distribution function (ODF) of statistically aligned rods changes due to interactions with the polymer matrix, since the typical mesh size in the hydrogel network is comparable to or smaller than the length of the particles (see chapter 6). Furthermore, in section 7.1 is described, how the composites' transition from linear viscoelastic (LVE) to nonlinear viscoelastic (NLVE) behavior is shifted towards lower deformations with increasing shear frequency in oscillatory shear experiments.
RheoSAXS experiments presented in this section, aim to investigate the influence of the networks' vorticity to the orientational distribution function of the hematite spindles. At the coherence beamline P10 the RheoSAXS setup as described in section 5.3 is used to

investigate the rheological properties of two different hematite species *HEM 3* and *HEM 4* with varying aspect ratios $\nu_{\mathrm{HEM3}} = 5.2$ and $\nu_{\mathrm{HEM4}} = 2.9$, embedded in a hydrogel matrix consisting of *pSys 6* with a polymer volume fraction $\varphi = 0.09$ and a crosslinking ratio $\chi = 0.1$. Additionally, the number density of hematite embedded in the hydrogel matrix has been varied by tuning the composites' polymer mass ratio $\psi = m(\mathrm{pSys})/m(\mathrm{HEM})$. Oscillatory shear experiments in dependence on the shear frequency f and the shear deformation γ at constant temperature ϑ are performed to investigate the viscoelastic behavior of these composites.

As a first step, particles are aligned with their long axis parallel to the shear plane and perpendicular to the shear gradient and the direction of the primary beam by a radial shear flow induced by compressing drops of isotropic composites between the rheometer plates.
The velocity field in laminar shear flow in x-direction can be described as

$$\mathbf{v}(x,y,z) = \begin{pmatrix} v_0 + z\dot{\gamma} \\ 0 \\ 0 \end{pmatrix} \tag{8.2}$$

with the shear gradient $\partial v_x/\partial z = \dot{\gamma}$. The rotation of the velocity field

$$\begin{aligned} \text{curl } \mathbf{v}(x,y,z) &= \begin{pmatrix} \frac{\partial}{\partial x} \\ \frac{\partial}{\partial y} \\ \frac{\partial}{\partial z} \end{pmatrix} \times \mathbf{v}(x,y,z) \\ &= \begin{pmatrix} 0 \\ \dot{\gamma} \\ 0 \end{pmatrix} \end{aligned} \tag{8.3}$$

results in an angular velocity with a rotation axis in y-direction.
Due to the circular symmetric alignment, the particle directors are randomly aligned in the $x-y$-plane. Particles with a director parallel to the y-direction rotate in the vorticity of the shear flow around their long axis without influence to their scattering power, since the orientation of their particle director does not change with respect to the scattering vector (see figure 8.8, lhs). Particles aligned in x-direction, however rotate around their short axis and change their orientation with respect to the scattering vector $\boldsymbol{Q}$ (see figure 8.8, rhs). By deflection of a part of the initially radially symmetric ensemble, in shear flow, anisotropy evolves.
In oscillatory shear experiments, periodic fluctuations of the scattered intensity from isotropic to anisotropic scattering pattern are observed. The temporal fluctuations between circular symmetric and anisotropic ensembles are visible especially in differences

of scattered intensity. In figure 8.9, differences of scattered intensities under oscillatory shear stress and those of the initial configuration without shear stress are displayed.

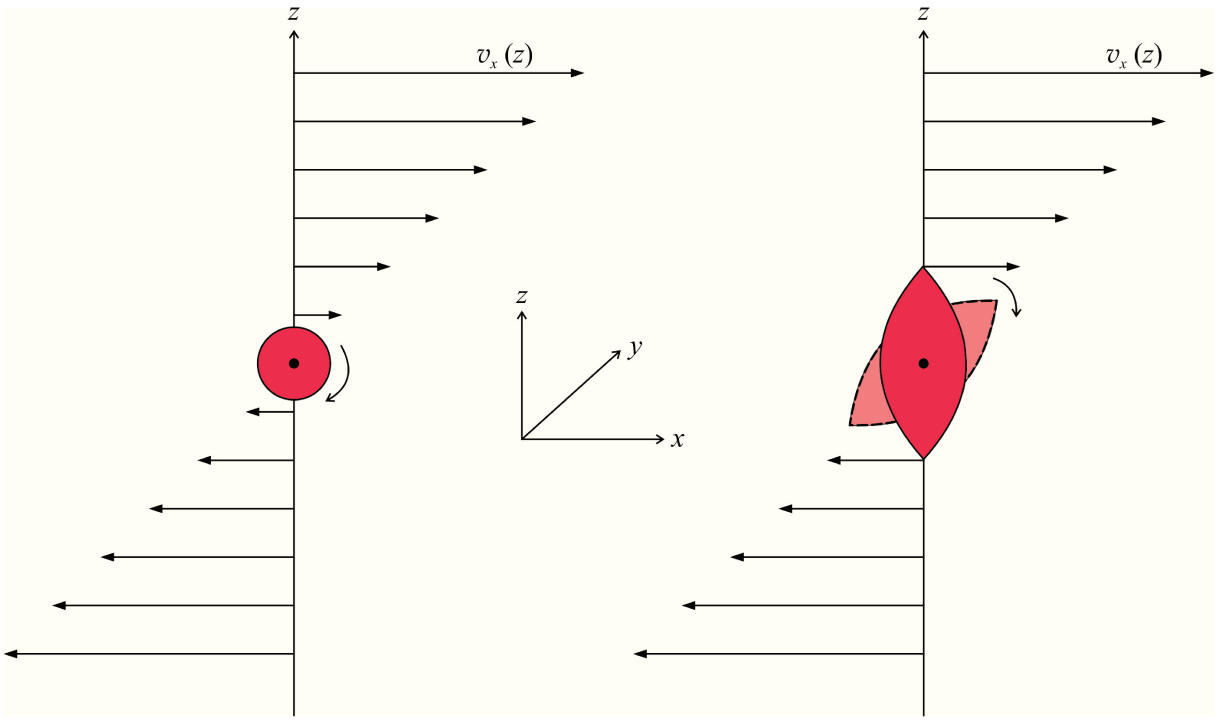

Figure 8.8: Rotation of axially symmetric particles in the vorticity of a shear flow at different particle orientations with respect to the shear gradient.

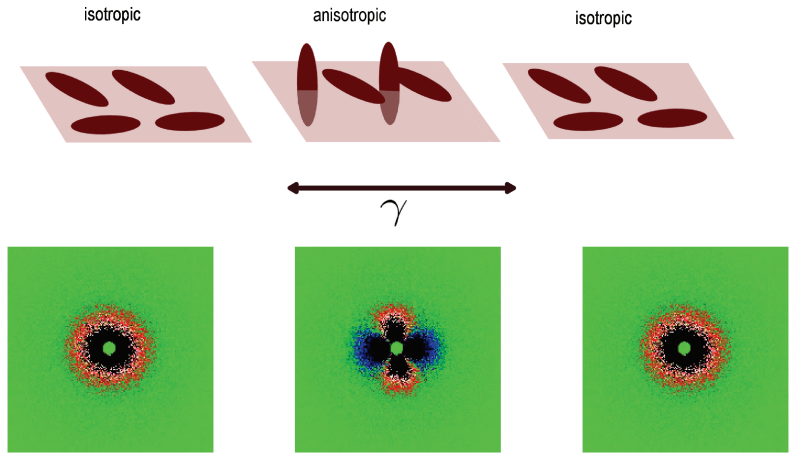

Figure 8.9: Differences of scattered intensities under oscillatory shear stress and those of initial configuration without shear stress.

Similar to the procedure in section 8.1, the scattering signal is evaluated by partitioning the detector plane in multiple sectors and averaging the intensity of each sector. Hence, an angle dependent intensity $I(\vartheta)$ is obtained. In the following, only scattering functions $I(Q)$ for sectors parallel ($\vartheta = 0$) and perpendicular ($\vartheta = \pi/2$) to the shear flow are shown. In figure 8.10 scattering functions of the composite pNS 6 HEM 25 with a polymer mass ratio $\psi = 4$ are shown for different rheometer plate deflection angles Φ, which corresponds to the phase of deformation. Plate deflection angle and deformation are related via the expression

$$\gamma = \frac{\Phi r}{h} \tag{8.4}$$

with r denoting the radius at which the primary beam hits the sample and h the height of the gap between the two measuring plates. The maxima of the sinusoidal function $\Phi(t)$ each represent the maximum plate deflection, also corresponding to the maximum deformation of the sample. $\Phi = 0$ corresponds to a nondeformed state of the sample. For maximum deflection, the out of shear plane alignment of the particles and therewith the anisotropy of the scattering patterns are maximal, at zero-crossing, all particles are realigned within the shear plane and the corresponding scattering pattern becomes isotropic again.

In scattering functions from anisotropically aligned ensembles, intensity differences between sectors parallel ($\vartheta = 0$) and perpendicular ($\vartheta = \pi/2$) to the shear flow are observed. This is the case for scattering data obtained for deflection angles $\Phi = 2.09\,^\circ$ and $\Phi = -2.14\,^\circ$ close to the maximum plate deflection (see figure 8.10, lhs). Out of plane alignment of the hematite particles here results in angular dependent, anisotropic scattering signals. Deflection angles $\Phi = 0.48\,^\circ$ and $\Phi = -0.53\,^\circ$ represent plate deflection close the the point zero-crossing. The corresponding scattering functions show nearly no differences for $\vartheta = 0$ and $\vartheta = \pi/2$, since almost all particles are realigned within the shear plane at this point, resulting into an isotropic scattering pattern (see figure 8.10, rhs). Concluding these findings, it can be stated that the observed intensity fluctuations are in phase with the deformation.

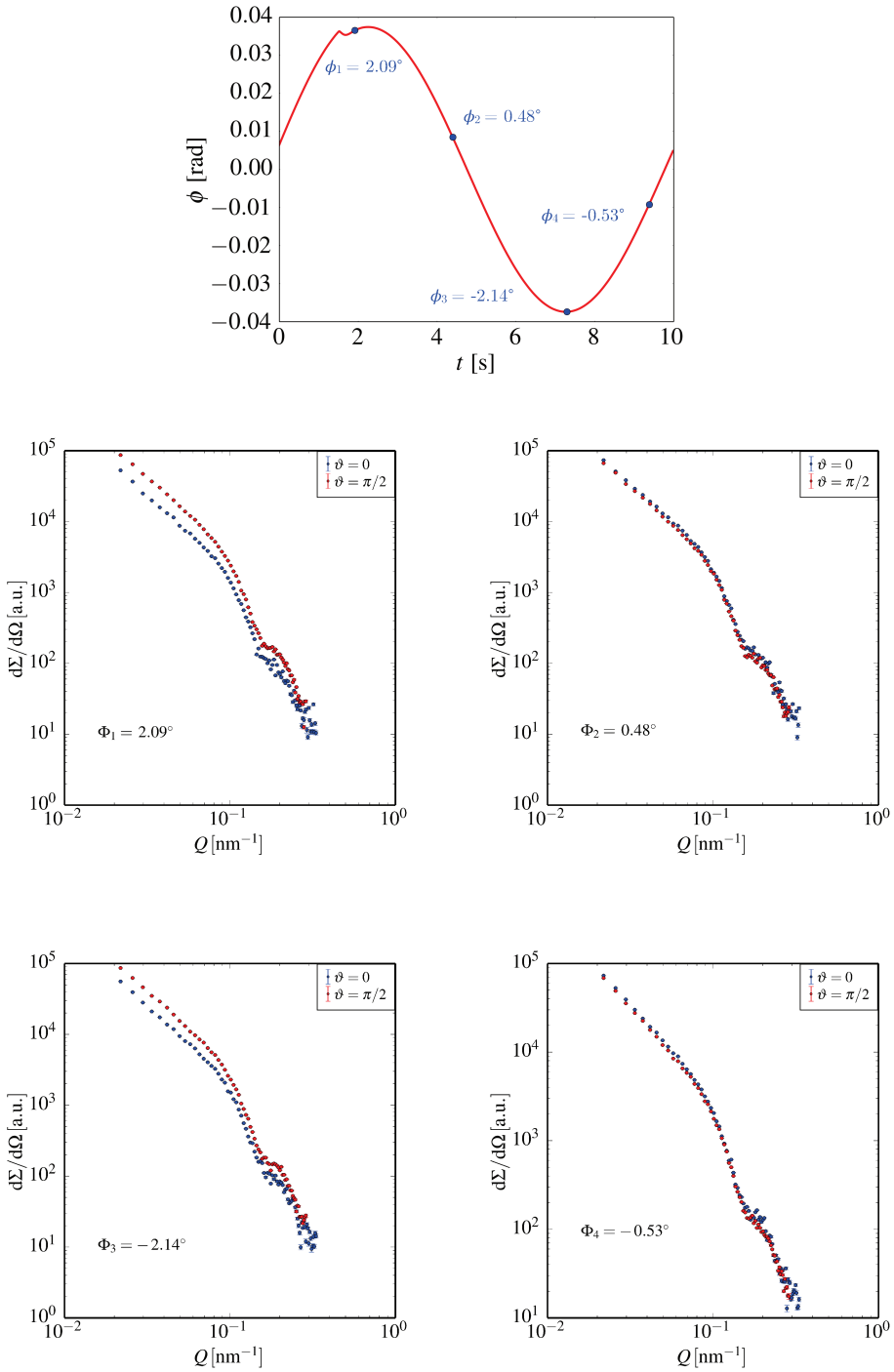

Figure 8.10: Plate deflection angle Φ in dependence on the time t to illustrate one period of deformational shear stress during oscillatory shear experiments (upper row). Sector averaged mean intensities of a hematite-pNIPAM composite of polymer mass ratio $\psi = 4$ for sectors parallel ($\vartheta = 0$) and perpendicular ($\vartheta = \pi/2$) to the shear flow at different deflection angles Φ.

In figure 8.11 contour plots, representing the scattered intensity as an integral in the limits $2 \times 10^{-2}\mathrm{nm}^{-1} \leqslant \mathrm{Q} \leqslant 2 \times 10^{-1}\mathrm{nm}^{-1}$ in dependence on the time t and the angle with respect to the direction of the shear flow, are shown. Three different ferrogel composites, either containing hematite particles of varying aspect ratio ν or of different polymer mass ratio ψ are investigated by means of oscillatory shear experiments.
From left to right, the first two contour plots show results from the investigation of the composites pSys 6 HEM 4 with $\psi = 1$ and $\nu_{\mathrm{HEM4}} = 2.9$ at a shear frequency $f = 0.05\,\mathrm{s}^{-1}$ and pSys 6 HEM 3 with $\psi = 1$ and $\nu_{\mathrm{HEM3}} = 5.2$ at a shear frequency $f = 0.1\,\mathrm{s}^{-1}$. Over the period of two deformation cycles each, it is visible, that the anisotropy of the scattering pattern is much more pronounced for hematite particles of bigger aspect ratio. Hence, the out of shear plane alignment of the particles due to particle matrix interactions is intensified with increasing shape anisotropy of the hematite particles. Additionally the contour plots also confirm, that the occurring intensity fluctuations are in phase with the deformation and the shear frequency, respectively.
In the middle and on the right hand side of figure 8.11, contour plots from temporal analysis of composites pSys 6 HEM 3 with $\psi = 1$ and $\nu_{\mathrm{HEM3}} = 5.2$ at a shear frequency $f = 0.1\,\mathrm{s}^{-1}$ and pSys 6 HEM 3 with $\psi = 4$ and $\nu_{\mathrm{HEM3}} = 5.2$ at a shear frequency $f = 0.1\,\mathrm{s}^{-1}$ are shown. Comparing the intensity fluctuations for different sectors, it becomes obvious that an increasing polymer mass fraction ψ significantly increases the anisotropy of the scattering pattern, which can be explained by enhanced particle-matrix interactions. An increased polymer volume intensifies the out of plane alignment of the hematite particles, embedded in the pNIPAM matrix. The phase relation of intensity fluctuations and deformations is not influenced by the polymer mass fraction.

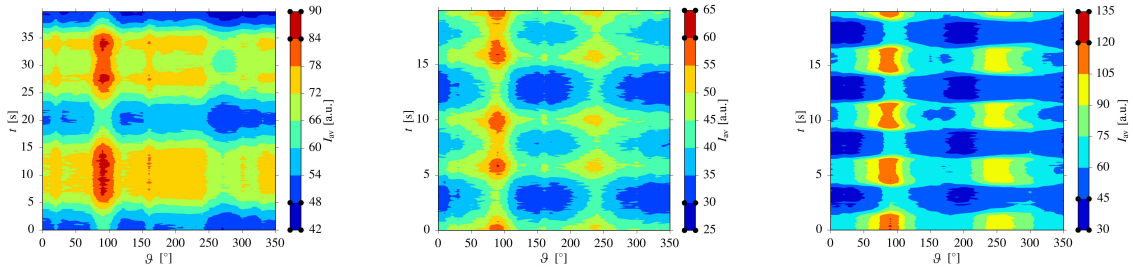

Figure 8.11: Contour plots, representing the scattered intensity in dependence on the time t and the angle ϑ with respect to the direction of the shear flow as an integral within the limits $2 \times 10^{-2}\mathrm{nm}^{-1} \leqslant \mathrm{Q} \leqslant 2 \times 10^{-1}\mathrm{nm}^{-1}$. Left: Composite pSys 6 HEM 4 with $\psi = 1$ and $\nu_{\mathrm{HEM4}} = 2.9$ at a shear frequency $f = 0.05\,\mathrm{s}^{-1}$. Middle: pSys 6 HEM 3 with $\psi = 1$ and $\nu_{\mathrm{HEM3}} = 5.2$ at $f = 0.1\,\mathrm{s}^{-1}$. Right: pSys 6 HEM 3 with $\psi = 4$ and $\nu_{\mathrm{HEM3}} = 5.2$ at $f = 0.1\,\mathrm{s}^{-1}$.

A correlation between the anisotropy of the scattering pattern and the shear deformation of the oscillatory shear experiments is shown in figure 8.12. The composite

pSys 6 HEM 3 with $\psi = 1$ and $\nu_{\mathrm{HEM3}} = 5.2$ is investigated at a constant shear frequency $f = 0.1\,\mathrm{s}^{-1}$ for deformations $0.1 \leqslant \gamma \leqslant 10$. The loss and storage modulus G' and G'' indicate linear viscoelastic (LVE) behavior up to deformations of $\gamma = 6 \times 10^{-1}$ (see figure 8.12, upper row). Exceeding this critical deformation, with increasing deformation the system transits into the nonlinear viscoelastic region (NLVE region).
Sector averaged mean intensities for sectors parallel ($\vartheta = 0$) and perpendicular ($\vartheta = \pi/2$) to the shear flow are shown for selected deformations each at maximum plate deflection Φ. It can be seen, that with increasing deformations and furthermore with the transition from the LVE region to the NLVE region the differences between scattering functions become more pronounced. Hence, the amplitude of the angular dependent intensity fluctuations increases with the amplitude of deformation, especially upon entering the nonlinear viscoelastic regime. Shear induced structural changes to the matrix, as occurring within the NLVE region, appear to favor the out of shear plane alignment of the hematite particles due to particle-matrix interactions.

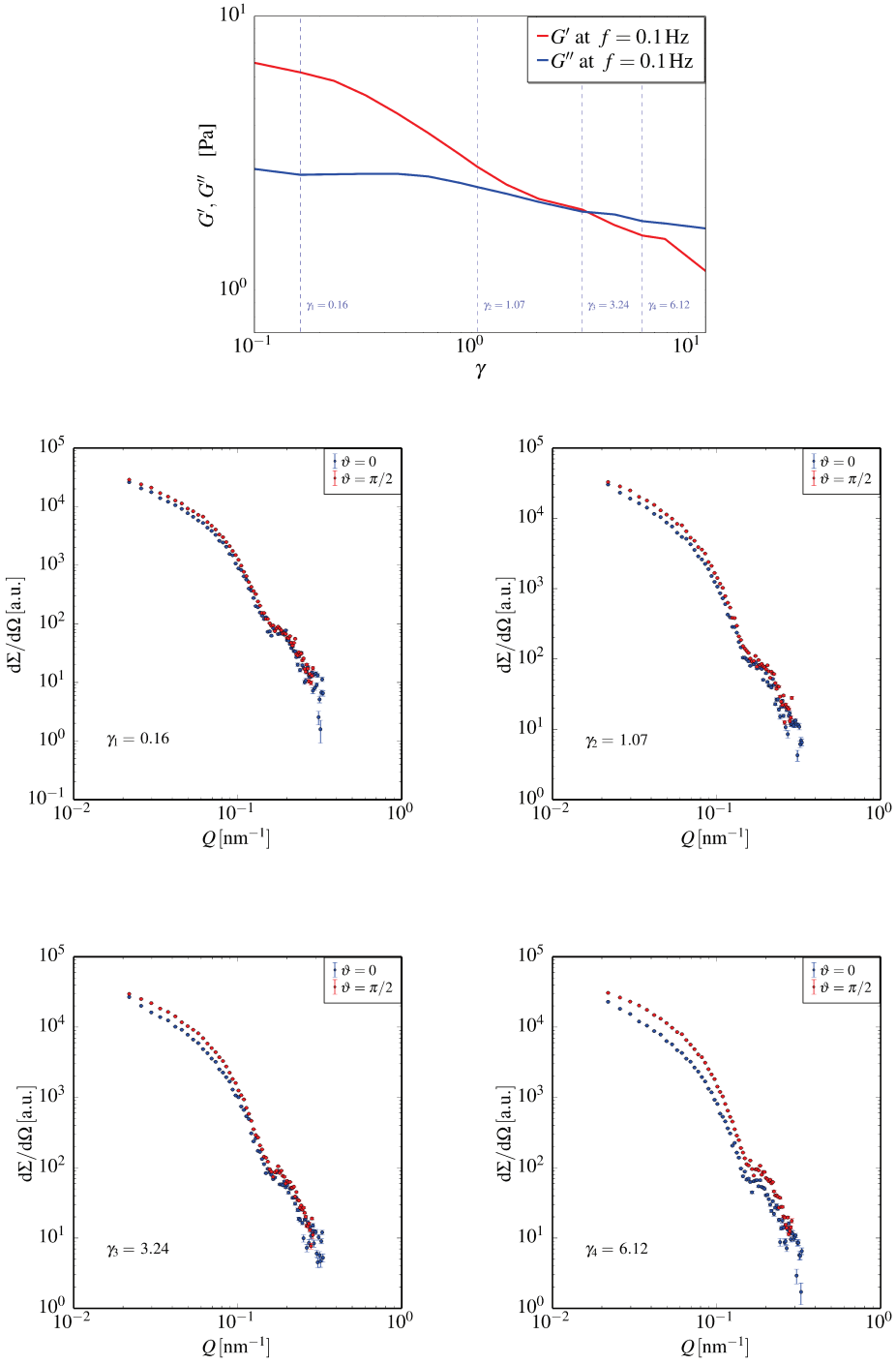

Figure 8.12: Storage and loss moduli G' and G'' in dependence on the deformation γ at a shear frequency $f = 0.1\,\mathrm{s}^{-1}$ of composite pSys 6 HEM 3 with $\psi = 1$ and $\nu_{\mathrm{HEM3}} = 5.2$ (upper row). Sector averaged mean intensities for sectors parallel ($\vartheta = 0$) and perpendicular ($\vartheta = \pi/2$) to the shear flow at distinct deformations $\gamma_1 = 0.16$, $\gamma_2 = 1.07$, $\gamma_3 = 3.24$ and $\gamma_4 = 6.12$

8.3 X-ray photon correlation spectroscopy

small angle X-ray scattering (SAXS) experiments described in section 8.1 give insights into the hematite-pNIPAM-composites structure on mesoscopic length scales with and without the presence of an external magnetic field. Additionally, rheology small angle X-ray scattering (RheoSAXS) experiments, as described in section 8.2, aim to investigate the influence of the polymer networks' vorticity to the ODF of the hematite spindles in real time with a time resolution in the range of seconds.
Quasielastic scattering experiments give insights into the diffusive motion of scatterers. In the time domain, XPCS gives access to dynamic processes at mesoscopic length scales analyzing temporal correlations of the intensity in SAXS experiments employing coherent X-rays.
The fundamental experimental quantity in homodyne photon correlation spectroscopy is the intensity autocorrelation function $g_2(Q,t)$. For ergodic samples, this quantity is related to the field autocorrelation function or intermediate scattering function $g_1(Q,t)$ by the Siegert's relation

$$g_2(Q,t) = 1 + c(Q)g_1^2(Q,t), \tag{8.5}$$

where $c(Q)$ is the Q-dependent speckle contrast.
For a Gaussian diffusion process, the intermediate scattering function can be written as a single-exponential decay

$$g_1(Q,t) = \exp(-Q^2 D_E t) \tag{8.6}$$

with D_0 indicating the Einstein diffusion coefficient. The relaxation rate Γ of the intermediate scattering function is related to the Einstein diffusion coefficient via the Landau-Placzek relation $\Gamma(Q) = D_\mathrm{E} Q^2$. A superposition of processes with a distribution of decay rates leads to a stretched or compressed exponential decay with the form

$$g_1 = \exp\left[-(\Gamma t)^\beta\right] \tag{8.7}$$

of the intermediate scattering function. This functional form originally introduced by Kohlrausch [88] is often denoted as Kohlrausch-William-Watts (KWW) function. Values of $\beta < 1$ indicate a stretched exponential, whereas $\beta > 1$ a compressed exponential decay which is typical for soft matter systems [89, 90]. Employing again Siegert's relation for a multispeckle experiment, the intensity correlation function can be written as

$$\begin{aligned} g_2(Q,t) &= 1 + c(Q) g_1^2(Q,t) \\ &= 1 + c(Q) \exp^2 \left[-(\Gamma t)^\beta \right] \\ &= 1 + c(Q) \exp \left[-2(\Gamma t)^\beta \right] . \end{aligned} \tag{8.8}$$

By fitting a stretched exponential function to the intensity autocorrelation function, Γ with the dimension of an inversed time and therewith the diffusion coefficient are obtained. Figure 8.13 shows an exemplary fit to an intensity autocorrelation function g_2 obtained from an XPCS experiment for the composite pN1 H1.

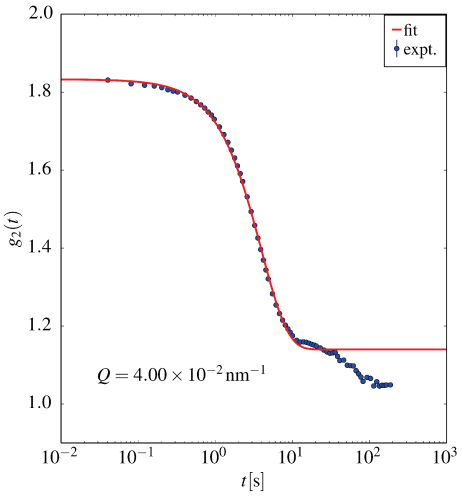

Figure 8.13: Intensity autocorrelation function $g_2(t)$ (blue circles) and compressed exponential function fitted to the experimental data (red, solid line).

X-ray photon correlation spectroscopy (XPCS) experiments presented in this section are performed at the beamline ID10 at the European Synchrotron Radiation Facility (ESRF) in Grenoble, using the same sample environment as for the SAXS experiments at ID02, allowing to apply an external magnetic field of varying flux densities to the sample. Here presented are the results of the investigation of the hematite-pNIPAM composite *pN1 HEM1*, with pNIPAM with a ploymer volume fraction of $\varphi = 0.065$ and crosslinking ratio of $\chi = 0.034$ and hematite spindles of an aspect ratio $\nu = 7.0$. The dynamics of this sample is investigated in dependence on the flux density of a field perpendicular to the primary beam. As for the SAXS experiments, the scattering signal is again evaluated by partitioning the detector plane in multiple sectors and annuli and averaging the intensity of each partition. Hence, an angle dependent intensity $I(\vartheta)$ is obtained also for the XPCS

experiments.
Figure 8.14 shows the Q-dependent relaxation rate $\Gamma(Q)$ versus the square of the scattering vector Q without external magnetic field (left column) and at a flux density $B = 1.0\,\mathrm{T}$ (right column) resulting from the compressed exponential fits to the XPCS data (see 8.13) for sectors parallel ($\vartheta = 0\,^\circ$) and perpendicular ($\vartheta = 90\,^\circ$) to the external magnetic field. A linear relation between both quantities, where the slope of a line trough the origin corresponds to the effective diffusion coefficient D_E, would indicate Gaussian diffusion of the particles within the hydrogel network. As visible for both, field free and within magnetic field conditions, a Q^2- dependent slope of relaxation rates deviating from Landau-Placzek behavior is obtained.
As highlighted by interpolations of data points for both angles $\vartheta = 0\,^\circ$ and $\vartheta = 90\,^\circ$ at $B = 0.0\,\mathrm{T}$ and $B = 1.0\,\mathrm{T}$ (figure 8.14, lower row), a critical, mean Q^2 value corresponding to $Q \approx 0.035\,\mathrm{nm}^{-1}$, can be found, separating two, in first approximation linear regimes for Γ vs. Q^2. The corresponding distance in real space is $\approx$ 180 nm and in accordance with the mean void size of the pNIPAM hydrogel matrix. For small values of $Q^2 < 1.2 \times 10^{-3}\,\mathrm{nm}^{-2}$ and therefore long distances in real space, no angular dependency for the diffusion coefficient is found as can be seen in figure 8.14, regarding the solid green line, representing data for both, $\vartheta = 0\,^\circ$ and $\vartheta = 90\,^\circ$.
For $Q > 1.2 \times 10^{-3}\,\mathrm{nm}^{-2}$ angular dependent differences for the linear relations of Γ vs. Q^2 are observed for no-field conditions and within an external magnetic field of $B = 1.0$ T. Without an external magnetic field, the slopes of $\Gamma(Q)$ vs. Q^2 for both, $\vartheta = 0\,^\circ$ and $\vartheta = 90\,^\circ$ are almost identical, meaning that also the diffusion coefficients are nearly the equal. However, the transition from Gaussian to non-Gaussian diffusion is shifted to smaller length scales in real space for the direction perpendicular ($\vartheta = 90\,^\circ$) to the direction of the external magnetic field. The analysis of the time-averaged intensities did not show any preferred orientation of the hematite particles within the hydrogel matrix, as can be seen in figure 8.4 in section 8.1. This type of experiments is not sensitive to a possible preferred orientation of the hydrogel matrix itself. Hence, it is possible, that the mesostructure of the hydrogel network is influenced during the filling of the capillary previous to the experiments. In this case, shear forces cause stretching of the polymer networks' voids in the direction parallel to the direction of the external field ($\vartheta = 0\,^\circ$). Therewith the transition from quasi-free diffusion of the particles within the viods to diffusion processes between voids is shifted to smaller values of Q in reciprocal space and to larger length scales in real space is possible.
For a flux density of $B = 1.0\,\mathrm{T}$ it is visible, that the slopes of the linear interpolations differ from each other for $\vartheta = 0\,^\circ$ and $\vartheta = 90\,^\circ$ more significantly. In accordance with the nematic order parameters shown in section 8.1, it can be stated that hematite spindles embedded into the pNIPAM hydrogel are almost completely aligned perpendicular to the direction of the external magnetic field at a flux density of $B = 1.0\,\mathrm{T}$. Therefore it can be concluded, that in external magnetic fields the spindle-shaped particles without particle-matrix interactions preferably move in the direction of their particle director, corresponding to the sector centered at $\vartheta = 90\,^\circ$, than in direction of the short particle

axis. This preferred diffusive motion is restricted to the confinement of the voids, existing within the hydrogel network, since it occurs only for sufficiently large Q^2 and corresponding short diffusion paths in real space.
For larger length scales only one significantly faster and direction-independent diffusion coefficient can be found. A possible reason are escape processes through by the hydrogel network preformed diffusion channels as junctions between adjacent voids in the hydrogel network. Since the orientation of such channels is unaffected by external magnetic fields, in this regime which is at the limit of Q-resolution, even in external fields of $B = 1\,\mathrm{T}$ flux density, no direction dependency is observed. The mean squared displacement here is significantly higher, explaining the much steeper slope for Γ vs. Q^2 at $Q^2 < 1.2 \times 10^{-3}\,\mathrm{nm}^{-2}$. Regarding the ratio $D_\mathrm{r} = D_\parallel / D_\perp$ we obtain $D_\mathrm{r}(0\,\mathrm{T}) = 0.84$ and $D_\mathrm{r}(1\,\mathrm{T}) = 0.65$. This again verifies, that the application of an external magnetic field influences the diffusion of the hematite spindles within the matrix more significantly than the effect of a shear induced structural change of the mesostructure of the matrix.
In figure 8.15 the exponent β in dependence on the scattering vector Q, as given in equation (8.8), resulting from fitting scattering data over the whole Q-range is shown for sectors parallel ($\vartheta = 0\,^\circ$) and perpendicular ($\vartheta = 90\,^\circ$) to the external magnetic field. The mean values for β indicate, whether the particles undergo Gaussian or anomalous diffusion processes. Anomalous subdiffusion is hindered diffusion in which the mean-square displacement of a diffusing particle is proportional to some power law different from that of Gaussian diffusion with $\langle r^2 \rangle \propto t$ [91]. For classical Gaussian diffusion, with respect to the Siegert relation, the fit of the field autocorrelation function g_2 would result the exponent $\beta = 1$, recovering an usual exponential function. A stretched exponential function with $\beta < 1$ indicates sub-diffusive processes.
Regarding figure 8.15, for zero-field conditions $\beta \approx 1.2$ (lhs) is obtained. For external magnetic fields with a flux density of $B = 1.0\,\mathrm{T}$, the slightly larger exponent $\beta \approx 1.3$ results. Both exponentials, with values larger than 1, indicate that the hematite particles undergo non-Gaussian behavior within the hydrogel matrix, for both, field-free and in-field conditions. Such a behavior indicated by compressed exponential decays of the autocorrelation functions are commonly observed in jammed systems [89, 90].

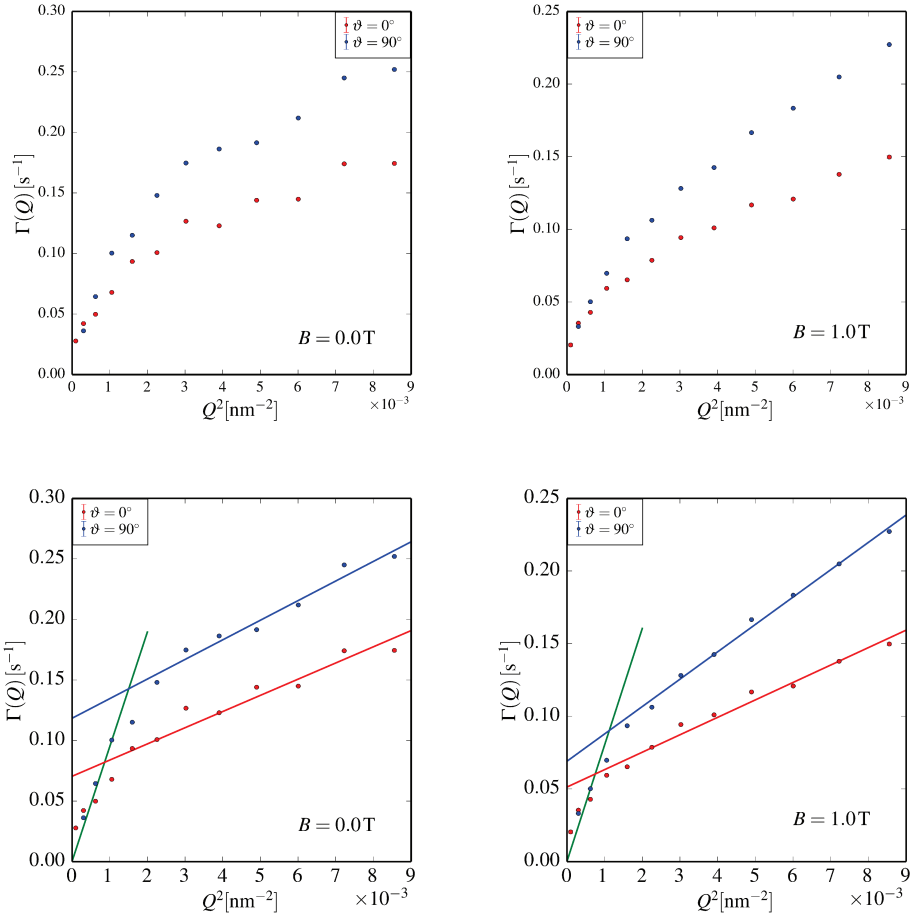

Figure 8.14: Relaxation rate Γ in dependence on the square of the scattering vector Q^2 determined for the composite pN 1 HEM 1, with a ploymer volume fraction $\varphi = 0.065$, a crosslinking ratio $\chi = 0.034$ and hematite spindles of an aspect ratio $\nu = 7.0$ for sectors parallel ($\vartheta = 0\,°$) (red circles) and perpendicular ($\vartheta = 90\,°$) (blue circles) to the external magnetic field for a no field environment (lhs) and for $B = 1.0\,\mathrm{T}$ (rhs).

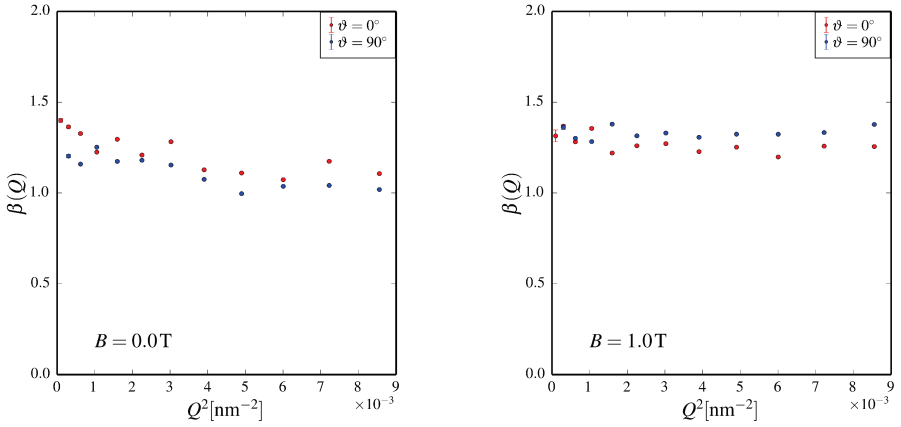

Figure 8.15: Compressed exponential coefficient β in dependence on the square of the scattering vector Q^2 for $B = 0.0\,\mathrm{T}$ and $B = 1.0\,\mathrm{T}$ and sectors parallel ($\vartheta = 0\,°$) (red circles) and perpendicular ($\vartheta = 90\,°$) (blue circles).

9 Summary and outlook

Since the pioneering work of Payne et al. [92] the influence of incorporated nanoparticles on the mechanical properties of elastomers has attracted considerable scientific interest. The macroscopic viscoelastic properties of such composites are strongly influenced by interactions between embedded particles and the polymer network. If shape anisotropic, magnetic particles are embedded in viscoelastic matrices, their mesoscale structure and dynamics and the related macroscopic properties depend on the particles' orientation as an additional degree of freedom. Distortions of the matrix either induced by interaction of the particles with an external field or mechanical stress exerted on the composites influence, both, the spatial and orientational distribution of the particles. In this work, mesoscopic particle-matrix interactions of hematite spindles confined in cavities of an intercrosslinked polymer hydrogel network formed by pNIPAM and related changes of macroscopic, rheological properties have been investigated by means of X-ray scattering and rheological experiments.

Hematite spindles of different aspect ratios ν are prepared, proving the regio-specific NaH_2PO_4-adsorption mechanism, inducing the spindles' preferred growth along their rhombohedral axis. Nanoparticles of polydispersities $p < 15\%$, suitable for X-ray scattering experiments, are obtained. Due to both, a permanent magnetic moment nearly perpendicular to the rotation axis and an induced moment proportional to their negative magnetic anisotropy, hematite particles align perpendicular to the direction of external magnetic fields. The nematic order parameter, calculated from the field dependent ODF of the spindles determined by the evaluation of X-ray scattering data is used to quantify the alignment of of the particles as a function of the flux density B. In figure 6.3 it is visible, that the alignment of the particles in aqueous suspension increases with increasing magnetic flux densities.
pNIPAM hydrogels, consisting of thermoresponsive polymer spheres connected by polymer chains are prepared systematically with varying crosslinking ratios χ and varying polymer volume fractions φ. Static light scattering experiments show a pronounced structure peak for the hydrogels, corresponding to a correlation length in accordance with the polymer spheres' interparticle distances determined by means of TEM. DLS experiments confirm the non-ergodicity of the system, meaning the non-equivalence between time-averaged and ensemble-averaged time-autocorrelation functions, visible from the existence of two separated relaxation processes (see figure 6.5).
Rotational shear experiments are performed to investigate the influence of temperature, polymer volume fraction φ and crosslinking ratio χ on the viscosity η of the matrix. Due

to the characteristic coil-to-globuli transition, with increasing temperature, the viscosity of the hydrogel decreases. With increasing crosslinking ratio χ, the matrix' viscosity decreases due to therewith decreasing radii of gyration. An increasing polymer volume fraction φ however, result in increasing viscosity, due to enlarged friction in the mesoscale structure of the denser matrix.
Oscillatory shear experiments give insights into the viscoelastic behavior of the pNIPAM hydrogels by evaluating the storage- and loss moduli G' and G'' as an answer to a sinusoidal shear deformation γ in dependence on volume fraction φ and crosslinking ratio χ. Here, an increment of the samples' crosslinking density as well as polymer volume fraction results in a progressing transition from a viscoelastic solid to a viscously dominated liquid-like system within the LVE region for constant shear frequencies f. For constant crosslinking ratio χ and polymer volume fraction φ but increasing shear frequency, the hydrogel matrix shows progressing liquid-like behavior, since restoring forces, contributing to the elastic behavior of the sample are overcome by increasing forces of friction.

Furthermore, hematite-pNIPAM composites are prepared to investigate the changes of mechanical properties of the hydrogel induced by the presence of shape anisotropic, magnetic nanoparticles. For this reason, rotational and oscillatory shear experiments with and without external magnetic fields within the sample environment are performed.
For field-free conditions, rotational shear experiments show, that the addition of hematite nanoparticles to the polymer network causes a significant rise in viscosity compared to the unloaded hydrogels. This is because incorporated nanoparticles cause an additional moment of friction within the voids of the gel. Considering the viscoelastic properties of the composites compared to unloaded hydrogels, no influence of the hematite particles to these properties can be stated.
In presence of an external field, in rheological experiments an increasing viscosity of the composites with increasing flux density is observed. Freely rotating particles minimize their rotational friction by following the angular velocity field of their environment. In presence of a magnetic field, however, the rotational mobility of the particles is progressively confined with increasing flux density. Also in oscillatory shear experiments, at least for small deformations, an elastic particle-matrix interaction is observed: increasing flux density solely affects the elastic modulus G', whereas the loss modulus for deformations $\gamma < 10^{-1}$ is nearly unchanged at constant oscillation frequency f. With the flux density increasing rotational arrest of hematite particles leads as an increasing polymer volume fraction φ and crosslinking ratio χ to rising elasticity of the composites. Phenomenologically, embedded hematite particles act as additional, field-dependent crosslinkers.

The field-induced rotation of particles embedded in a hydrogel leads to an elastic deformation of the polymer network causing a restoring torque related to the elastic modulus of the hydrogel. Hence, the orientational distribution function of hematite spindles as a function of the flux density, derived from the analysis of SAXS data, is influenced by particle-matrix interactions in these composites.

The interactions of the particles with an external magnetic field provoke a field-induced isotropic-nematic phase transition which is progressively hindered with increasing elasticity of the matrix. The orientational correlation of the particles is quantified by the nematic order parameter S_2 in dependence on the flux density. Since the elastic moduli of hydrogels are influenced by the polymer volume fraction φ as well as by the crosslinking ratio χ, both parameters affect the nematic order parameter S_2 of hematite spindles in different hydrogel matrices as a function of the flux density as visible in figures 8.6 and 8.7.
The complete reversibility of the field-induced nematic transition clearly indicates that the hindrance of nematic alignment is related to the elasticity and not to an increased Newtonian viscosity: purely viscous particle-matrix interactions would not change the thermal equilibrium at a given flux density, but only slow down the systems' response to a jump in magnetic flux density. For all samples, the thermal equilibrium is reached after several seconds and removing of the external field results after few seconds in isotropic ODFs.

Further insights into the shear-induced changes of the mesostructure are given by simultaneous rheological and SAXS experiments. Here, the influence of the networks' vorticity to the ODF of the hematite spindles is investigated. Experimentally, as a first step, particles are aligned with their long axis parallel to the shear plane and perpendicular to the shear gradient, which is parallel to the primary beam, by a radial shear flow. This radial shear flow results when compression drops of isotropic composites between the rheometer plates.
In oscillatory shear experiments, periodic fluctuations of the scattered intensity from isotropic to anisotropic patterns in phase with the shear deformation, are observed (see figure 8.10). Concerning the sample properties, it is found that the anisotropy of the scattering pattern is more pronounced for composites with hematite particles of high aspect ratios ν as well as with an increasing polymer mass fraction ψ. Evaluating deformation sweeps shows, that shear induced structural changes to the matrix, as occurring within the NLVE region, appear to favor the out of shear plane alignment of hematite due to particle-matrix interactions. Therewith it can be stated, that the anisotropy of the scattering evolves with increasing shear deformation.

To investigate the dynamic behavior of the hematite particles within the pNIPAM hydrogel, XPCS experiments with and without an external magnetic field applied to the sample are performed. From the relaxation rates $\Gamma(Q)$ derived from compressed exponential fits to the intensity autocorrelation function, two different diffusion processes can be identified. For large scattering vectors corresponding to diffusion paths smaller than the size of voids in the hydrogel network, in presence of external fields a preferred diffusive motion parallel to the particle director is observed. In the region of smaller Q, observing long diffusion paths between adjacent voids, even in presence of external fields, a direction-dependence could not be observed. The increased slope of $\Gamma(Q)$ vs. Q^2 in this domain is a hint for faster diffusion in preformed channels of the network, the orientation of which

is not influenced by external fields. In both regimes, the compressed exponential decay of the intensity autocorrelation function indicates a non-Gaussian diffusion behavior of the hematite particles in the hydrogel matrix, where their diffusion is limited by the surrounding polymer network, both with and in absence of external fields.

The quantitative analysis of the hydrogels' elastic properties from the field-dependent nematic order parameter is the scope of future work. With known magnetic properties of the hematite spindles, i.e. the magnitude of their magnetic moment, the direction of the magnetic moment with respect to the particle axis and their magnetic anisotropy, the torque acting on the hematite spindles in presence of magnetic fields can be calculated. On the other hand, from the particles geometry and their roatation, the deformation of the hydrogel network is accessible.
First attempts to model the mesostructural response of ferrogels are described by Weeber et al.[93] and Pessot et al.[94] by molecular dynamics on a coarse grained level. The hindrance of nematic alignment of anisotropic particles due to elastic distortion of gels can be used to compare these theoretic results with experimental data, since geometry and torques acting on the particles as well as the elastic properties of the matrix are known. Furthermore, Brader et al. [95] proposed a mode coupling approach to describe the nonlinear viscoelastic behavior of colloidal particles. As an input for this quantitative approach the static structure factor of the colloidal system is used. Since the hydrogel, presented in this work, consists of chemically crosslinked polymer spheres, this approach is also promising to analyze the nonlinear viscoelasticity of these composites. Due to the limited Q-range accessible by light scattering and the small electron density of the polymer, additional neutron scattering experiments are required to access the structure factor of the hydrogel matrix in the relevant Q-range.
Regarding the sample system itself, the introduction of charges to the polymer structure is of interest for future work. Charges within such polyelectrolyte-hydrogels induce additional interactions, relevant for many composite systems. For example colloids, often carry charges stabilizing dispersions of these particles. If such charged colloidal particles are embedded into polyelectrolyte-hydrogels, additional electrostatic particle-matrix interactions define the properties of these systems. Especially in the area of biomedical applications, polyelectrolyte hydrogels are already discussed as potential drug delivery systems. Many pharmaceuticals carry acidic or basic functionalities, influencing the interactions between pharmaceutical and matrix. By varying the pH or the ionic strength during the application in biologic environments, due to varying interactions with the hydrogel matrix, pharmaceutical can be released [96].

List of Figures

List of Tables

Bibliography

[1] A. R. Payne. The dynamic properties of carbon black-loaded natural rubber vulcanizates. part i. *Journal of Applied Polymer Science*, 6(19):57–63, 1962.

[2] Y. C. Yuan, T. Yin, M. Z. Rong, and M. Q. Zhang. Self healing in polymers and polymer composites. Concepts, realization and outlook: A review. *eXPRESS Polymer Letters*, 2(4):238–250, 2008.

[3] R. Mohr, K. Kratz, T. Weigel, M. Lucka-Gabor, M. Moneke, and A. Lendlein. Initiation of shape-memory effect by inductive heating of magnetic nanoparticles in thermoplastic polymers. *Proceedings of the National Academy of Sciences USA*, 103(10):3540–3545, 2006.

[4] W. Huang. On the selection of shape memory alloys for actuators. *Materials and Design*, 23(1):11–19, 202.

[5] J. Joule. On the effects of magnetism upon the dimensions of Iron and Steel bars. *The London, Edinburgh and Dublin philosophical magazine and journal of science*, pages 225–241, 1947.

[6] G. Kocak and C. Tuncera and V. Bütün. pH-Responsive polymers. *Polymer Chemistry*, 1(8):144–176, 2017.

[7] M. A. Ward and T. K. Georgiou. Thermoresponsive Polymers for Biomedical Applications. *Polymers*, 3(3):1215–1242, 2011.

[8] R. Dinarvand and A. D'Emanuele. The use of thermoresponsive hydrogels for on-off release of molecules. *Journal of Controlled Release*, 36:221–227, 1995.

[9] C. Scherer and A. M. Figueiredo Neto. Ferrofluids: Properties and Applications. *Brazilian Journal of Physics*, 35(3A):718–727, 2005.

[10] W. Voit, D. K. Kim, W. Zapka, and M. Muhammed. Magnetic behavior of coated superparamagnetic iron oxide nanoparticles in ferrofluids. *Materials Research Society Proceedings*, 676, 2001.

[11] N. Efron, P. B. Morgan, I. D. Cameron, N. A. Brennan, and M. Goodwin. Oxygen permeability and water content of silicone hydrogel contact lens materials. *Optometry and Vision Science*, 84(4):328–337, 2007.

[12] R. M. Kappel and G. J. M. Pruijn. The monobloc hydrogel breast implant, experiences and ideas. *European Journal of Plastic Surgery*, 35(3):229–233, 2012.

[13] J. Chen, H. Park, and K. Park. Synthesis of superporous hydrogels: Hydrogels with fast swelling and superabsorbent properties. *Journal of Biomedical Materials Research*, 44(1):53–62, 1999.

[14] E. Caló and V. V. Khutoryanskiy. Biomedical applications of hydrogels: A review of patents and commercial products. *European Polymer Journal*, 65:252–267, 2015.

[15] T. R. Hoare and D. S. Kohane. Hydrogels in drug delivery: Progress and challenges. *Polymer*, 49:1993–2007, 2008.

[16] A. S. Hoffman. Hydrogels for biomedical applications. *Advanced Drug Delivery Reviews*, 64:18–23, 2012.

[17] H. Rahn, I. Gomez-Morilla, R. Jurgons, Ch. Alexiou, and S. Odenbach1. Microcomputed tomography analysis of ferrofluids used for cancer treatment. *Journal of Physics: Condensed Matter*, 20:204152, 2008.

[18] Jacob Rabinow. The magnetic field clutch. *American Institute of Electrical Engineers Transactions*, 67:308–315, 1948.

[19] T. van Vliet. Rheological properties of filled gels. influence of filler matrix interaction. *Colloid and Polymer Science*, 266(6):518–524, 1988.

[20] X. Zhao, J. Kim, C.A. Cezar, N. Huebsch, K. Lee, K. Bouhadir, and D.J. Mooney. Active scaffolds for on-demand drug and cell delivery. *Proceedings of the National Academy of Sciences USA*, 108(1), 2011.

[21] T. Y. Liu, S. H. Hu, T. Y. Liu, D. M. Liu, and S. Y. Chen. Magnetic-Sensitive Behavior of Intelligent Ferrogels for Controlled Release of Drug. *Langmuir*, 22(14):5974–5978, 2006.

[22] J. Qin, I. Asempah, S. Laurent, A. Fornara, R. N. Muller, and M. Muhammed. Injectable Superparamagnetic Ferrogels for Controlled Release of Hydrophobic Drugs. *Advanced Materials*, 21(13):1354–1357, 2009.

[23] L. L. Lao and R. V. Ramanujan. Magnetic and hydrogel composite materials for hyperthermia applications. *The Journal of Materials Science: Materials in Medicine*, 15(10):1061–4, 2004.

[24] S. H. Song, J. H. Park, G. Chitnis, R. A. Siegel, and B. Ziaie. A wireless chemical sensor featuring iron oxide nanoparticle-embedded hydrogels. *Sensors and Actuators B: Chemical*, 193:925–930, 2014.

[25] A. Yu. Zubarev and A. S. Elkady. Magnetodeformation and elastic properties of ferrogels and ferroelastomers. *Physica A: Statistical Mechanics and its Applications*, 413:400 – 408, 2014.

[26] L. Barsi and M. Zrínyi. Ferrogels as magnetomechanical actuators. *ACH - Models in Chemistry*, 135(3):241–246, 1998.

[27] M. Zrínyi. *Intelligent Materials - Magnetic Polymeric Gels as Intelligent Artificial Muscels*. RSC Publishing, 2008.

[28] H. G. Schild. Poly(N-isopropylacrylamide): experiment, theory and application. *Progress in Polymer Science*, 17(2):163–249, 1992.

[29] C. Märkert, B. Fischer, and J. Wagner. Small-angle scattering from spindle-shaped colloidal hematite particles in external magnetic fields. *Journal of Applied Crystallography*, 44(3):441–447, 2011.

[30] P. J. Carreau, De Kee D. C. R., and R. P. Chhabra. *Rheology of Polymer Systems: Principles and Applications*. Hanser Publisher, 1997.

[31] T. Mezger. *Das Rheologie-Handbuch: Für Anwender von Rotations- und Oszillations-Rheometern*. Vincentz, 2000.

[32] P. Kapitzka. Viscosity of liquid helium below the λ-point. *Nature*, 141(74), 1938.

[33] H. Giesekus. *Phänomenologische Rheologie : Eine Einführung*. Springer, 1994.

[34] R. G. Larson. *Structure and Rheology of complex fluids*. Oxford University Press, 1999.

[35] V. A. Hackley and C. F. Ferraris. Guide to Rheological Nomenclature: Measurements in Ceramic Particulate Systems. *NIST Special Publications 946*, 2001.

[36] L. C. Maxwell. A Dynamical Theory of the Electromagnetic Field. *Philosophical Transactions of the Royal Society*, 1865.

[37] I. N. Levine. *Physical Chemistry*. McGrawHill, 6 edition, 2009.

[38] M. Kerker. *The Scattering of Light and other Electromagnetic Radiation*. Academic Press, Inc., 1969.

[39] R. Siegel, J. R. Howell, and M. Pinar Mengüc. *Thermal radiation heat transfer*. CRC Press, 5 edition, 2011.

[40] B. J. Berne and Robert P. *Dynamic Light Scattering - With Applications to Chemistry, Biology, and Physics*. Dover Publications, Inc., 2000.

[41] G. Mie. Beiträge zur Optik trüber Medien, speziell kolloider Metallösungen. *Annalen der Physik*, 25(3):377–445, 1908.

[42] Redouane B. and Robert P., editors. *Soft Matter Characterization*, volume 2. Springer, 2008.

[43] J. D. Jackson. *Classical Electrodynamics*. Wiley, New York, 1975.

[44] P. W. Schmidt. *Modern Aspects of Small-Angle Scattering*. Kluwer Academic, 1995.

[45] G. V. Schulz. Molecular weight determination on macromolecular compounds. VIII. Distribution function of multimolecular compounds and their determination by fractionation. *Z. Phys. Chem.*, B47:155–193, 1949.

[46] J. P. de Gennes and J. Prost. *The Physics of Liquid Crystals*. Oxford Science Publcations, 1993.

[47] M. R. Wilson. Determination of order parameters in realistic atom-based models of liquid crystal systems . *Journal of Molecular Liquids*, 68(1):23–31, 1996.

[48] R. Brown. A brief account of microscopical observations made in the months of June, July and August, 1827, on the particles contained in the pollen of plants; and on the general existence of active molecules in organic and inorganic bodies. *Edinburgh new Philosophical Journal*, pages 358 – 371, 1828.

[49] A. Einstein. Über die von der molekularkinetischen Theorie der Wärme geforderte Bewegung von in ruhenden Flüssigkeiten suspendierten Teilchen. *Annalen der Physik*, 332(8):549–560, 1905.

[50] W. Sutherland. A dynamical theory of diffusion for non-electrolytes and the molecular mass of albumin. *Philosophical Magazine Series 6*, pages 781–785, 1905.

[51] M. Smoluchowski. Zur kinetischen Theorie der Brownschen Molekularbewegung und der Suspensionen. *Annalen der Physik*, 326(14):756–780, 1906.

[52] J. B. Hayter and J. Penfold. Self-consistent Structural and Dynamic Study of Concentrated Micelle Solutions. *Journal of the Chemical Society, Faraday Transactions 1*, 77:1851–1863, 1981.

[53] A. R. Altenberger and J. M. Deutch. Light scattering from dilute macromolecular solutions. *American Institute of Physics*, 59(2), 1973.

[54] B. J. Ackerson, P. N. Pusey, and R. J. A. Tough. Interpretation of the intermediate scattering function at short times. *Journal of Chemical Physics*, 76(3), 1982.

[55] M. Zrínyi, L. Barsi, and A. Búki. Ferrogel: a new magneto-controlled elastic medium. *Polymer Gels and Networks*, 5:415–427, 1997.

[56] S. Backes, M. U. Witt, E. Roeben, L. Kuhrts, S. Aleed, A. M. Schmidt, and R. von Klitzing. Loading of PNIPAM Based Microgels with CoFe2O4 Nanoparticles and Their Magnetic Response in Bulk and at Surfaces. *The Journal of Physical Chemistry B*, 119(36):12129–12137, 2015. PMID: 26262551.

[57] H. Remmer, J. Dieckhoff, A. Tschöpe, E. Roeben, A. M. Schmidt, and F. Ludwig. Dynamics of CoFe2O4 Single-Core Nanoparticles in Viscoelastic Media . *Physics Procedia*, 75:1150–1157, 2015. 20th International Conference on Magnetism, {ICM} 2015.

[58] T. Nakao, D. Nagao, H. Ishii, and M. Konno. Synthesis of monodisperse composite poly(N-isopropylacrylamide) microgels incorporating dispersive Pt nanoparticles with high contents . *Colloids and Surfaces A: Physicochemical and Engineering Aspects*, 446:134–138, 2014.

[59] S. Papell. Low viscosity magnetic fluid obtained by the colloidal suspension of magnetic particles. patent, November 1965.

[60] R. Moskowitz K. Raj. Commercial applications of ferrofluids. *Journal of Magnetism and Magnetic Materials*, 85:233–245, 1990.

[61] N. Bayat, A. Nethe, J. M. Guldbakke, J. Hesselbach, V. A. Naletova, H. D. Stahlmann, E. Uhlmann, and K. Zimmermann. *Technical Applications*, pages 359–430. Springer, 2009.

[62] C. Alexiou, R.J. Schmid, and R. Jurgons. Targeting cancer cells: magnetic nanoparticles as drug carriers. *European Biophysics Journal*, 35:466, 2006.

[63] A. Zahoor Abbasi, L. Gutiérrez, L. L. del Mercato, F. Herranz, O. Chubykalo-Fesenko, S. Veintemillas-Verdaguer, W. J. Parak, M Puerto Morales, J. M González, A. Hernandoe, and P. de la Presa. Magnetic capsules for NMR imaging: Effect of magnetic nanoparticles spatial distribution and aggregation. *The Journal of Physical Chemistry C*, 2011.

[64] I. Hilger, R. Hergt, and W. A. Kaiser. Use of magnetic nanoparticle heating in the treatment of breast cancer. *IEE. Proceedings - Nanobiotechnoogy*, 152:33–39, 2005.

[65] S. Purushotham, P. E. J. Chang, H. Rumpel, I. H. C. Kee, R. T. H. Ng, P. K. H. Chow, C. K. Tan, and R .V. Ramanujan. Thermoresponsive core–shell magnetic nanoparticles for combined modalities of cancer therapy. *Nanotechnology*, 20(30):305101, 2009.

[66] G. Filipcsei, I. Csetneki, A. Szilágyi, and M. Zrínyi. Magnetic Field-Responsive Smart Polymer Composites. *Adv Polym Sci*, 206:137–189, 2007.

[67] M. Zrínyi, L. Barsi, and A. Búki. Deformation of ferrogels induced by nonuniform magnetic fields. *American Institute of Physics*, 104, 1996.

[68] J. R. Retama, N. E. Zafeiropoulos, C. Serafinelli, R. Rojas-Reyna, B. Voit, E. Lopez Cabarcos, and M. Stamm. Synthesis and Characterization of Thermosensitive PNIPAM Microgels Covered with Superparamagnetic γ-Fe2O3 Nanoparticles. *Langmuir*, 23(20):10280–10285, 2007. PMID: 17718580.

[69] L. Y. Huang and M. C. Yang. Behaviors of controlled drug release of magnetic-gelatin hydrogel coated stainless steel for drug-eluting-stents application. *Journal of Magnetism and Magnetic Materials*, 310(2):2874–2876, 2007.

[70] H. N. W. Lekkerkerker and G. J. Vroege. Liquid crystal phase transitions in suspensions of mineral colloids: new life from old roots. *Philosophical Transactions of the Royal Society of London A: Mathematical, Physical and Engineering Sciences*, 371(1988):1–20, 2013.

[71] J. C. P. Gabriel and P. Davidson. New Trends in Colloidal Liquid Crystals Based on Mineral Moieties. *Advanced Materials*, 12(1):9–20, 2000.

[72] R. P. Murphy, K. Hong, and N. J. Wagner. Therresponsible Gels Composed of Colloidal Silica Rods with Short-Range attractions. *Langmuir*, 32:8424–8435, 2016. Text hier eingeben.

[73] L. Onsager. The effects of shape in the interaction of colloidal particles. *Annals of the New York Academy of Sciences*, 51(4):627–659, 1949.

[74] I. Martchenko, J. Crassous, A. Mihut, A. Menzel, H. Dietsch, P. Linse, and P. Schurtenberger. Anisotropic magnetic particles in a magnetic field. *Soft Matter*, 12:8755–8767, 2016.

[75] de Souza-Santos, P., Vieira-Coelho, A. C., de Souza-Santos, H., and Kunihiko-Kiyohara, P. . Hydrothermal synthesis of well-crystallised boehmite crystals of various shapes. *Materials Research*, 12:437 – 445, 2009.

[76] S. Kametani, S. Sekine, T. Ohkubo, T. Hirano, K. Ute, H. N. Cheng, and T. Asakura. NMR studies of water dynamics during sol-to-gel transition of poly(N-isopropylacrylamide) in concentrated aquous solution. *Polymer*, 109:287–296, 2017.

[77] G. Graziano. On the temperature-induced coil to globule transition of poly-N-isopropylacrylamide in dilute aqueous solutions. *International Journal of Biological Macromolecules*, 27:89–97, 2000.

[78] M. Ozaki, Stanka K., and E. Matijević. Formation of monodispersed spindle-type hematite particles. *Journal of Colloid and Interface Science*, 102(1):146–151, 1984.

[79] Z. Hu and G. Huang. A New Route to Crystalline Hydrogels, Guided by a Phase Diagram. *Angewandte Chemie International Edition*, 42(39):4799–4802, 2003.

[80] ESRF. ID02 beamline specifications. `http://www.esrf.eu/home/UsersAndScience/Experiments/CBS/ID02/BeamlineLayout.html`, 12 2016.

[81] ESRF. ID10 beamline specifications. `http://www.esrf.eu/UsersAndScience/Experiments/CBS/ID10`, 12 2016.

[82] K. D. Finkelstein, Q. Shen, and S. Shastri. Resonant X-Ray Diffraction near the Iron K Edge in Hematite. *Physical Review Letters*, 69(10):1612–1615, 1992.

[83] E. Stellamanns, D. Meissner, M. Lohmann, and B. Struth. A Unique Rheology / SAXS Combination at DESY / Petra III. *Journal of Physics: Conference Series*, 425(20):202007, 2013.

[84] I. V. Golosovsky, I. Mirebeau, F. Fauth, D. A. Kurdyukov, and Yu. A. Kumzerov. Magnetic structure of hematite nanostructured in a porous glass. *Solid State Communications*, 141(4):178 – 182, 2007.

[85] B. J. Lemaire, P. Davidson, J. Ferre, J. P. Jamet, D. Petermann, P. Panine, I. Dozov, and J. P. Jolivet. Physical properties of aqueous suspensions of goethite (alpha-FeOOH) nanorods - Part I: In the isotropic phase. *The European Physical Journal E - Soft Matter*, 13(3):291–308, March 2004.

[86] P. N. Pusey and W. Van Megen. Dynamic light scattering by non-ergodic media. *Physica A: Statistical Mechanics and its Applications*, 157(2):705–741, 1989.

[87] J. Goodwin and R. Hughes. *Rheology for Chemists : An Introduction*. RSC Publishing, 2 edition, 2008.

[88] R. Kohlrausch. Theorie des elektrischen Rückstand in der Leidner Flasche. *Annalen der Physik und Chemie*, 91:179–213, 1854.

[89] A. Madsen, R. L. Leheny, H. Guo, M. Sprung, and O. Czakkel. Beyond simple exponential correlation functions and equilibrium dynamics in x-ray photon correlation spectroscopy. *New Journal of Physics*, 12:055001, 2010.

[90] J. Gabriel, T. Blochowicz, and B. Stühn. Compressed exponential decays in correlation experiments: The influence of temperature gradients and convection. *Journal of Chemical Physics*, 142:104902, 2015.

[91] M. J. Saxton. Anomalous Subdiffusion in Fluorescence Photobleaching Recovery: A Monte Carlo Study. *Biophysical Journal*, 81:2226–2240, 2001.

[92] A. R. Payne and R. E. Whittaker. Low strain dynamic properties of filled rubbers. *Rubber Chemistry and Technology*, 44(2):440–478, 1971.

[93] R. Weeber, S. Kantorovich, and C. Holm. Ferrogels cross-linked by magnetic particles: Field-driven deformation and elasticity studied using computer simulations. *The Journal of Chemical Physics*, 143(15):154901, 2015.

[94] G. Pessot, H. Löwen, and A. M. Menzel. Dynamic elastic moduli in magnetic gels: Normal modes and linear response. *The Journal of Chemical Physics*, 145(10):104904, 2016.

[95] J. M. Brader, M. Siebenbürger, M. Ballauff, K. Reinheimer, M. Wilhelm, S. J. Frey, F. Weysser, and M. Fuchs. Nonlinear response of dense colloidal suspensions under oscillatory shear: Mode-coupling theory and Fourier transform rheology experiments. *Physical Review E*, 82:061401, Dec 2010.

[96] A. Khare and N. Peppas. Swelling/deswelling of anionic copolymer gels. *Biomaterials*, 16(7):559–567, 1995.

Publications and conference talks on the topic

Publications

A. Nack, J. Seifert, C. Passow, J. Wagner
Hindered nematic alignment of hematite spindles in viscoelastic matrices,
arXiv:1704.05659, April 2017

Presentations

Rheological properties of binary colloidal mixtures consisting of thermosensitive polymer particles and anisotropic hematite particles, 113. Bunsentagung, Hamburg, *Mai 2014*
A. Nack, F. Ziegert, C. Passow, J. Wagner

Investigation of rheological and dynamic properties of composites consisting of viscous hydrogels and anisotropic hematite particles, 2. DFG SPP Kolloquium, Benediktbeuern, *September 2014*
A. Nack, C. Passow, J. Wagner

Hindered nematic alignment of hematite spindles in viscoelastic matrices, 15.Ferrofluid Workshop, Rostock, *Juni 2015*
A. Nack, J. Seifert, C. Passow, J. Wagner

Hindered nematic alignment of hematite spindles in viscoelastic matrices, 3. DFG SPP Kolloquium, Benediktbeuern, *September 2015*
A. Nack, J. Seifert, C. Passow, J. Wagner

Hindered nematic alignment of hematite spindles in viscoelastic matrices, 115. Bunsentagung, Rostock, *Mai 2016*
A. Nack, J. Seifert, C. Passow, J. Wagner

Particle-matrix interactions between charged, anisotropic hematite particles and polyelectrolyte hydrogels, 4. DFG SPP Kolloquium, Benediktbeuern, *September 2016*
A. Nack, J. Seifert, C. Passow, J. Wagner

Danksagung

An dieser Stelle möchte ich allen Beteiligten danken, die die Fertigstellung dieser Arbeit im Laufe der letzten Jahre ermöglichten.

Prof. Dr. Joachim Wagner danke ich dafür, dass er mir 2011 die Möglichkeit gab, mich in seinem Arbeitskreis mit physikalischer Chemie jenseits der von uns Studenten *geliebten* Thermodynamik auseinander zu setzen. Seither durfte ich mich mit vielen interessanten Fragestellungen auf dem Gebiet der Ferrogele befassen. Danke für eine kompetente Betreuung und viele anregende wissenschaftliche Diskussionen während dieser Zeit, sowie für die Möglichkeit, meine persönlichen Grenzen zu entdecken und dabei über mich hinaus zu wachsen.

Prof. Dr. Gerhard Grübel danke ich für die Begutachtung dieser Arbeit. Zudem danke ich ihm dafür, dass ich als Studentin eine Zeit lang in seinem Arbeitskreis forschen und den wissenschaftlichen Alltag an einer Großforschungseinrichtung, wie dem DESY kennenlernen durfte.

Julian Seifert danke ich für seine Ausdauer und Hingabe, mit der das Lösen so manch eines kniffligen Problems für mich zu einer angenehmen und reizvollen Aufgabe wurde. Danke auch für die stetige Unterstützung und Hilfsbereitschaft, wenn es um die Bewältigung langer Rheometertage oder extensiver Synthesevorhaben ging.

Falko Ziergert bin ich für seine Geduld und seinen Ehrgeiz, die mich unser gesamtes Studium, sowie die Zeit der Promotion begleitet haben, zu Dank verpflichtet. So manch' eine Prüfung wäre ohne ihn nicht denkbar gewesen. Bei Dr. Christopher Passow bedanke ich mich für seine immer währende Hilfbereitschaft und sein stets offenes Ohr bezüglich aller Fragen und Problemstellungen, die mir im wissenschaftlichen Alltag begegneten.

Margitta Prieß und Sabine Kindermann möchte ich für die langjährige Unterstützung bei allen denkbaren administrativen Aufgaben, sowie für ihre freundliche und offene Art danken. Beides hat den Arbeitsalltag sehr angenehm werden lassen. Bei allen weiteren Mitgliedern des Arbeitskreises – Kira, Michael, Elisabeth und Philipp – bedanke ich mich für die freundliche Arbeitsatmosphäre in den vergangenen Jahren.

Bei allen KollegInnen und MitdoktorandInnen des DFG Schwerpunktprogrammes 1681 möchte ich mich für den offenen und hilfreichen Austausch auf diversen Tagungen und Meetings bedanken. Danke besonders an Hilke, Kerstin, Micha, Patrick, Rudolf und Christian für die gute Zusammenarbeit.

Den KollegInnen und WissenschaftlerInnen am Deutschen Elektronen Synchrotron (DESY) und der European Synchrotron Radiation Facility (ESRF) danke ich für die intensive Unterstützung bei Messzeiten sowie für viele fruchtvolle Diskussionen. Hervorheben möchte ich dabei Prof. Dr. Gehard Grübel, Dr. Birgit Fischer, Dr. Michael Sprung, Dr. Eric Stellamanns und Dr. Beatrice Ruta.

Dr. Marcus Frank, Gerhard Fulda und Dr. Armin Springer vom Elektronenmikroskopiezentrum (EMZ) Rostock danke ich für die Möglichkeit der Nutzung des Transmissionselektronenmikroskopes und die kompetente Assistenz am Gerät.

Abschließend möchte ich meiner Familie und meinen Freunden dafür danken, dass sie mich mit Geduld und Verständnis auf diesem Weg, der viele Höhen und Tiefen barg, begleitet haben. Besonders möchte ich David danken, der, seit er mich auf meinem Weg begleitet, die Achterbahn der Emotionen mit mir durchlebt und mir in vielen Momenten eine große Stütze war und ist.

Erklärung der Urheberschaft

Hiermit erkläre ich, dass die vorliegende Arbeit selbstständig und unter Verwendung der angegebenen Quellen und Hilfsmittel angefertigt wurde. Es wurden keine anderen Quellen außer den von mir angegebenen verwendet und inhaltlich und wörtlich entnommene Stellen als solche kenntlich gemacht. Die Arbeit wurde bisher in der gleichen oder ähnlicher Form in keiner anderen Prüfungsbehörde vergelegt und auch noch nicht veröffentlicht.

Ort, Datum

Annemarie Nack